รายงานการวิจัยฉบับสมบูรณ์

การจำแนกประเภทของกราฟีนด้วยเทคนิคกล้องจุลทรรศน์และรามานสเปกโตรสโคปี

Graphene Identification Using Optical Microscopy and Raman Spectroscopy

นางสาวรัชนก สมพรเสน่ห์

ได้รับทุนสนับสนุนงานวิจัยจากงบประมาณเงินรายได้ ประจำปีงบประมาณ พ.ศ. 2558

ภาควิชาฟิสิกส์ คณะวิทยาศาสตร์
สถาบันเทคโนโลยีพระจอมเกล้าเจ้าคุณทหารลาดกระบัง

500219475

Research Title: Graphene Identification Using Optical Microscopy and Raman Spectroscopy
Researcher: Dr. Ratchanok Somphonsane
Faculty: Science **Department:** Physics

ABSTRACT

We study the techniques of optical microscopy, Raman spectroscopy and atomic forced microscopy and used them to determine the numbers of layers of graphene samples isolated by micromechanically exfoliation technique on SiO_2 substrate. We find that the results obtained from these three techniques are in good agreement and we are able to determine the number of graphene layers properly and to classify monolayer, bilayer, tri-layer and many-layer graphene. Although all the techniques are simple and reliable, the optical microscopy method is the safest and the most straightforward approach. Moreover, we find that the throughput of optical method is higher than that of the other two techniques although there is some chance for inducing human error. To offset the minor drawback of optical microscopy, Raman spectroscopy and atomic forced microscopy might be needed as additional confirmation methods to determine the layer thickness of graphene samples. These techniques therefore are very useful for study physical properties of each category since they have very distinct properties theoretically. The proper identification of graphene layers will in turn help in understanding the appropriate application that they can be used for.

Keywords: 2D materials; graphene; Raman spectroscopy; atomic forced microscopy; optical microscopy

Acknowledgement

I would like to take this opportunity to express my gratitude to Prof. Jonathan Bird in University at Buffalo for giving me an opportunity to visit there and to work on graphene device fabrication. During my time there, he provided valuable insights and theoretical support for the results obtained in this work. Without his comprehensive knowledge, expertise and foresight of the field, my work here would have never been completed. I appreciate the hospitality that I received from all the group members. Particularly, I would like to thank Harihara Ramamoorthy, a Ph.D. student whom I worked with during my stay at Buffalo. It was a great learning experience with him and I was very much impressed by his work spirit.

This work is supported by King Mongkut's Institute of Technology Ladkrabang Research Fund of 2015 (project # 51).

Ratchanok Somphonsane

Contents

List of Figures

Chapter 1
Introduction

1.1 Introduction to the Research Problem and Its Significance

A central feature of modern electronics is the ability to control the electronic properties of various materials by externally applied voltage. Today's semiconductor industry is based on silicon and driven by Moore's law concerning size reduction in micro-computers. For decades, making silicon metal-oxide-semiconductor field-effect transistors (MOSFETs) smaller has been the key to progress, and device gate lengths had been reduced to 22 nm by 2011. This scaling has led to significant improvements in performance, and to a decrease in price per transistor, but cannot be continued indefinitely. There are number of restrictions, both scientific as well as technological in nature, that place limits on the ultimate size and performance of silicon devices. For example, at some point it is physically impossible to etch transistors to the level of individual atoms [1]. It is roughly estimated from Moore's law, however, that transistors will need to reach this atomic scale by 2020. These transistors will be so small that quantum principles are expected to completely take over their operation. Such challenges have led to a growing interest in searching for new materials and device concepts to ensure that performance continues to improve. Some of the most notable examples are organic conductors, carbon nanotubes (CNTs) [2], spin-based devices, and most recently, graphene [3-4].

Graphene is a two-dimensional, one-atom thick, sheet of carbon atoms that are tightly packed in a honeycomb lattice. This material was isolated for the first time in 2004, by the surprisingly simple approach of using cellophane tape to exfoliate graphene from a piece of graphite [3-5]. Since then, graphene has rapidly emerged as an exceedingly promising material for studies of fundamental physics and for the development of new electronic technologies. Much of the fascination in graphene comes from the unqiue nature of its energy spectrum, which resembles a "Dirac spectrum" for massless fermions and provides a connection to quantum electrodynamics (QED) [6-13]. This results, in turn, in the observation of number of unusual electronic properties, such as a linear dispersion relation for which charge carriers behave like massless relativistic particles, anomalous quantum Hall effects [11-13], finite minimum conductivity [14-16], and suppression of backscattering [17-19].

Motivated by these considerations, we had conducted preliminary study on preparation of graphene on Si/SiO$_2$ substrate using mechanical exfoliation technique. The next step after exfoliation is to determine the number of layers of graphene flakes.

Therefore, in this work, we have conducted study on identification of graphene flakes. We hope to be able to select several potential flakes, both monolayer and bilayer graphene, for using in fabrication of graphene field effect transistors (FETs) in the future.

1.2 Objectives

To determine the number of layers of preselected graphitic flakes that have been transferred onto Si/SiO_2 substrate earlier, using different techniques including optical microscopy, Raman spectroscopy, and atomic force microscopy (AFM).

1.3 Scope of Research

1.3.1 Identifying graphitic flakes using optical microscopy technique
1.3.2 Identifying graphitic flakes using Raman spectroscopy technique
1.3.3 Identifying graphitic flakes using atomic force microscopy (AFM) technique

1.4 Method

1.4.1 Optical Microscopy

- We use an optical microscope to scan the entire wafer at 20× magnification, looking for flakes with a greenish tint that we then study under magnifications of 50× and 100×. The flake with the lowest contrast is assigned as monolayer graphene

1.4.2 Raman spectroscopy

- We use green laser excitation (514.5 nm) to obtain Raman spectra of our monolayer and bilayer graphene samples at room temperature. The number of graphene layers is determined from the shape of the 2D band. Where needed, multi-Lorentzian fitting will be performed for the 2D peak.

1.4.3 Atomic forced microscopy (AFM)

- AFM can be used to map surface potential of graphene, which show the thickness of the graphene layer. Imaging was done in non-contact mode. All images were collected under ambient conditions at room temperature with a scanning raster rate of 1 Hz.

More details on these steps will be discussed in Chapter 3.

Chapter 2
The Properties of Graphene

In this chapter, we introduce some of the key properties of graphene. We start by discussing the honeycomb crystalline structure of graphene, focusing on the formation of σ and π bonds between the carbon atoms. We then proceed to discuss the implications of this type of crystal that lead to unique electronic band structure of both monolayer and bilayer graphene.

2.1 Crystalline Structure of Graphene

As already mentioned in the introduction, graphene is made out of carbon atoms arranged in hexagonal rings which form a honeycomb lattice (see Figure 2.1(a)). An isolated carbon atom has six electrons in the $1s^2 2s^2 2p^2$ configuration. The two electrons in the *1s* orbital are inert and do not contribute to the chemical bonding whereas the remaining four valence electrons of the *2s* and *2p* orbitals (2s, $2p_x$, $2p_y$, $2p_z$) construct bonds between carbon atoms to form the hexagonal lattice. Since the energies of the *2s* and *2p* orbitals are very similar, carbon can form a number of hybridized atomic orbitals characterized by different geometries. In the case of graphene, two of the *2p* electrons ($2p_x$ and $2p_y$) hybridize with the *2s* electron to form three sp^2 orbitals. These sp^2 orbitals are oriented in the *xy*-plane with a mutual angle of 120°, while unhybridized $2p_z$ electrons exist perpendicular to the plane. As depicted in Figure 2.1(a-b), to form a crystal two carbon atoms each utilize one sp^2 hybrid to mutually link up in a σ-bond which the $2p_z$ orbitals form a π-bond that corresponds to a *C-C* double bond. The remaining two sp^2 hybrids overlap with those of another two neighboring carbon atoms, forming σ-bonds between them. Thus, a hexagonal ring of carbon is formed in a 2D layer. These σ-bonds hold carbon atoms tightly in the graphene structure, resulting in the robustness of the crystal that makes the isolation of single atomic layers possible. However, as shown in Figure 2.1(c), the energy bands of these σ orbitals are far from Fermi energy (E_F) and hence do not normally contribute to electrical transport in graphene. In contrast, the π-bonds provide highly delocalized electrons which are free to move in the plane and it is these electrons that determine the band structure and conductivity in graphene. It must be noted that the π-orbitals are not assigned firmly to a particular *C-C* bond but are instead delocalized over a ring.

2.2 Electronic Band Structure of Graphene

The electronic properties of a material are intimately related to its band structure, particularly to its form near the Fermi energy. The band structure is generally referred to as the energy dispersion, $E(\boldsymbol{k})$ (i.e. how the energy of an electron varies as a function of crystal wave vector) of electrons within a material. To provide the necessary background for the discussion of transport properties in graphene, we will give a brief review of the band structure of π electrons for both monolayer and bilayer graphene. Although there are several approaches to calculate the electronic energy bands, here we focus on the widely used tight-binding approximation [20].

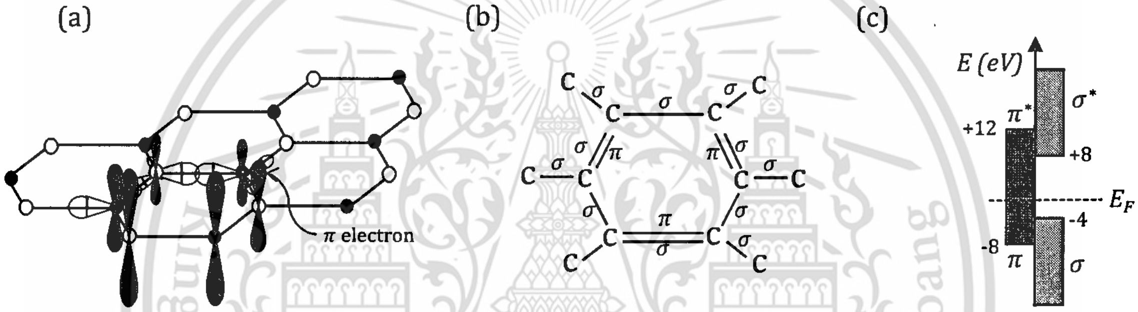

Figure 2.1: (a) Orbital structure of carbon atoms arranged in hexagonal rings. Each carbon atom has three in-plane sp^2 orbitals (blue color) and one $2p_z$ orbital (red) perpendicular to the sheet. (b) σ and π bonds formed from the overlap of sp^2 orbitals and $2p_z$ orbitals, respectively. (c) Large energy gap between bonding σ band and anti-bonding σ^* band due to sp^2 symmetric and anti-symmetric overlap. π band and anti-bonding π^* band which arise from symmetric and anti-symmetric overlap of $2p_z$ orbitals lie in the vicinity of the Fermi level (E_F) Consequently, the σ bonds are frequently neglected for the prediction of the electronic properties of graphene around the Fermi energy.

2.2.1 Single Layer Graphene

The honeycomb-arrangement of carbon atoms in graphene can be viewed as a triangular Bravias lattice with a basis of two atoms per unit cell, indicated by A and B. Figure 2.2(a) shows the lattice structure and the primitive unit cell with the A and B carbon atoms. The lattice vectors can be written as:

$$\boldsymbol{a_1} = \frac{a}{2}(3, \sqrt{3}), \qquad \boldsymbol{a_2} = \frac{a}{2}(3, -\sqrt{3}), \qquad (2.1)$$

where $a \approx 1.42$ Å is the distance between two nearest carbon atoms. In the reciprocal lattice, the first Brillouin zone is also hexagonal, as illustrated in Figure 2.2(b). The reciprocal lattice vectors are given by:

$$\boldsymbol{b_1} = \frac{2\pi}{3a}(1, \sqrt{3}), \qquad \boldsymbol{b_2} = \frac{2\pi}{3a}(3, -\sqrt{3})\,. \tag{2.2}$$

The six corners of the first Brillouin zone can be separated into two distinct but energetically degenerate points. These degenerate valleys are commonly referred to as the ***K*** and *K'* points. Their positions in momentum space are given by:

$$\boldsymbol{K} = \left(\frac{2\pi}{3a}, \frac{2\pi}{3\sqrt{3}a}\right), \qquad \boldsymbol{K'} = \left(\frac{2\pi}{3a}, \frac{2\pi}{-3\sqrt{3}a}\right). \tag{2.3}$$

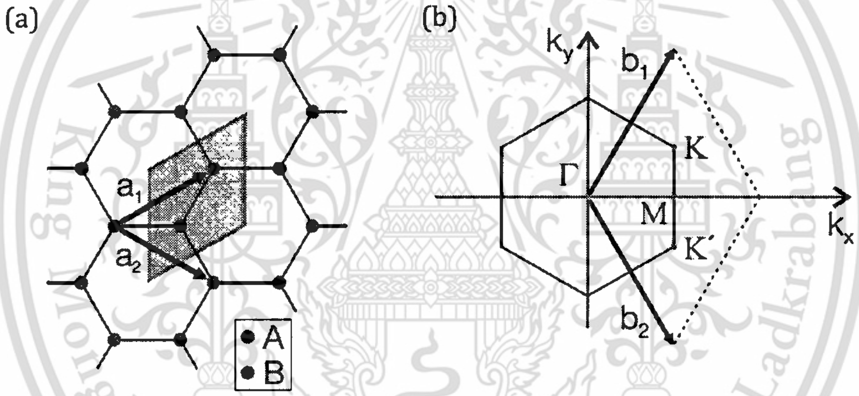

Figure 2.2: (a) Honeycomb structure of graphene lattice in real space. Two equivalent sublattices, A and B are represented by different colors. The primitive unit cell is shaded in grey and has the vector basis a_1 and a_2. (b) First Brillouin zone of the reciprocal lattice with the base vectors b_1 and b_2 and degenerate points *K* and *K'*.

The electronic band structure of single-layer graphene was first calculated by Wallace in 1947 [20] and others later [21, 22] using a tight-binding approximation. A more pedagogical derivation of this band structure can be found in Refs. [9, 20-26]. In this model, it is assumed that π electrons belonging to atoms in different sublattices are sufficiently tightly bound around their positions (although they are delocalized) and described by independent wave-functions that satisfy the Bloch theorem. This assumption finally leads to the energy dispersion of the graphene π-orbitals:

$$E(k_x, k_y) = \pm t\sqrt{1 + f(k)}, \tag{2.4}$$

where

$$f(k) = 4\cos\left(\frac{3a}{2}k_x\right) cos\left(\frac{\sqrt{3}a}{2}k_y\right) + 4\cos^2\left(\frac{\sqrt{3}a}{2}k_y\right). \tag{2.5}$$

The plus and minus sign refers to the upper (π*) and the lower (π) band, respectively. The energy dispersion of Eq. (2.4) is plotted in Figure 2.3. It consists of two symmetric bands: the valence band (lower π band) and conduction band (upper π* band), which touch each other at six corners of the Brillouin zone where the energy distribution vanishes (*E* = 0). Graphene is therefore a zero band-gap semiconductor and the points where the π band touches the π* band are referred to as the “Dirac” points. Each carbon atom has one π electron and each electron may occupy either spin-up or spin-down states. This results in the lower π band being completely filled and the upper π* band being completely empty. Thus, in the absence of external electric charges and at zero temperature, the Fermi level of intrinsic graphene lies at the Dirac points. The maximum energy at $k = 0$ can be estimated from Eq. (2.4) and $E_{max} \approx 8.4$ eV. When k is larger (higher energy), a saddle point is reached where the six K points merge into one Fermi surface (see Figure 2.3).

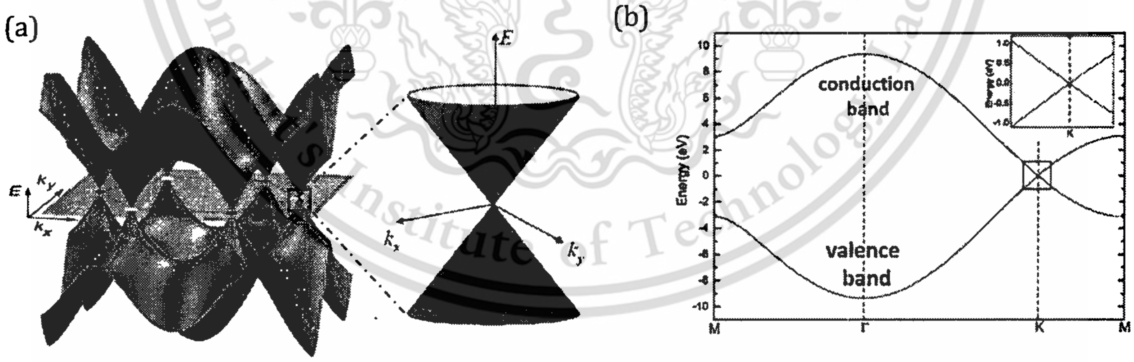

Figure 2.3: Energy dispersion of monolayer graphene obtained by the tight-binding approximation [8, 9]. (a) Energy spectrum in Brillouin zone with an expanded view of the energy bands close to one of the Dirac points. The band structure close to the Dirac points is referred to as the “Dirac cone” due to its shape. (b) The band structure along high symmetry points $M \rightarrow \Gamma \rightarrow K \rightarrow M$. Inset: enlargement in vicinity of Dirac point.

Typically, transport properties of charge carriers in any conductor are determined by the electronic states close to the Fermi level E_F. In the case of graphene, the states in the vicinity of the *K* or *K'* points are therefore relevant. In order to investigate this low-energy band structure, a linear expansion is made around *K* or *K'* point. By using the wave vector $\boldsymbol{k} = K + q$ (or $\boldsymbol{k} = K' + \boldsymbol{q}$), where $\boldsymbol{q}$ is the momentum measured relative to the *K* or *K'* point, and performing a Taylor expansion of the energy dispersion in Eq. (2.4) at that point, we obtain effective Hamiltonians H_K and $H_{K'}$ of the forms:

$$H_K = \hbar v_F \begin{pmatrix} 0 & q_x - iq_y \\ q_x + iq_y & 0 \end{pmatrix} \text{ and } H_{K'} = -\hbar v_F \begin{pmatrix} 0 & q_x + iq_y \\ q_x - iq_y & 0 \end{pmatrix}. \qquad (2.6)$$

Both Hamiltonians operate on $\phi = (\phi_A, \phi_B)^T$ where ϕ_A and ϕ_B are two components of wave-function ϕ on sublattice A and B, respectively. The eigenvalues of these Hamiltonians finally reduce to the following:

$$E = \pm\hbar v_F|\boldsymbol{k}|, \qquad (2.7)$$

where $v_F = \frac{3\gamma_0 a}{2\hbar} \approx 10^6$ m/s is Femi velocity, which is very large and energy-independent, in contrast to the case of an ordinary 2D semiconductor. Therefore, near the *K* and *K'* points the energy dispersion relation in single layer graphene has a linear dependence on wave vector (see Figure 2.3 and 2.4(a)).

In the tight-binding Hamiltonian, if we consider the next nearest neighbor hopping term t' where electrons hop in the same sublattice and include $t' \approx 0.1$ eV in the calculations, Eq. (2.4) becomes:

$$E = \pm t\sqrt{1 + f(\boldsymbol{k})} - t'(f(\boldsymbol{k}) - 2). \qquad (2.8)$$

The second term is the so-called trigonal warping, which breaks the electron-hole symmetry and shifts the energy of the Dirac points [9].

The density of states, which gives the number of available electronic states per energy and space, is given in single layer graphene as:

$$\rho(E) = \frac{4E}{2\pi(\hbar v_F)^2}, \qquad (2.9)$$

where the factor of four accounts for the spin and valley degeneracies [25]. The density of states of Eq. (2.9) is shown in Figure 2.4(b). Note that the density of states in single layer graphene has a linear dependence on energy and vanishes at zero energy (a direct consequence of the linear dispersion near the *K* points). This is quite different from conventional 2D systems where the density of states is constant.

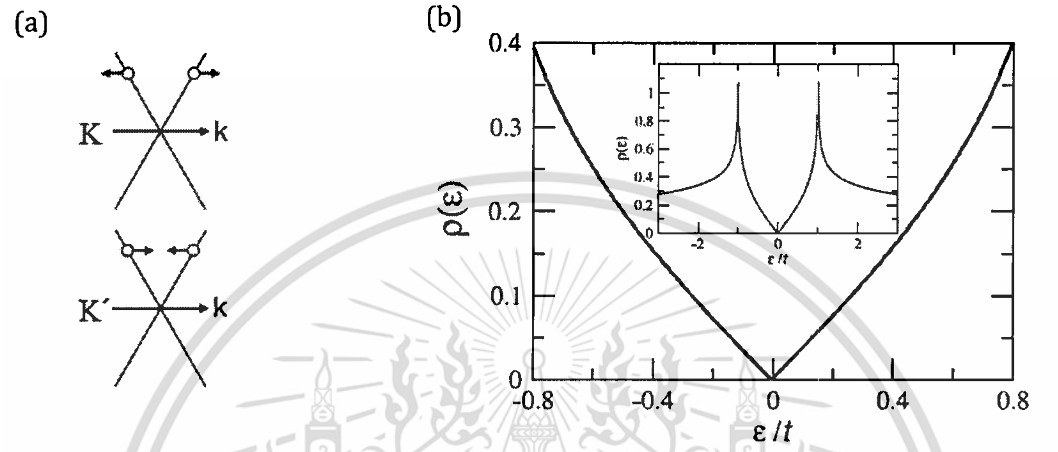

Figure 2.4: (a) Model energy dispersion $E = \pm\hbar v_F|\boldsymbol{k}|$ at *K* and *K'* points showing sublattice pseudospin. (b) Density of states of graphene close to the *K* point which can be approximated by $\rho(E) \propto |E|$. The inset shows the density of states over the full electron bandwidth [9].

2.2.3 Bilayer Graphene

Bilayer graphene is a system in which two monolayer graphene sheets are formed on top of one another. Depending on the orientation of the monolayers, there are two main means of stacking a graphene bilayer: (i) AA stacking and (ii) Bernal (AB) stacking [27]. In AA stacking, the atoms of the upper layer sit directly above those of the lower layer. AA stacking has been observed in epitaxial graphene [28] and results in two, parallel, 2D systems that may be treated as independent of each other [29]. In AB stacking, shown schematically in Figure 2.5, the B atoms in one layer are aligned on top of the A atoms of the other layer [30]. As a result, the unit cell of Bernal graphene consists of a basis of four atoms from different planes (A1, B1, A2 and B2). This bilayer structure is commonly found in 3D graphite and must be treated as a single 2D system [25] since interlayer hopping couples the two layers. In the following discussions we consider only AB stacking because of its relevance to the bilayer graphene devices discussed later in this thesis.

The most relevant hopping energies in AB-stacked bilayer graphene are shown in Figure 2.5(b). The intra-layer hopping energy between A1 (A2) and B1 (B2) in the lower (upper) layer is $\gamma_0 = t \approx 2.8$ eV. The inter-layer hopping is described by three coupling constants: $\gamma_1 \approx 0.4$ eV is the hopping energy between atom B1 and the A2, which sit on top of each other, $\gamma_3 \approx 0.3$ eV connects atom A1 and B2, which have no atom above or below, and the much smaller $\gamma_4 \approx 0.04$ eV determines the hopping energy between A1 (B1) and A2 (B2). γ_2 is not relevant for monolayer or bilayer graphene, as it describes next-nearest-layer hopping [31].

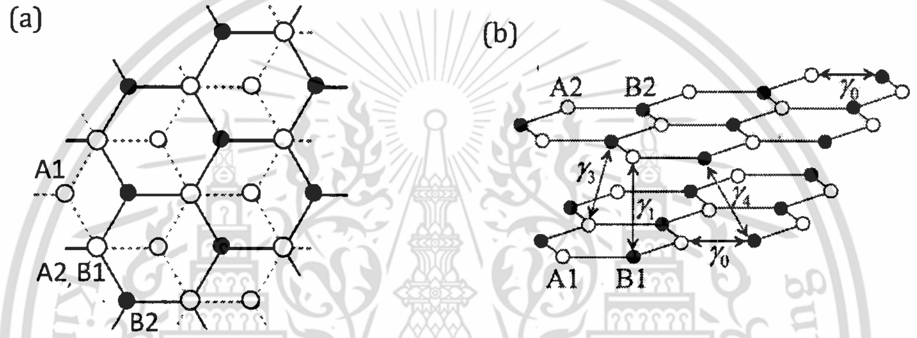

Figure 2.5: Lattice structure of AB-stacked bilayer graphene, which consists of two coupled monolayers of graphene and whose unit cell contains four equivalent carbon atoms: A1, B1, A2 and B2. (a) Top view. Atoms A2 and B1 sit directly on top of each other while atoms B2 of the lower layer and A1 of the upper layer have no atom above or underneath them. (b) Side view with its respective electronic hopping parameters: $\gamma_0(A1 - \mathrm{B1}, A2 - \mathrm{B2}), \gamma_1(\mathrm{B1} - \mathrm{A2}), \gamma_3(\mathrm{A1} - \mathrm{B2}), \gamma_4(\mathrm{A1} - \mathrm{A2}, \mathrm{B1} - \mathrm{B2}$ [9].

The electronic band structure of bilayer graphene is different from that of single-layer graphene even though it can be calculated by extending the tight-binding approximation for single-layer graphene [32–36]. Here, the hopping energies between neighbors in different layers are also considered, in addition to the hopping energy between in-plane nearest neighbors. For simplicity, we include only the interlayer hopping energies γ_0 and γ_1 in the calculation [9]. Finally, we obtain the set of four-band energy dispersions for bilayer graphene:

$$E_{\pm}(\boldsymbol{k}) = \pm\frac{\gamma_1}{2} \pm \frac{\gamma_1}{2}\sqrt{1 + \left(\boldsymbol{k} \cdot \frac{3\gamma_0 a}{\gamma_1}\right)^2}. \qquad (2.10)$$

For $\boldsymbol{k} \ll \gamma_1/(3\gamma_0 a)$, the bands are parabolic, whereas for $\boldsymbol{k} \gg \gamma_1/(3\gamma_0 a)$ they are linear. Figure 2.6 (a) shows the band structure of bilayer graphene calculated in Refs. [26, 30], in which the highest valence and lowest conduction band touch each other at the K and K' points at zero energy (zero band-gap). The second energy band is shifted by $\gamma_1 = \pm 0.4$ eV away from the E = 0 Fermi-level position. As mentioned above, the bands are indeed parabolic at small energies (small k) and become linear at higher energies (higher k). The cross-over between parabolic and linear dispersions was estimated to occur at a carrier density of $n \approx 5 \times 10^{12}$ cm^{-2} [25].

In the low-energy limit, only the upper valence band and lower conduction band are relevant and the energy dispersion of these bands is readily obtained from the secular determinant of the effective Hamiltonians H_K for the high symmetry K points:

$$H_K = -\frac{\hbar^2}{2m^*}\begin{pmatrix} \Delta & (k_x - ik_y)^2 \\ (k_x + ik_y)^2 & -\Delta \end{pmatrix}, \qquad (2.11)$$

where $m^* = \gamma_1/2{v_F}^2 \approx 0.03m_e$ is the effective mass (m_e is the electron mass) [25]. It must be noted that, in contrast to monolayer graphene, the carriers in bilayer graphene are "massive" with a small effective mass m^*. The energy quantity Δ, added in Eq. (2.11) for bilayer dispersion, corresponds to the possibility of a shift in electrochemical potential between the two layers (this term will become non-zero if a potential bias is applied between the layers). For Δ = 0 the operator in Eq. (2.11) has a similar structure to monolayer graphene, leading to a low-energy dispersion in bilayers which is non-Dirac-like and parabolic:

$$E = \pm\frac{\hbar^2 k^2}{2m^*}. \qquad (2.12)$$

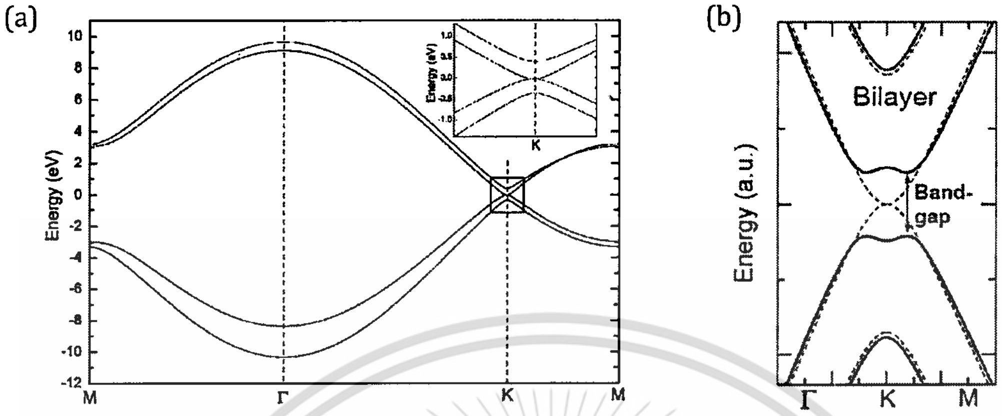

Figure 2.6: (a) The band structure of bilayer graphene along $\mathrm{M\Gamma KM}$ [8, 20]. The bands touch at zero energy at the K points. Inset shows the enlarged square region close to the K points. At higher energy, the bands become linear. The higher bands are shifted in energy by $\gamma_1 = \pm 0.4$ eV. (b) Band-gap opening induced by an applied perpendicular electric field in bilayer graphene [37, 41]. The dotted lines (solid lines) represent the band structure in the absence (presence) of the field.

If we lift the energy degeneracy between the carbon sublattices on the two layers, for example by applying an electric field perpendicular to the carbon-atom planes, then we will have $\Delta \neq 0$ and the energy dispersion will open an energy gap equal to 2Δ at each valley (E = 0) (see Figure 2.6(b)). This condition has been realized experimentally in double gated devices and it led to the discovery of a tunable band-gap (from metal to semiconductor) in bilayer graphene making it an interesting system for technological applications [37-49].

Another important distinction between single-layer and bilayer graphene is the density of states. While monolayer graphene has a density of states $\rho(E) \propto E$, in bilayer graphene the density of states is a constant [25] as in conventional two-dimensional electron gas systems (2DEG):

$$\rho(E) = \frac{4m^*}{2\pi\hbar^2} = const\,, \tag{2.13}$$

where m^* is the aforementioned effective mass and the factor of four accounts for the spin and valley degeneracies.

Chapter 3

Methodology

The next step in device fabrication after graphene exfoliation is the identification of graphene flakes on the substrate. Generally, it is found that there is plenty of graphite debris on the substrate, with large, shiny chunks of all shapes and colors, and also some highly transparent crystalline shapes having little color compared to the rest of the wafer. It is the latter that are possible candidates as useful thin graphene flakes. There are various methods available for locate, recognize and characterize of graphene. Optical microscopy, Raman spectroscopy and atomic force microscopy (AFM) are all widely used methods, and were also used in this work for flake identification. Therefore, in this chapter, we describe details of these three techniques.

3.1 Optical Microscopy

This is the most simple and efficient way for identification, in which surface of the substrate is carefully scanned in an optical microscope [50-58]. Thin flakes of graphene add to the optical path of reflected light which changes their color with respect to a clean wafer. The sensitivity of the human eye is maximal at 550 nm and oxide thickness ranging from 90 nm to 300 nm can give maximum reflected light intensity at this wavelength. Blake *et al.* used a model based on the Fresnel law to investigate the dependence of this color contrast on oxide thickness and light wavelength [50]. They have demonstrated that contrast can be maximized for any oxide thickness by using appropriate filters (Figure 3.1). For example, oxide thickness of approximately 90 nm and 280 nm are most appropriate, with the use of green filters, as well as without any filters, in white light. For this reason, standard 300-nm thick SiO_2 was used as the substrate in our work for deposition of the graphene flakes.

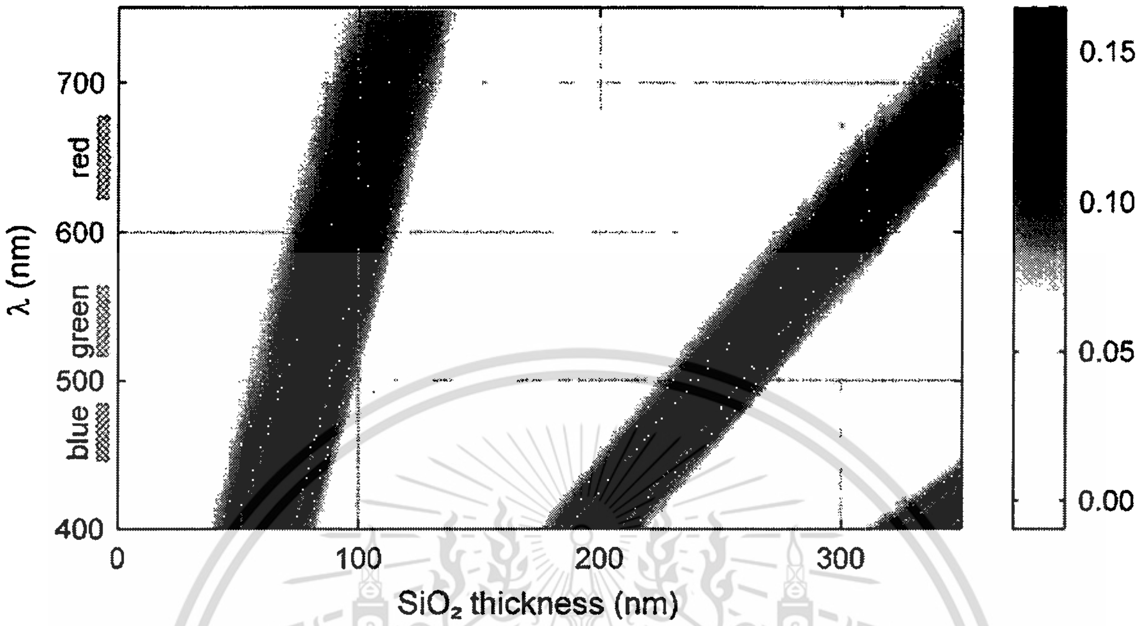

Figure 3.1: Contour plot of contrast as a function of wavelength and SiO2 thickness. Color scale on the right shows the expected contrast [50].

In our process of evaluation, the entire chip is first scanned at 20x magnification to find areas that look green, and then magnified to 50x in those areas to locate flakes that appear light purple under this magnification. The flake is then checked at 100x magnification, for which its shape and thickness is easier to ascertain. Photographs of the flake at each of these magnifications are taken, with special attention paid to ensure that at 20x the flake and its four surrounding markers are all included in the picture, thereby allowing efficient design of the AutoCAD file for EBL processing which will be performed later.

3.2 Raman Spectroscopy

Raman spectroscopy is a fast and non-destructive technique for the high resolution characterization of carbon structures [62]. It also gives the most structural and electronic information. This spectroscopic method is based on inelastic scattering of monochromatic light, usually from a laser source. The laser light interacts with molecular vibrations, phonons or other excitations in the sample, causing the energy of the reemitted laser photons to be shifted up or down (Raman effect). This shift in energy provides information about vibrational, rotational, or other low frequency modes in the sample.

Plotting the intensity of this shifted energy versus frequency results in a Raman spectrum of the sample. It typically involves illuminating sample with the laser beam and collecting back the light from the illuminated spot with a lens. This light is sent through a monochromator where wavelengths close to laser line due to elastic Rayleigh scattering are filtered out and rest of the collected light is dispersed onto a detector.

The Raman spectra of carbon materials show common features in the range of 800-2000 cm^{-1}, with two peaks, the G and D peak, that are located near 1560cm^{-1} and 1360 cm^{-1} respectively. The G peak arises from the doubly degenerate E_{2g} phonon at the center of the Brillouin zone of the carbon atoms, and the D peak is due to breathing modes of sp^{2} atoms and requires a defect for its activation. This peak is generally absent for high quality graphene samples due to the absence of defects and can only be seen at the edges of the sample [63]. However, the most prominent feature of graphene's Raman spectrum is the second-order D peak (also referred as 2D) which changes in shape, width, and position for an increasing number of layers, reflecting the change in the electron bands due to second-order resonant Raman scattering from zone boundary K+ ΔK phonons [61-67].

Graphene has a sharp, single 2D peak with full width at half maximum (FWHM) around 30 cm^{-1}, in contrast with graphite and few-layer graphene which both show a broad peak consisting of two sub-peaks (2D1 and 2D2). A significant downshift in the position of the G peak, and an upshift in the 2D peak, has also been observed with an increasing number of graphene layers. A few early experiments [61, 66] suggested that the intensity ratio of I(2D)/I(G) can be used to estimate the number of layers, but this was contradicted later in further experiments [65]. Nonetheless, Raman spectroscopy can clearly distinguish single layer graphene, from its bilayer and few- (less than 5) layer counterparts. Beyond 5 layers, the spectrum becomes largely indistinguishable from that of bulk graphite (Figure 3.2).

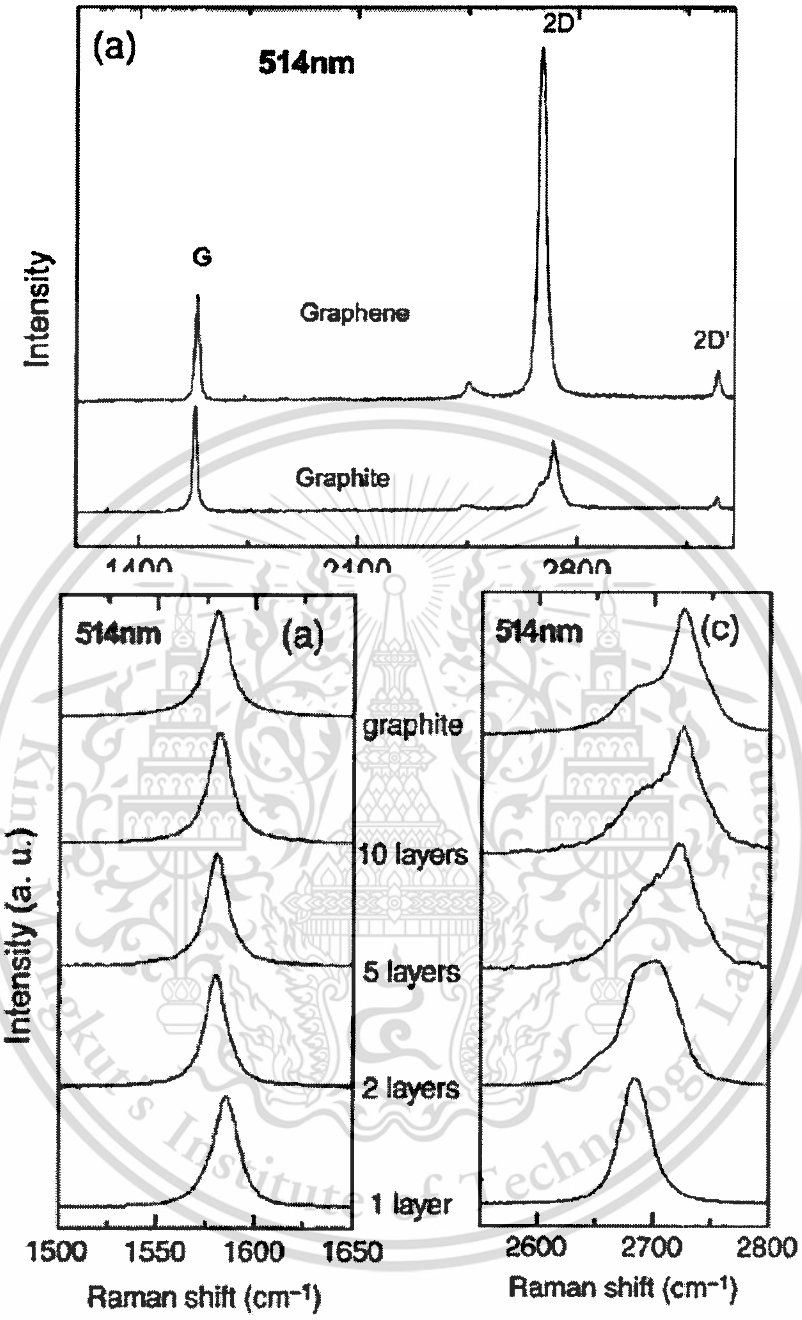

Figure 3.2: (Top) Raman spectra of graphene and graphite measured at 514 nm. (Bottom) shows the evolution of G and 2D peaks as a function of number of layers, respectively [63, 64].

3.3 Atomic Force Microscopy (AFM)

AFM is one technique that can be used to establish that graphene flakes are really one atomic-layer thick. The thickness of a single layer of graphene on crystalline graphite is typically 0.4 nm, but monolayer of graphene on oxidized wafers consistently appear to be 0.8 - 1.2 nm in thickness in AFM measurements. This origin of this extra thickness is unclear as it cannot be caused by van der Waals interaction between the substrate and graphene. It may be due to a water film that can be present in between the graphene film and the SiO_2 surface during the graphene deposition, which is always done in a cleanroom under ambient conditions (humidity of 45 – 50 %).

It has been shown by Wo *et al.* in their work on organic pentacene deposited on SiO_2 that if an interfacial water layer is present on the oxide surface, its thickness is about 0.75 nm [59]. Also, graphene is hydrophobic and a hydration layer (~ 0.15 nm in thickness) is expected to form at its interface with water. This uncertainty about the nature of 0.8 nm thick graphene sheets was cleared by studying self-folded sheets [60] or combining AFM with micro-Raman spectroscopy [61]. While AFM suffers from disadvantages of being slow, and limited in lateral scan size it is nonetheless the best way to monitor the topological quality of substrate-supported graphene. Figure 3.3 shows an AFM image of monolayer graphene on SiO_2. The step height is ~ 0.8 nm, as generally observed in most AFM measurements of single-layer graphene.

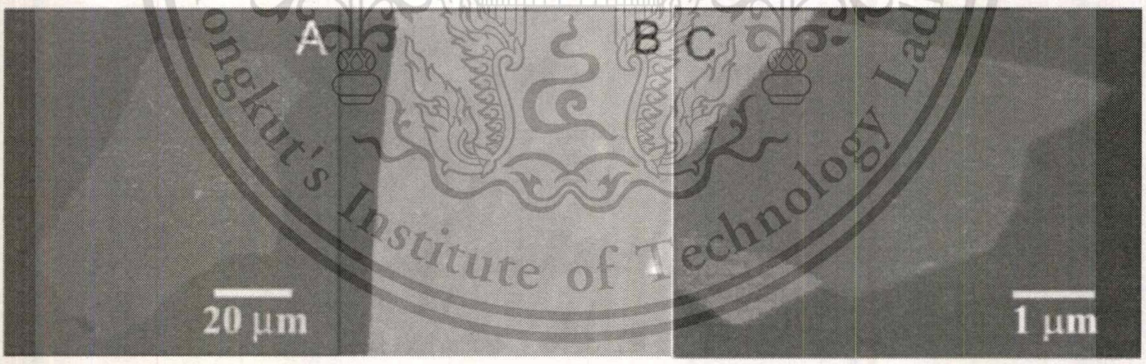

Figure 3.3 (A) Optical image of a multilayer graphene flake with thickness ~ 3 nm on top of SiO_2 substrate. (B) AFM image of 2 µm by 2 µm area of this flake near its edge. Colors: dark brown, SiO_2 surface; orange, 3 nm height above the SiO_2 surface. (C) AFM image of single layer graphene. Color: dark brown, SiO_2 surface; brown-red (central area), 0.8 nm height; yellow-brown (bottom left), 1.2 nm; orange (top left), 2.5 nm. Notice the folded part of the film near the bottom, which exhibits a differential height of ~ 0.4 nm. Adopted from [3].

Chapter 4

Results and Discussions

In this chapter we present the results obtained from our study on identifying graphene flakes using optical microscopy, Raman spectroscopy techniques and atomic force microscopy (AFM). We start the chapter with the discussion on how we identify suitable graphene flakes by visual inspection under an optical microscope. We then proceed to discuss the results obtained from Raman spectroscopy and AFM techniques. We also comment a little on the similar results of the three techniques.

4.1 Optical Microscopy

In our process of evaluation, the entire chip is first scanned at 20x magnification to find areas that look green, and then magnified to 50x in those areas to locate flakes that appear light purple under this magnification (Figure 4.1 & 4.2). The flake is then checked at 100x magnification, for which its shape and thickness is easier to ascertain. Photographs of the flake at each of these magnifications are taken, with special attention paid to ensure that at 20x the flake and its four surrounding markers are all included in the picture, thereby allowing efficient design of the AutoCAD file for EBL processing which will be performed later

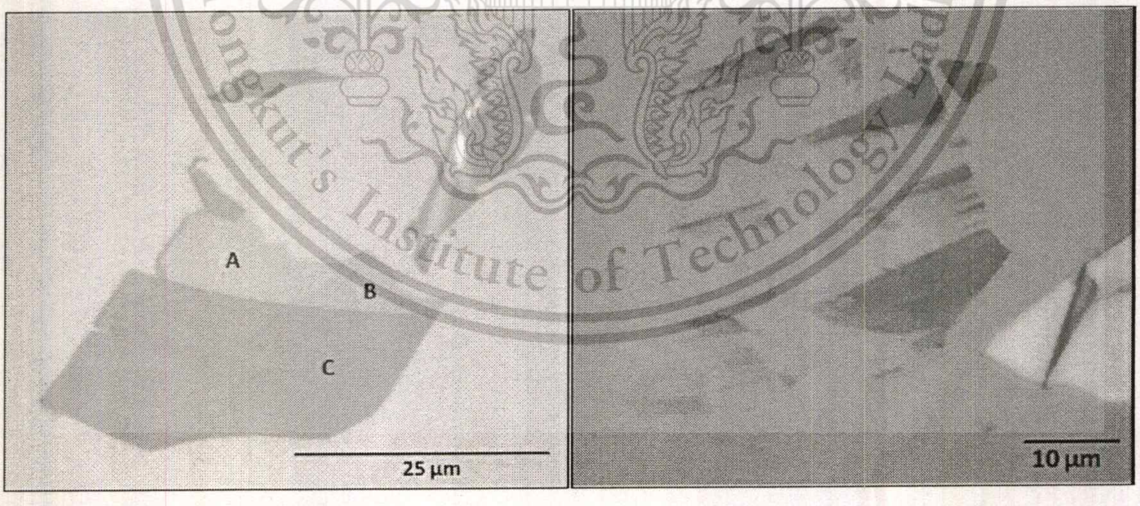

Figure 4.1: Optical images of two different graphene samples obtained from natural graphite and deposited onto a Si/SiO$_2$ substrate. The images show a change in visibility of graphene with different number of layers. A, B and C show mono, bi- and few layer graphene, respectively.

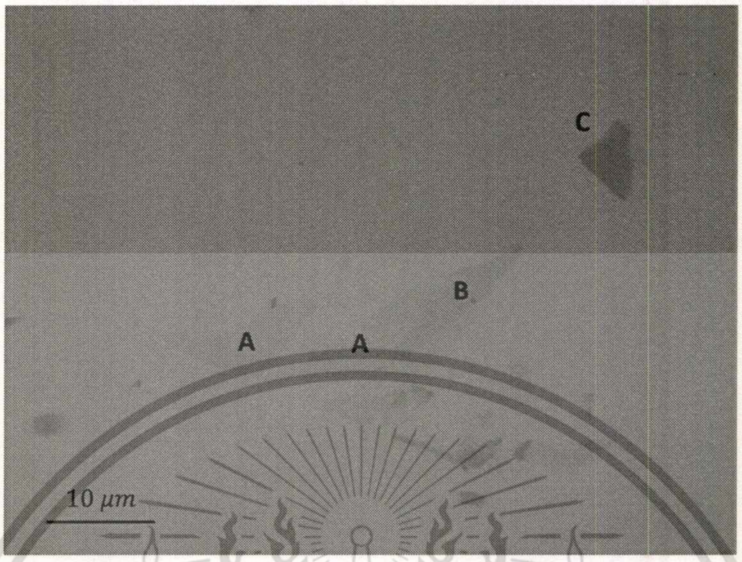

Figure 4.2: Optical images of monolayer (A), bilayer (B) and many-layer (C) graphene obtained from Kish graphite and deposited on a Si/SiO$_2$ substrate. Note the relative contrast of these layers.

4.2 Raman Spectroscopy

Raman spectra of our samples were measured at room temperature under a 514 nm excitation wavelength. The resulting spectra of a few representative graphitic materials: monolayer, bilayer and many-layer graphene are shown in Figure 4.3. The two most prominent features, which are the *G* peak at 1582 cm^{-1} and the *2D* band at around 2700 cm^{-1} are clearly distinguishable here. The G peak is a first-order intra-valley Raman scattering, which associated with the doubly degenerate (LO and iTO) phonon mode (E_{2g}) at the Brillouin zone center (Γ point), while the 2D peak is a two-phonon, inter-valley, double resonance process of the iTO phonon mode near the zone-boundary (K point). In disordered graphite, such zone-boundary phonons (iTO phonon mode) also give rise to the D peak at ~1360 cm^{-1}, which is basically second-order inter-valley scattering process (scattering from K to K' (or K' to K) point). This peak consists of iTO phonon emission and an elastic scattering due to the lattice defect with $\boldsymbol{q}$ vectors connecting K and K' points. As a result, the crystal quality of graphene can be quantified by making use of the D peak. In samples with high densities of defects or impurities, the D peak is commonly seen. Note that the 2D peak is not an overtone mode of the D peak since defect scattering is not involved for the former.

The number of layers in a graphene flake can be identified [61, 63-68] either from the intensity of the G peak, which increases with the number of layers, or from the downshift of the G peak and the upshift of 2D peak with increasing layer number. However, doping in graphene is also found to shift the position of the G and 2D peaks [69] and may also cause changes in their intensity. Therefore, probing the number of layers via this approach is rather unreliable. A more reliable way is to instead use the shape of the 2D peak, more specifically the number of Lorentzians required to fit this peak. In monolayer graphene, the 2D peak is narrow and comprised of a single Lorentzian, while in bilayer graphene it is much broader and up-shifted with respect to monolayer graphene. As can be seen in Figure 4.3, our results for different graphene samples exhibit the characteristics described above. The 2D band of the bilayer graphene has four Lorentzian peaks as shown in Figure 4.4, where we show a Lorentzian peak fitting performed on the *2D* peak of another bilayer sample of ours. For larger numbers of layers, two Lorentzians are generally found although these become almost in distinguishable.

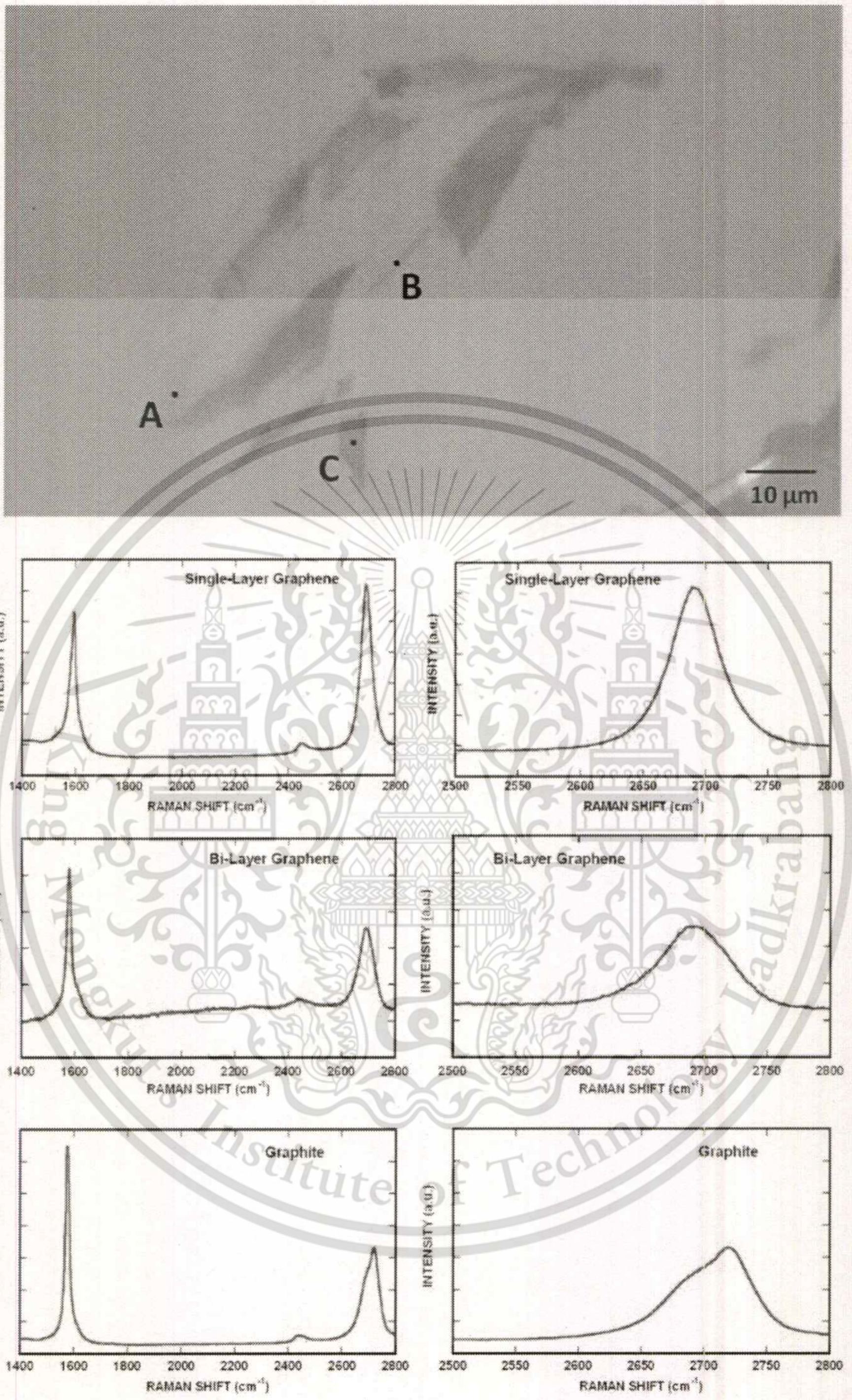

Figure 4.3: Raman spectra for flakes shown in the optical image. A, B and C show the area where spectra for mono, bi- and graphite were taken, respectively. (Left) Complete spectra for single, Bi-layer, and graphite respectively, from top to bottom. (Right) 2D peak of the Raman spectrum.

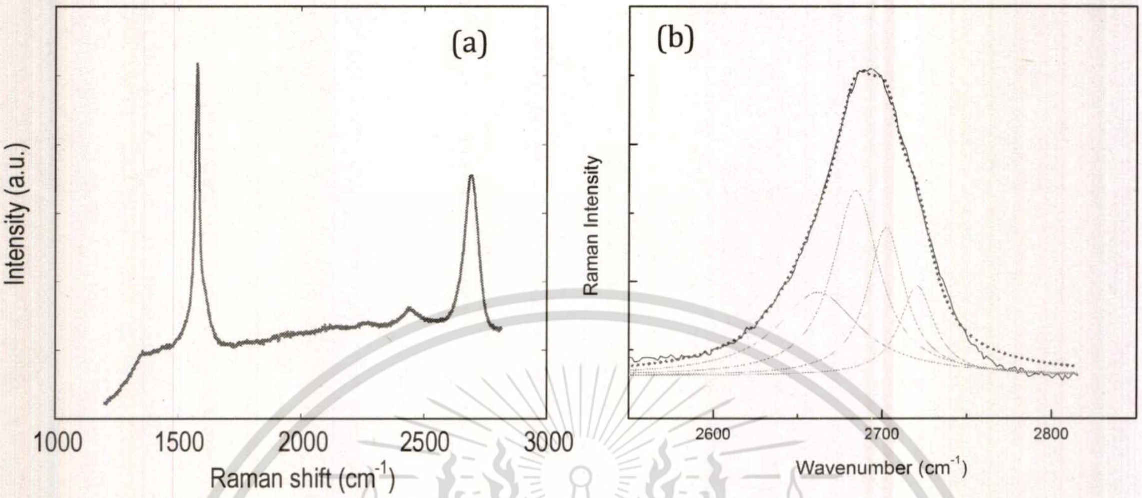

Figure 4.4: The Raman spectrum of graphene on a Si/SiO$_2$ substrate, taken with a green laser (514.5 nm). (a) Comparison of monolayer, bilayer and many-layer graphene (indicated), showing the evolution of the G and 2D peaks as a function of the number of layers. (b) An enlargement of the 2D peak, showing its four Lorentzians, for bilayer graphene.

4.3 Atomic Force Microscopy (AFM)

We performed AFM on one of our monolayer sample deposited on 500 nm of SiO$_2$ and the result is showed in Figure 4.5. The step height obtained here is ~ 0.8 nm, as generally observed in most AFM measurements of single-layer graphene. This result therefore can be used to confirm the results obtained from optical microscopy and Raman spectroscopy.

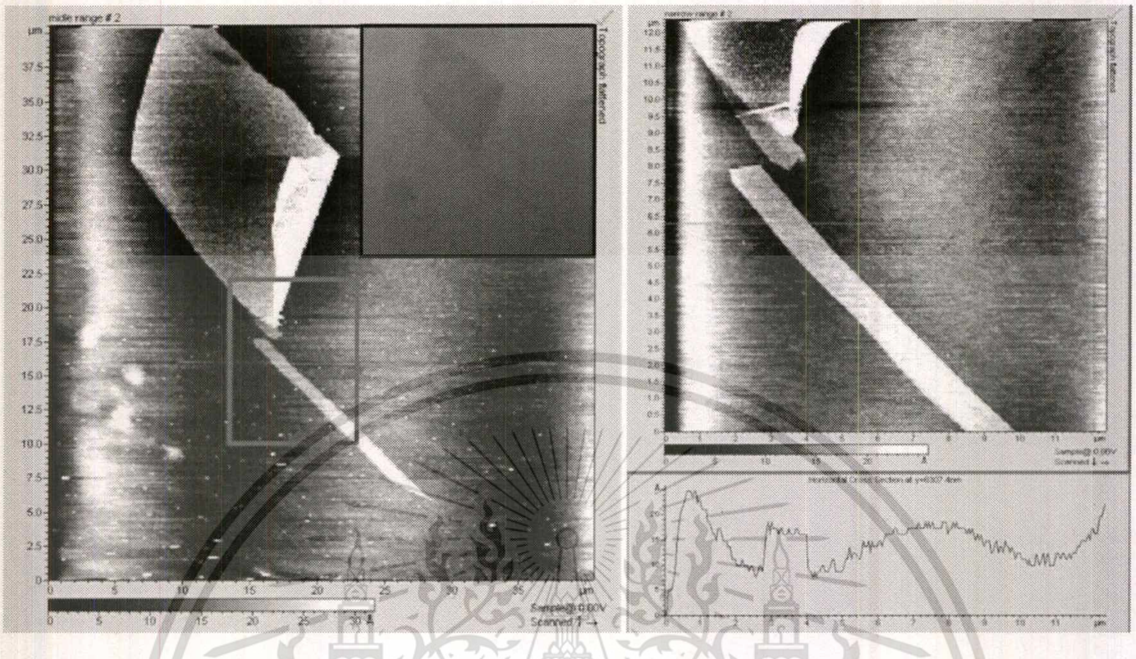

Figure 4.5: (Left) AFM of a single layer of graphene on SiO_2. Inset shows the optical image of the scanned area. (Right) AFM scan of the area indicated by red rectangle in the left image. The step height is ~ 0.8 nm when scanned along the green line.

Chapter 5

Summary and Outlook

In the course of this work, we have studied the techniques of optical microscopy, Raman spectroscopy and atomic force microscopy (AFM) and used them to identify graphene flakes on Si/SiO_2 substrate. These three techniques are most commonly used since they are simple and reliable. By using these approaches, we were able to determine the number of graphene layers properly. For example we were able to classify monolayer, bilayer, tri-layer and many-layer graphene. These techniques therefore are very useful for study physical properties of each category since they have very distinct properties theoretically. The proper identification of graphene layers will in turn help in understanding the appropriate application that they can be used for. The key findings of our experimental studies were as follows:

- Of all the techniques for identification the optical microscopy method is the safest and the most straightforward approach
- The throughput of optical method is high compare to other techniques although there is some chance for inducing human error
- To offset the minor drawback of optical microscopy, Raman spectroscopy can be used for additional confirmation
- Both optical microscopy and Raman spectroscopy are noninvasive method and therefore to not damage the sample
- AFM on the other hand can be a destructive method but at the same time might be needed for studying layer uniformity in addition to determine the layer thickness

Chapter 6

Output

This grant has been utilized for the study of graphene identification using optical microscopy and Raman spectroscopy the result of which is included in the following publications:

[1] G. He, K. Ghosh, U. Singisetti, H. Ramamoorthy, R. Somphonsane, G. Bohra, M. Matsunaga, A. Higuchi, N. Aoki, S. Najmaei, Y. Gong, X. Zhang, R. Vajtai, P. M. Ajayan, and J. P. Bird, “*Conduction Mechanisms in CVD-Grown Monolayer* MoS_2 *Transistors: From Variable-Range Hopping to Velocity Saturation*”, Nano Lett. **15**, 5052 (2015)

[2] D. K. Ferry, R. Somphonsone, H. Ramamoorthy, and J. P. Bird, “*Plasmon-mediated energy relaxation in graphene*” Appl. Phys. Lett. **107**, 262103 (2015)

[3] D. K. Ferry, R. Somphonsone, H. Ramamoorthy, and J. P. Bird, “*Energy relaxation of hot carriers in graphene via plasmon interactions*” J. Comput. Electron. **15**, 144-153 (2016)

[4] B. Liu, R. Akis, D. K. Ferry, G. Bohra, R. Somphonsone, H. Ramamoorthy, and J. P. Bird, “*Conductance fluctuations in graphene in the presence of long-range disorder*” J. Phys.: Condens. Matter **28**, 135302 (2016)

[5] HRamamoorthy .,,nsaneSompho .R J. Radice, ,He .GC.-P. Kwan, Bird .P .and J “*"Free-ing" Graphene from its Substrate: Observing Intrinsic Velocity Saturation with Rapid Electrical Pulsing*” Nano Lett. **16**, 399–403 (2016)

[6] R. Somphonsane, H. Ramamoorthy, G. He, J. Nathawat, C.-P. Kwan, Y.-H. Lee, J. Fransson, and J. P. Bird “*Evaluating the contribution of impurities and phonons to the resistivity of graphene by differential-conductance mapping*” Phys. Rev. B (2016, under revision)

[7] G. He, H. Ramamoorthy, C.-P. Kwan, Y.-H. Lee, J. Nathawat, R. Somphonsane, M. Matsunaga, A. Higuchi, N. Aoki, Y. Gong, X. Zhang, R. Vajtai, P. M. Ajayan, and J. P. Bird "*Thermally-Assisted Nonvolatile Memory in Monolayer* MoS_2 *Transistors*" Nature Nanotech. (2016, under review)

Bibliography

[1] Fuechsle, M. *et al. Nature Nanotech.* **7,** 242-246 (2012).

[2] Avouris, P. *et al. Nature Nanotech.* **2,** 60-614 (2007).

[3] Novoselov, K. S. *et al. Science* **306,** 666-669 (2004).

[4] Novoselov, K. S. *et al. Proc. Natl. Acad. Sci. USA* **102,** 10451-10453 (2005).

[5] Geim, A. K. *et al. Scientific American*, 90-97 (April 2008).

[6] Katsnelson, M. I. *et al. Materials Today* **10,** 20-27 (2007).

[7] Geim, A. K. *et al. Nat. Materials* **6,** 183-191 (2007).

[8] Geim, A. K. *et al. Science* **324,** 1530-1534 (2009).

[9] Castro Neto, A., H. *et al. Rev. Mod. Phys.* **81,** 109- 162 (2009).

[10] Sarma, S. Das *et al. Rev. Mod. Phys.* **83,** 407-470 (2011).

[11] Novoselov, K. S. *et al. Nature* **438,** 197-200 (2005).

[12] Zhang, Y *et al. Nature* **438,** 201-204 (2005).

[13] Novoselov, K. S. *et al. Nat. phys.* **2,** 177-180 (2005).

[14] Adam, S. *et al. Proc. Natl. Acad. Sci. USA* **104,** 18392-18397 (2007).

[15] Tan, Y. W. *et al. Phys. Rev. Lett.* **99,** 26803 (2007).

[16] Chen, J. H *et al. Nat. Phys.* **4,** 377-381 (2008).

[17] Morozov, S. V. *et al. Phys. Rev. Lett.* **97,** 016801 (2006).

[18] Katsnelson, M. I. *et al. Nat. Phys.* **2,** 620- 623 (2006).

[19] Young, A. F. *et al. Nat. Phys.* **5,** 222-226 (2009).

[20] Wallace, P. R. *Phys. Rev.* **71**, 622-634 (1947).

[21] McClure, J. W. *Phys. Rev.* **108**, 612-618 (1957).

[22] Slonczewski, J. C., and Weiss, P. R. *Phys. Rev.* 109, 272-279 (1958).

[23] Abergel, D. S. L. et al. *Advances in Physics* 59, 261-482 (2010).

[24] Schönenberger, C. *Bandstructure of graphene and carbon nanotubes: An exercise in condensed matter physics* (2010).

[25] Sarma, S. Das et al. *Rev. Mod. Phys.* **83**, 407-470 (2011).

[26] Partoens, B. et al. *Phys. Rev. B* 74, 075404 (2006).

[27] Charlier, J.-C. *et al. Phys. Rev. B* **46**, 4531-4539 (1992).

[28] Lauffer, P. *et al. Phys. Rev. B* **77**, 155426 (2008).

[29] Poncharal, P. *et al. Phys. Rev. B* **78**, 113407 (2008).

[30] Latil S. *et al. Phys. Rev. Lett.* **97**, 036803 (2006).

[31] Dresselhaus, M. S.; and Dresselhaus, G. *Adv. Phys.* **51**, 1-186 (2002).

[32] McCann, E.; and Fal'ko, V. I. *Phys. Rev. Lett.* **96,** 086805 (2006).

[33] McCann, E. *Phys. Rev. B* **74**, 161403(R) (2006).
[34] McCann, E. *et al. Eur. Phys. J. - Special Topics* **148**, 91-103 (2007).
[35] McCann, E. *et al. Solid State Commun.* **143**, 110-115 (2007).
[36] Min, H. *et al. Phys. Rev. B* **75**, 155115 (2007).
[37] Castro, E. V. *et al. Phys. Rev. Lett.* **99**, 216802 (2007).
[38] Oostinga, J .B. *et al. Nature Mate.* **7**, 151-157 (2008).
[39] Zhang, Y. *et al. Nature* **459**, 820-823 (2009).
[40] Deshpande A. *et al. Appl. Phys. Lett.* **95**, 243502 (2009).
[41] Avouris, P. *Nano Lett.* **10,** 4285-4294 (2010).
[42] Avetisyan, A. A. *et al. Phys. Rev. B* **81**, 115432 (2010).
[43] Kuzmenko, A. B. *et al. Phys. Rev. B* **80**, 165406, (2009).
[44] Mak, K. F. *et al. Phys. Rev. Lett.* **102**, 256405 (2009).
[45] Ohta, T. *et al. Science* **313**, 951-954 (2006).
[46] Taychatanapat, T.; and Jarillo-Herrero, P. *Phys. Rev. Lett.* **105**, 166601 (2010).
[47] Xia, F. *et al. Nano Lett.* **10**, 715-718 (2010).
[48] Zhang, L. M. *et al. Phys. Rev. B* **78**, 235408 (2008).
[49] Zou, K.; and Zhu, J. *Phys. Rev. B*, **82**, 081407 (2010).
[50] Blake, P. *et al. Appl. Phys. Lett.* **91,** 063124 (2007).
[51] Abergel, D. S. L. *et al. Appl. Phys. Lett.* **91,** 063125 (2007).
[52] Roddaro, S. *et al. Nano Lett.* **7,** 2707-2710 (2007).
[53] Ni, Z. H. *et al. Nano Lett* **7,** 2758-2763 (2007).
[54] Reina A. *et al. J. Phys. Chem. C* **112,** 17741–17744 (2008).
[55] Teo, G. *et al. J. Appl. Phys.* **103,** 124302 (2008).
[56] Gao, L. *et al. ACS Nano* **2,** 1625-1633 (2008).
[57] Song, E. B. *et al. Appl. Phys. Lett.* **96,** 081911 (2010).
[58] Soldano, C. *et al. Carbon* **48,** 2127-2150 (2010).
[59] Wo, S. *et al. J. Appl. Phys.* **100,** 093504 (2006).
[60] Li, L *et al.* Carbon **44,** 1544-1547 (2008).
[61] Gupta, A. *et al. Nano Lett.* **6,** 2667-2673 (2006).
[62] Ferrari, A. C. *et al. Phil. Trans. Roy. Soc. A* **362,** 2267-2565 (2004).
[63] Ferrari, A. C. *et al. Phys. Rev. Lett.* **97,** 187401 (2006).
[64] Ferrari, A. C. *Sol. St. Comm.* **143,** 47-57 (2007).
[65] Casiraghi, C. *et al. Appl. Phys. Lett.* **91**, 233108 (2007).
[66] Graf, D. *et al. Nano Lett.* **7,** 238 (2007).
[67] Malard, L. M. *et al. Physics Reports* **473,** 51-87 (2009).

[68] Wang, Y. Y. *et al. J. Phys. Chem. C* **112**, 10637–10640 (2008).

[69] Ni, Z. *et al. Nano Lett.* **10**, 3868-3872 (2010).

Appendix

Conductance fluctuations in graphene in the presence of long-range disorder

IOP Publishing
Journal of Physics: Condensed Matter
J. Phys.: Condens. Matter **28** (2016) 135302 (7pp)
doi:10.1088/0953-8984/28/13/135302

Conductance fluctuations in graphene in the presence of long-range disorder

Bobo Liu[1], Richard Akis[1], David K Ferry[1], Girish Bohra[2], Ratchanok Somphonsane[3], Harihara Ramamoorthy[2] and Jonathan P Bird[2]

[1] School of Electrical, Computer, and Energy Engineering, Arizona State University, Tempe, AZ 85287, USA
[2] Department of Electrical Engineering, the University at Buffalo, Buffalo, NY 14260, USA
[3] Department of Physics, King Mongkut's Institute of Technology Ladkrabang, Bangkok 10520, Thailand

E-mail: ferry@asu.edu

Received 13 August 2015, revised 14 October 2015
Accepted for publication 30 October 2015
Published 4 March 2016

CrossMark

Abstract

The fluctuations in the conductance of graphene that arise from a long-range disorder potential induced by random impurities are investigated with an atomic tight-binding lattice. The screened impurities lead to a slow variation of the background potential and this varies the overall potential landscape as the Fermi energy or an applied magnetic field is varied. As a result, the phase interference varies randomly and leads to fluctuations in the conductance. Recently, experiments have shown that an applied magnetic field produces a remarkable reduction in the amplitude of these conductance fluctuations. We find qualitative agreement with these experiments, and it appears that the reduction in magnetic field of the fluctuations arises from a field induced smoothing of the conductance landscape.

Keywords: graphene, conductance, fluctuations, transport

(Some figures may appear in colour only in the online journal)

1. Introduction

The phenomenon of fluctuations in the conductance of a disordered metal or semiconductor at low temperature has been studied for many years [1]. In such systems, it is observed that the conductance will exhibit such fluctuations as the Fermi energy, or an applied magnetic field, is varied. It is presumed that this arises from the variations in the local potential landscape and changes in the electron wave interference as these variations are introduced. Recently, these fluctuations have been observed in monolayer and bilayer sheets of graphene [2–8]. In some of these experiments, it was found that the fluctuations observed [9] for varying magnetic field were smaller than for varying the gate voltage (energy) and decreased as the density increased [7–9]. These behaviors are contrary to the idea of ergodicity[4] which arose from early diagrammatic theories for fluctuations in disordered materials [10], and from recent theories for graphene in the metallic regime of high conductivity [11–13]. However, such behavior has been observed in some simulations of the fluctuations in normal semiconductors [14, 15]. It was originally suggested that this reduction of the amplitude with magnetic sweeps was due to the breaking of microscopic symmetries connected with the detailed electronic structure of the graphene itself. However, some of these symmetries could be expected to be broken by the in-plane magnetic field as well, and this was not observed [9].

Motivated by the experimental situation described above, we have undertaken simulations of quantum transport in graphene to investigate the connection of the conductance fluctuations (CF) to the nature of the disorder potential. With a very short-range atomic potential used to simulate the disorder, no decay of the fluctuation amplitude with magnetic field was observed [16, 17]. In these earlier calculations, an atomic-basis tight-binding lattice also was used to study the structure and transport in a graphene nanoribbon. The random potential was introduced via a local potential in the Anderson model [18], an approach that we have used successfully for finite difference lattices in the past [14, 15]. But, this potential appears

---

[4] The term ergodic in this context would mean that the amplitude would be independent of which physical variable (energy, magnetic field, sample, etc) was varied.

0953-8984/16/135302+7$33.00

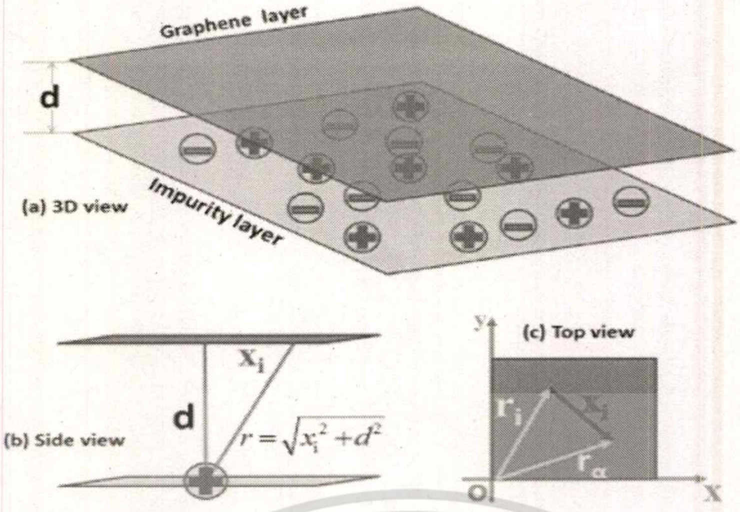

Figure 1. A typical schematic of remote charge impurity. (a) 3D view: the distance between graphene layer and impurity layer is d and the positive and negative impurity charges are randomly located within the impurity layer. (b) Side view: the distance between the impurity charge and the point where potential is calculated is r. (c) Top view: the distance between the impurity charge and the point where potential is calculated is obtained by $|\mathbf{r}_a - \mathbf{r}_i|$.

to be too short range for the atomic-basis lattice, a point we return to later. On the other hand, it has been pointed out that a long-range potential, appropriate to describe the potential induced by remote impurities trapped beneath the graphene sheet, is an important approach [13]. Hence, we have used here a long-range potential which derives from the impurities trapped below the graphene sheet in/on the silicon dioxide substrate. In the following, we briefly first describe our simulation approach, and then discuss how the results give agreement with available experimental data.

2. Impurities and the simulation approach

One of the critical factors for fluctuations is the types of extrinsic scattering sources that can exist in graphene ribbons. Although the scattering scenario is a complicated picture with contributions from adsorbates, ripples, corrugations and remote charged impurities, etc, here we consider only the long-range Coulomb potential arising from the random distribution of charged impurities. The resulting disordered potential will be the main scattering mechanism, at least as based upon experimental evidence [19–21]. Utilizing the superposition principle, the total electric potential of all charged impurities is simply the sum of potentials due to the individual charged impurities, which can be described in a form [21]

$$V_\alpha = \sum_{i=1}^{N_i} \frac{1}{4\pi\varepsilon_0\varepsilon_r}\frac{e_i}{\sqrt{|r_\alpha - r_i|^2+d^2}}\exp\left(-\xi\cdot\sqrt{|r_\alpha - r_i|^2+d^2}\right). \tag{1}$$

Here, N_i is the number of the impurities, ε_0 is the vacuum permittivity, and the relative permittivity is ε_r. e is the elementary electric point charge which may have a different sign for different impurities. The exponential term $\exp\left(-\xi\sqrt{|\mathbf{r}_a - \mathbf{r}_i|^2+d^2}\right)$ represents the modification of the potential by both the screening and the set-back of the impurity from the graphene sheet. Here, ξ is the screening coefficient [22]. The distance between the point charge and the position where potential $V(r)$ is calculated is the argument of the square root term in the exponential. We use a constant screening, which has been shown to comparable to a density-dependent screening in terms of fluctuation amplitudes [13]. Important parameters are illustrated in figure 1.

We use an atomic-basis tight-binding model to study the transport with such a long-range potential. The atoms are treated in slices, which contain two atomic rows in order to preserve the slice symmetry [16]. The graphene nanoribbon sample used in our calculation has a width of 199 atoms and a length of 200 columns (100 slices). So the area of the sample will be around 24.3 nm (width) × 42.4 nm (length) = 1030.32 nm^2 (we refer to this as the 'normal' size). We consider a density of impurities of 3×10^{12} cm^{-2}. This means that the number of charged impurities in the area of the ribbon is 31. Then, these impurity charges are randomly distributed throughout the area of the graphene nanoribbon. In addition, the distance between the graphene layer and the impurity charge layer is set to $d = a_0$ and the screening coefficient is $\xi = 1/(10 \times a_0)$, corresponding to a screening length of $10 \times a_0$. Here, $a_0 = 0.142$ nm is distance between two adjacent carbon atoms in the nanoribbon. A typical remote charge impurity random potential landscape is shown in figure 2. This potential distribution is changed for each simulation run.

This random potential provides the landscape in which the transport is computed by the above prescriptions. Because the conductance fluctuations are random, they will change with each implementation of the impurity potential. Hence, we use several samples, each of which has the same impurity density of 3×10^{12} cm^{-2} but a different distribution pattern for the impurities. From these impurities, the screened potential is determined and this potential is then mapped onto the atomic lattice to produce the on-site potentials, one example of which

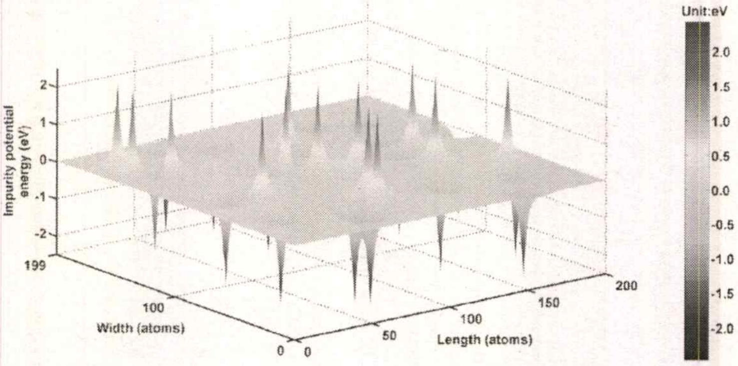

Figure 2. The potential resulting from one implementation of the remote impurity distribution. Here, the positively charged impurities are the larger quantity and the Fermi level would sit about 65 meV above the Dirac point in the absence of any gate bias.

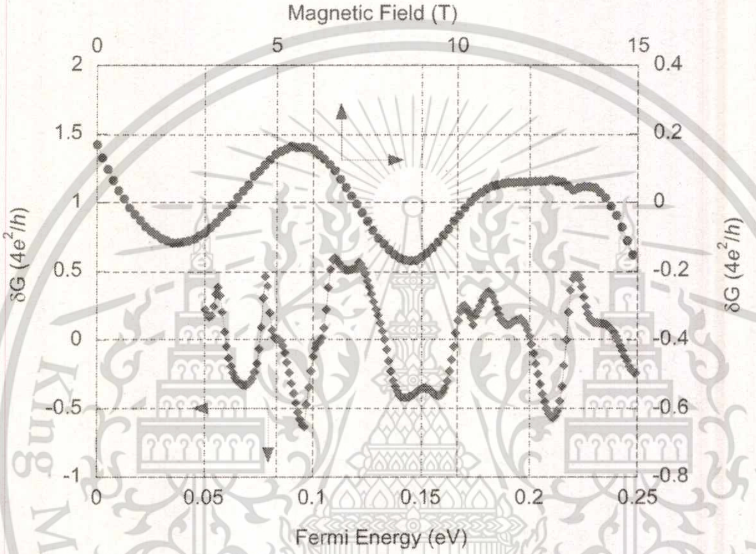

Figure 3. Typical fluctuations in the conductance observed for a magnetic field sweep (upper curve and right scale) and for a Fermi energy sweep (lower curve and left scale).

is shown in figure 2. As mentioned, the normal lattice has a width of 199 atoms and a length of 200 atomic columns, but we have considered other sizes. The position of the Fermi level, relative to the Dirac point, will depend upon the fraction of the impurities that are donors (or acceptors). Transport through this nanoribbon is computed with a stabilized variant of the scattering matrix formalism subject to magnetic field strengths applied perpendicular to the plane of the graphene sheet. The details of the computational technique have been given earlier [16, 17]. The transmission computed with this approach is then used in the multi-channel Landauer formula.

3. Results

When the conductance is computed for various values of the Fermi energy or an applied magnetic field, it is observed to have fluctuating values due to the disorder. In figure 3, we plot typical traces for the fluctuations that are observed in both a Fermi energy sweep and a magnetic field sweep (here, a background conductance has been removed to better illustrate the fluctuations themselves). Although the two curves appear to have similar amplitudes, please note that the scale on the left, for the Fermi energy sweep, is 2.5 × larger, so that the fluctuation amplitude for this latter sweep is correspondingly some 2.5 × larger than that of the magnetic field sweep. In addition, the magnetic field sweep displays a rather slow variation with magnetic field; indeed, this variation is much slower than that observed in GaAs [15]. It is not exactly clear what leads to this slow variation in magnetic field, but it may be connected with the peculiar band structure and density of states in graphene, where the cyclotron energy scales as the square root of the magnetic field rather than linear in magnetic field as in GaAs [23]. However, we showed in [15] that the correlation magnetic field in GaAs was about one flux quantum through the sample. For these samples, that corresponds to a magnetic field of 3.8 T, and could explain the slow variation in magnetic field. In the main panel of figure 4, we plot the RMS amplitude (δG_{rms}) of the CF induced by the Fermi energy sweeps, undertaken in the presence of various static magnetic fields oriented normal to the graphene plane. In the inset to this figure, we also plot the CF as a function of the Fermi energy for two different values of the magnetic field. It can clearly be seen that the amplitude of the fluctuation is significantly smaller with

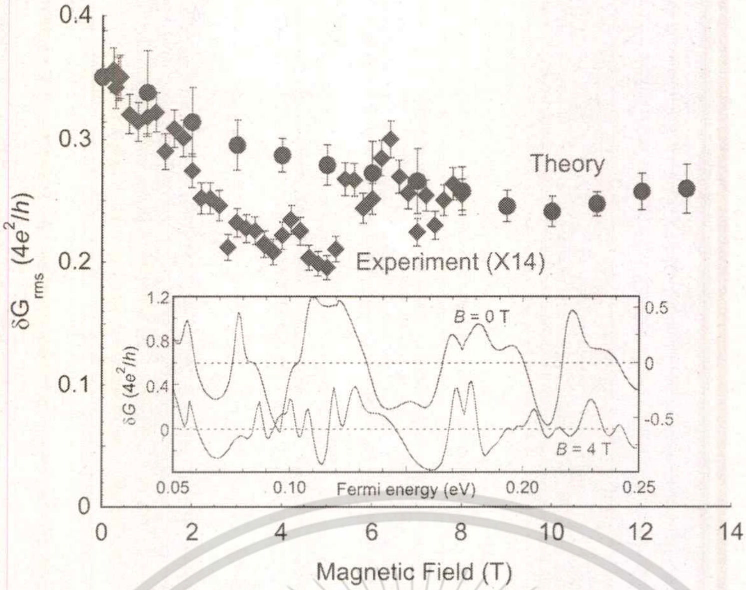

Figure 4. Amplitude of the conductance fluctuations obtained with a sweep of Fermi energy (or gate voltage in experiment) for our calculations (blue circles) and from the experiments of [9] (red diamonds). The latter has been multiplied by a factor of 14 to account for averaging over phase coherent regions in the experiment. The inset shows actual fluctuations versus Fermi energy for two different magnetic fields.

the presence of the magnetic field. Also plotted in the same figure are the experimental data from [9], which have been multiplied by a factor of 14. In the experiments, studies of the correlation function of the fluctuations observed in magnetic field sweeps were used to estimate the phase coherence length l_φ, which was found to be about 200 nm [9]. This distance is much smaller than the size of the sample over which the measurements were made, and smaller than the estimated thermal diffusion length. Hence, it is expected that the fluctuations observed experimentally should be considerably smaller than the theory due to statistical averaging of many phase coherent regions. The averaging length L in the measurements is about 2 μm. For the conditions discussed here, the reduction in amplitude is expected to be about [24]$\sqrt{6}\,(l_\varphi/L)^{3/2}$, which suggests that the experimental values should be smaller than the zero-temperature calculation by a factor of 12.9. Here, we focus upon a qualitative comparison with the experiment. Hence, we have arbitrarily used a factor of 14 in figure 4 to match the experimental and theoretical data at zero magnetic field, as this gives agreement for the values of theory and experiment at this point.

Referring to the field-induced reduction in the magnitude of the computed fluctuations in figure 4, we may conclude that this is not due to any symmetry breaking process (such as that due to the breaking of time reversal symmetry or the lifting of spin or valley degeneracy), since such mechanisms are not included in our calculations. Indeed, spin degeneracy should be lifted also when the magnetic field is applied in the plane of the graphene, but no such evidence of such symmetry breaking was found in the study of [9]. So, there must be another explanation for the magnetic-field induced reduction in the amplitude of the conductance fluctuations. We speculate that it may be related to where Büttiker has shown that, under certain conditions, and in a large perpendicular magnetic field, the latter can lead to a suppression of both elastic and inelastic back scattering [25]. As edge states begin to form in the magnetic field, most of the perceived resistance is found at the current contacts, and the forward and backward edge states are unequally occupied. Reflection from impurities cannot induce back scattering of the topologically-protected edge states, and the magnetic field also leads to a reduction in the number of channels that actually propagate through the sample. The result of these two effects should be to suppress the amplitude of the fluctuations in the conductance, and we speculate that it is this behavior that is seen in figure 4. However, we caution that the edge states are nowhere near fully formed in these samples. The fact that the experimental data falls more rapidly than our calculations suggest that the reduction of back scattering may well be more effective in the presence of additional scattering mechanisms, and when there are several phase coherent regions that lead to the averaging seen in the experimental data.

In figure 5, we plot the amplitude of the conductance fluctuations observed in experimental and simulated magnetic field sweeps as a function of the electron density. The calculations are actually done as a function of the Fermi energy, while the experiments are performed by varying the back gate voltage. We have converted both variations to one in terms of carrier density, so as to have a common parameter for comparison. Again, the experimental data has been multiplied by a factor of 14 to account for the multiple phase coherent area averaging [24]. A similar reduction in the amplitude of the fluctuations with density has been seen for both gate voltage sweeps and magnetic field sweeps [7]. It may be seen from this figure that the amplitude of the fluctuations is smaller than that in figure 4 for the Fermi energy sweeps. The difference is of the order of a factor of 3, which has also been seen in simulations for conductance fluctuations in GaAs [15]. This is

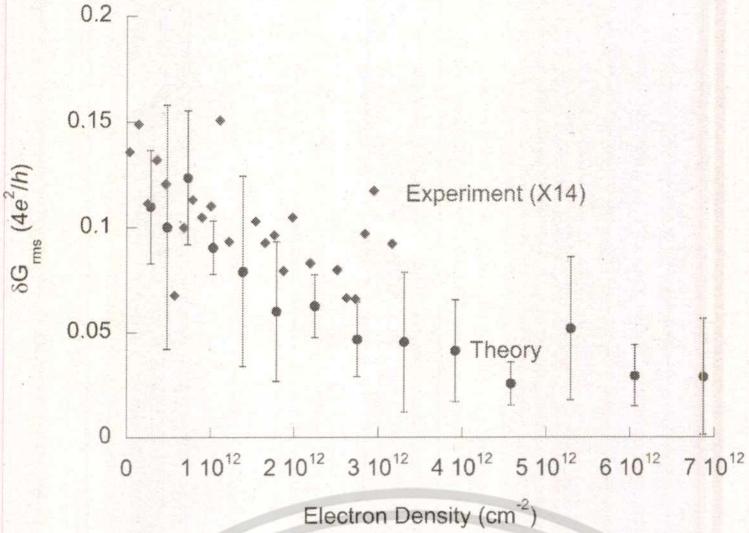

Figure 5. The average value of the conductance fluctuations that arise in a magnetic field sweep as a function of the density. The experimental data (red diamonds) has been multiplied by a factor of 14 (discussed in the text).

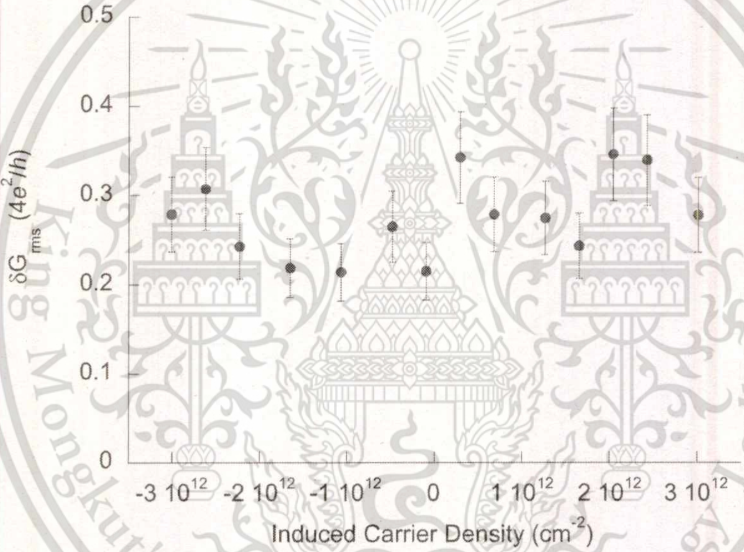

Figure 6. The conductance fluctuations observed for a fixed Fermi energy sweep on the electron side as a function of the net charge induced solely by the impurities themselves.

a clear indication that the CF do not possess any ergodic properties, as such a property would lead to equal amplitude fluctuations for different perturbations, such as sweeps in energy versus sweeps in magnetic field, or for different samples. Such a difference has also been seen in studies of 1/*f* noise in mesoscopic structures, where it is thought that this noise arises from similar interference effects as the conductance fluctuations [26]. In addition, it may be observed that the amplitude of the computed fluctuations decreases somewhat as the carrier density is raised, behavior that is captured in experiment also. This might be explained in the experiments by a decreasing phase breaking time at higher densities [27, 28], which would lead to a reduction of the phase coherence length. But, this cannot be the case in the theory, as the phase coherence length is assumed to be set by the simulation size. The observation, in both experiment and theory, of the density-dependent variations in the fluctuation amplitude points, once again, to the non-ergodic character of these fluctuations.

We have also investigated the role played by the net charge of the impurity distribution. In figure 6, we plot the conductance-fluctuation amplitude as a function of the net impurity charge, or the induced carrier density in the graphene sheet as a result of the impurity charge. That is, when the impurities are all negatively charged, a hole concentration of 3×10^{12} cm^{-2} is induced in the graphene and the Fermi energy will sit below the Dirac point in energy. With only positive impurity charge, the reverse is observed. However, the Fermi energy sweeps in figure 5 are always on the electron side over the range 50 to 250 meV, or for an actual electron density that varies from roughly 2.9×10^{11} to 7.2×10^{12} cm^{-2}. In the experiment, of course, the required gate voltage varies, and the actual carrier density depends upon the voltage at which the Dirac point is located [9]. The background charge indicated in figure 5 is the charge that shifts the Fermi energy (in the absence of gate voltage) away from the Dirac point. The difference that arises as the net impurity charge is varied is that the total charge in the system (carriers plus impurities) will vary. While the variation is too large to draw much of a conclusion, there does seem to be a slightly higher fluctuation when the induced charge is electrons. However, in the experiment, one must face the presence of the puddle state in which both electrons and holes are present with the Fermi energy near the Dirac point [29–31]. These puddles can form self-consistently and are of the order of 5–7 nm in extent [31, 32]. In the simulations done here, there is no puddle state, as the simulation does not include the many-body effects which would lead to the formation of these puddles. So, in the presence of the puddles, it would not be clear what the role of the exact net impurity density would be, nor would it be clear what the role of the additional random potential on the conductance fluctuations would be. However, it should be pointed out that an increase of the amplitude of the fluctuation near the Dirac point is observed in some cases [7], although a reduction in the amplitude of the fluctuations near the Dirac point also has been reported [33, 34] as has a reduction in the 1/*f* noise [26]. We do not see this in the simulations, and such a increase/reduction may be a natural result of the vagaries of the puddle state and its stability.

4. Discussion

Here, we have shown that the presence of a long-range potential, arising from the charged impurities lying between graphene and its substrate, may induce fluctuations due to quantum interference in the graphene conductance. We find that this long-range potential allows the carriers to respond to the presence of a magnetic field normal to the graphene sheet, something that was not observed in the case of a very short range atomic potential [17]. Indeed, for a short-range atomic potential, we find that there is no variation in the fluctuation amplitude in the presence of a magnetic field [17], which is quite similar to the experimental case of having the magnetic field in the plane of the graphene [9]. But, with the magnetic field oriented normal to the graphene, we find that the amplitude of the conductance fluctuations varies with magnetic field and density in a qualitatively similar manner as that observed in experiments of [9], confirming the idea that the quantum interference in graphene does not exhibit the ergodic character typically assumed to describe quantum interference. One question is whether this magnetic field dependence is observed in other semiconductors, such as GaAs. We have examined this question, and find that the answer is yes (which will be discussed further elsewhere).

Overall, this study confirms the idea that the theoretical framework developed several decades ago, in which mesoscopic transport in disordered material is described as ergodic is not applicable. Indeed, an alternative analytical theory of CF in monolayer graphene, developed by Kharitonov and Efetov [35] demonstrates that the fluctuations can have different universal values for different disorder type. We have shown in both normal materials, such as GaAs [14, 15], as well as in graphene [17], that the amplitude of the CF depends quite sensitively upon the amplitude of the random potential. This means that the fluctuations do not possess a universal property, especially as they are known to be suppressed in very high quality material. In addition, the response to sweeping the Fermi energy directly in the system, and to varying it via the magnetic field, produce dramatically different amplitudes of the fluctuations, which means that these fluctuations are not ergodic either. Similar behavior is seen in other interference situations, such as measurements of the 1/*f* noise in graphene [26]. While it may still be true that the actual physical basis for the fluctuations is a variation in the quantum interference of carrier waves in the random potential, the resulting CF are quite sensitive to the actual nature of this potential, both its amplitude and its range. Hence, one may expect that the improvement in the quality of the material under study will naturally lead to reduced amplitudes of these fluctuations. In fact, these results are all consistent with an understanding based on Anderson's much older description of disordered materials [18].

We do know that in very high quality material, no CF are observed, so apparently this material does not possess a sufficient degree of disorder. Secondly, we have shown previously that as the disorder is increased, states are gradually localized. We would expect the potential landscape to show more variations as the disorder increases, and this should then lead to larger amplitudes of CF, just as observed in our previous studies. Indeed, along with the onset of fluctuations, we observe the localization of the low-lying transverse modes in the device [15]. When the fluctuations are fully developed, at the higher values of the disorder potential, their amplitude is essentially just that expected by the turning on or off of a single transverse mode in the sample. Thus, we expect that this will lead to a maximum rms value of the conductance fluctuation as

$$\delta G_{\mathrm{rms}} = \frac{\eta_{\mathrm{valley}}\eta_{\mathrm{spin}}}{2\sqrt{2}}\frac{e^2}{h},$$

where the η are the degeneracy factors. This value actually agrees well with the earlier perturbation theory estimates [10], but is based more on empirical observations than on analytical methods. It should be remarked that the peak rms amplitude seen in graphene can be less than this, with this peak value of $0.35(4e^2/h)$ being seen only at zero magnetic field in figure 4.

Third, there is no concept of ergodicity that should be applied to CF. As the Fermi energy is varied, the number of transverse modes and the density also vary. But, the variation of the density with Fermi energy is quite different in e.g. GaAs and graphene. Similarly, the magnetic field also will cause the Fermi energy to change the number of transverse modes even when the density is constant. Yet, the energy scale for this, as given e.g. by the cyclotron energy, differs between e.g. GaAs and graphene, as discussed above. Hence, there is no reason to believe that there should be the same behavior for these different variations. Fourth, there is no *a priori* reason to expect that the degree of disorder will be the same for different samples (assuming that they do not come from the same slice of material) from different materials. Hence, there should be no expectation that the CF will have the same amplitude in these different samples.

Finally, as the CF depend upon the nature of the disorder potential, there may well be a density dependence, as seen in figure 5 above. Whether this arises from variations in the screening of the random potential, or from another effect, this further highlights the fact that there should be no expectation of ergodic behavior in the CF. The predictions of Anderson universality is that each and every sample is unique and one should not extend conclusions about the CF seen in a particular sample to other samples and materials.

References

[1] Ferry D K, Goodnick S M and Bird J P 2009 *Transport in Nanostructures* 2nd edn (Cambridge: Cambridge University Press) section 7.4
[2] Berger C *et al* 2006 *Science* **312** 1191
[3] Graf D, Molitor F, Ihn T and Ensslin K 2007 *Phys. Rev.* B **75** 245429
[4] Morozov S V, Novoselov K S, Katsnelson M I, Schedin F, Elias D C, Jaszczak J A and Geim A K 2008 *Phys. Rev. Lett.* **100** 016602
[5] Heersche H B, Jarillo-Herrero P, Oostinga J B, Vandersypen L M K and Morpurgo A F 2007 *Nature* **446** 56
[6] Lundeberg M B and Folk J A 2009 *Nat. Phys.* **5** 894
[7] Ojeda-Aristizabal C, Monteverde M, Weil R, Ferrier M, Guéron S and Bouchiat H 2010 *Phys. Rev. Lett.* **104** 186802
[8] Bohra G, Somphonsane R, Aoki N, Ochiai Y, Ferry D K and Bird J P 2012 *Appl. Phys. Lett.* **101** 093110 and references therein
[9] Bohra G, Somphonsane R, Aoki N, Ochiai Y, Akis R, Ferry D K and Bird J P 2012 *Phys. Rev.* B **86** 161405(R)
[10] Lee P A, Stone A D and Fukuyama H 1987 *Phys. Rev.* B **35** 1039
[11] Rycerz A, Tworzydlo J and Beenakker C W J 2007 *Europhys. Lett.* **79** 57003
[12] Kechedzhi K, Horsell D W, Tikhonenko F V, Savchenko A K, Gorbachev R V, Lerner I V and Fal'ko V I 2009 *Phys. Rev. Lett.* **102** 066801
[13] Rossi E, Bardarson J H, Fuhrer M S and Das Sarma S 2012 *Phys. Rev. Lett.* **109** 096801
[14] Grincwajg A, Edwards G and Ferry D K 1996 *Physica* B **218** 92
[15] Liu B, Akis R and Ferry D K 2013 *J. Phys.: Condens. Matter* **25** 395802
[16] Liu B, Akis R and Ferry D K 2014 *J. Comput. Electron.* **13** 950
[17] Liu B, Akis R and Ferry D K 2015 *J. Vac. Sci. Technol.* B **33** 04E101
[18] Anderson P W 1958 *Phys. Rev.* **109** 1492
[19] Hong X, Zou K and Zhu J 2009 *Phys. Rev.* B **80** 241415
[20] Bolotin K, Sikes K, Jiang Z, Fudenberg G, Hone J, Kim P and Stormer H 2008 *Solid State Commun.* **146** 351
[21] Das Sarma S, Adam S, Hwang E H and Rossi E 2011 *Rev. Mod. Phys.* **83** 407
[22] Davies J H 1998 *The Physics of Low-Dimensional Semiconductors: An Introduction* (Cambridge: Cambridge University Press)
[23] Castro Neto A H, Guinea F, Peres N M R, Novoselov K S and Geim A K 2009 *Rev. Mod. Phys.* **81** 109
[24] Beenakker C W J and van Houten H 1991 *Solid State Physics* ed H Ehrenreich and D Turnbull vol 44 (San Diego, CA: Academic) p 1
[25] Büttiker M 1988 *Phys. Rev.* B **38** 9375
[26] Rahman A, Guikema J W and Markovic N 2014 *Nano Lett.* **14** 6621
[27] González J, Guinea F and Vozmediano M A H 1996 *Phys. Rev. Lett.* **77** 3589
[28] Hwang E H, Hu B Y-K and Das Sarma S 2007 *Phys. Rev. Lett.* **99** 226801
[29] Martin J, Akerman N, Ulbricht G, Lohmann T, Smet J H, von Klitzing K and Yacoby A 2008 *Nat. Phys.* **4** 144
[30] Deshpande A, Bao W, Miao F, Lau C N and LeRoy B J 2009 *Phys. Rev.* B **79** 205411
[31] Rossi E and Das Sarma S 2011 *Phys. Rev. Lett.* **107** 155502
[32] Gilbertini M, Tomadin A, Guinea F, Katsnelson M I and Polini M 2012 *Phys. Rev.* B **85** 201405
[33] Chen Y-F, Bae M-H, Chialvo C, Dirks T, Bezryadin A and Mason N 2010 *J. Phys.: Condens. Matter* **22** 205301
[34] Berezovsky J, Borunda M F, Heller E J and Westervelt R M 2010 *Nanotechnology* **21** 274013
[35] Kharitonov M V and Efetov K B 2008 *Phys. Rev.* B **78** 033404

NANO LETTERS

Letter

pubs.acs.org/NanoLett

"Freeing" Graphene from Its Substrate: Observing Intrinsic Velocity Saturation with Rapid Electrical Pulsing

H. Ramamoorthy,[†] R. Somphonsane,[‡] J. Radice,[†] G. He,[†] C.-P. Kwan,[§] and J. P. Bird*,[†,||]

[†]Department of Electrical Engineering, University at Buffalo, the State University of New York, Buffalo, New York 14260-1900, United States

[‡]Department of Physics, King Mongkut's Institute of Technology Ladkrabang, Bangkok 10520, Thailand

[§]Department of Physics, University at Buffalo, the State University of New York, Buffalo, New York 14260-1500, United States

[||]Graduate School of Advanced Integration Science, Chiba University, 1-33 Yayoi-cho, Inage-ku, Chiba 263-8522, Japan

Supporting Information

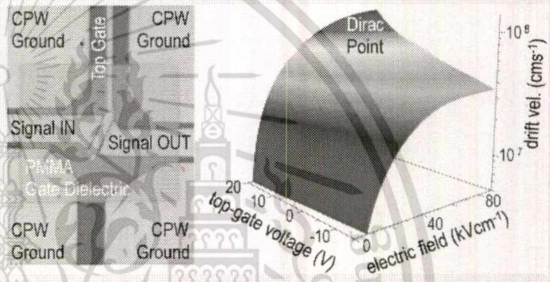

ABSTRACT: Rapid (nanosecond-scale) electrical pulsing is used to study drift-velocity saturation in graphene field-effect devices. In these experiments, high-field pulses are utilized to drive graphene's carriers on time scales much faster than that on which energy loss to the underlying substrate can occur, thereby allowing the observation of the highest saturation velocities reported to date. In a dramatic departure from the behavior exhibited by conventional metals and semiconductors, as the electron or hole density is reduced toward the charge-neutrality point, the drift velocity is found to reach values comparable to the Fermi velocity itself. Corresponding current densities are as large as 10^9 A/cm^2, similar to the values reported for carbon nanotubes and for graphene-on-diamond transistors. In essence, our approach of rapid pulsing allows us to "free" graphene from the deleterious influence of its substrate, revealing a pathway to achieve the superior electrical performance promised by this material. The usefulness of this approach is not merely limited to graphene but should extend also to a broad variety of two-dimensional semiconductors.

KEYWORDS: *Velocity saturation, hot carriers, graphene, transient transport, thermal effects in nanodevices*

Realizing the full potential of graphene[1] as a novel material for nanoelectronics[2,3] requires strategies to maximize its current-carrying capacity, while minimizing Joule losses to its surrounding environment. At the microscopic scale, this problem reduces to one of managing drift-velocity saturation (DVS), which arises when carriers, strongly accelerated by the electric field, rapidly lose their excess energy by spontaneously emitting optical phonons. By limiting the ultimate velocity to which carriers can be accelerated, DVS constrains the maximal currents that can be carried by any material, and must therefore be mitigated in many device scenarios. Although the large optical phonon energies (>150 meV) intrinsic to graphene promise high saturation velocities[4−7] (v_{sat}), experiments typically yield much lower values that are degraded by unintended heating of the underlying substrate.[8−16] This problem was apparent from the earliest investigations of the high-field characteristics of graphene, which revealed the velocity saturation to be consistent with a process in which the drifting carriers lose energy by exciting lower-energy (~55 meV) surface optical phonons (SOPs) in the SiO$_2$ substrate.[17] This result may be understood quantitatively in terms of the (approximate) relation for the saturation velocity[10]

$$v_{\mathrm{sat}} = \frac{2}{\pi}\frac{\omega_{\mathrm{OP}}}{\sqrt{\pi n}} \qquad (1)$$

where n is the two-dimensional (2D) carrier density. This relation shows that the value of v_{sat} is directly proportional to the energy ($\hbar\omega_{\mathrm{OP}}$) of the specific optical phonon responsible for hot-carrier energy loss. Because the energy of the SiO$_2$ SOPs is much lower than that of graphene's intrinsic optical modes, energy transfer to the substrate can dominate the velocity saturation, resulting in the surprisingly low values reported for v_{sat}.[8−16] In quantitative terms, using a density $n = 10^{12}$ cm^{-2} as a reference value, eq 1 predicts a saturated velocity $v_{\mathrm{sat}} \sim 10^8$ cms^{-1} for intrinsic graphene, while typical experiments performed with SiO$_2$ substrates yield values around a factor of four or five times smaller than this.

Recognizing the negative influence of the substrate on the high-field characteristics of graphene devices, one approach to overcome its effects are to eliminate it completely, making use of devices in which the graphene channel is freely suspended.[18−20] Measurements[21] of such devices do indeed exhibit higher saturation velocities than those reported for graphene-on-SiO$_2$ transistors, yet still do not reach the values expected for intrinsic graphene. Alternatively, exfoliation of

Received: October 1, 2015
Revised: December 7, 2015
Published: December 9, 2015

DOI: 10.1021/acs.nanolett.5b04003
Nano Lett. 2016, 16, 399−403

graphene onto BN substrates has been explored as a means to suppress substrate-related scattering and has been demonstrated to significantly improve low-field mobility.[22−24] While studies of DVS have been limited in this system, they have nonetheless been found[14] to exhibit low values for v_{sat}, consistent with a phonon pathway with an energy of just ∼40 meV.

Having identified how energy loss from graphene's hot carriers strongly suppresses its saturated velocity, a question that arises concerns whether suitable schemes can be implemented to alleviate this problem? The answer to this question is suggested by recent studies of transient transport in graphene, which show that heating of the substrate does not develop instantaneously, but rather takes place over many tens of nanoseconds.[12,25,26] This result can be attributed to the large thermal mismatch between channel and substrate and indicates that pulsed investigations of graphene, performed on nanosecond time scales, should allow its intrinsic nonequilibrium characteristics to be revealed.[11] While there have previously been several different reports of transient transport in graphene,[11,25−28] none of them have explored the behavior in this regime of rapid pulsing. In this Letter, we overcome this problem by using rapid (nanosecond) pulses, allowing us to probe the true hot-carrier dynamics of graphene before its performance is degraded through its coupling to the substrate. In this way, we are able to achieve saturation velocities consistent with those expected for intrinsic material, and higher than those reported for suspended graphene[21] and for devices realized on boron-nitride substrates.[14] In a dramatic departure from the behavior exhibited by conventional metals and semiconductors in which the drift-induced shift of the Fermi surface is typically small, as the Dirac point is approached from either the conduction or valence bands we find that v_{sat} reaches values comparable to the Fermi velocity (∼10^8 cm s^{-1}) itself. Corresponding current densities (∼10^9 A/cm^2) are similar to those found in carbon nanotubes[29] and in graphene-on-diamond transistors.[30] In essence, our approach of rapid pulsing allows us to "free" graphene from the influence of its substrate and to therefore reveal a pathway to achieve the superior electrical performance promised by this material. Beyond graphene, we expect that this approach should also be amenable to investigations of DVS in many other two-dimensional materials.

Rapid pulsing of graphene was performed at room temperature in an impedance-matched setup (Supporting Information) in which electrical contact to graphene flakes, exfoliated on SiO_2, was provided by on-chip coplanar waveguides (CPWs, see Figure 1a). The carrier density was varied by an aligned top-gate (TG), isolated from the graphene by 120 nm of hardened PMMA (insets to Figure 1a,b). Pulses of various amplitude (v_p^{in}) and duration were applied to the input CPW, and the resulting current was measured by connecting the output waveguide to the 50-Ω input of a sampling oscilloscope. For sufficiently small pulse amplitudes, the transient resistance (R) determined at different gate voltages (V_{TG}) agreed well with that obtained by small-signal lockin measurement (Figure 1b). Five devices (D1−D5) were investigated here with D2−D5 being monolayer while D1 was realized from bilayer graphene (see the Supporting Information for the dimensions of the devices and their room-temperature mobility.)

The transient electrical characteristics of graphene can be strongly influenced by extrinsic factors, most notably by charge injection into the dielectric layers of the device and by thermal conduction to its substrate.[25−28,31] Under such conditions, it is easy to reach misleading conclusions regarding the physical

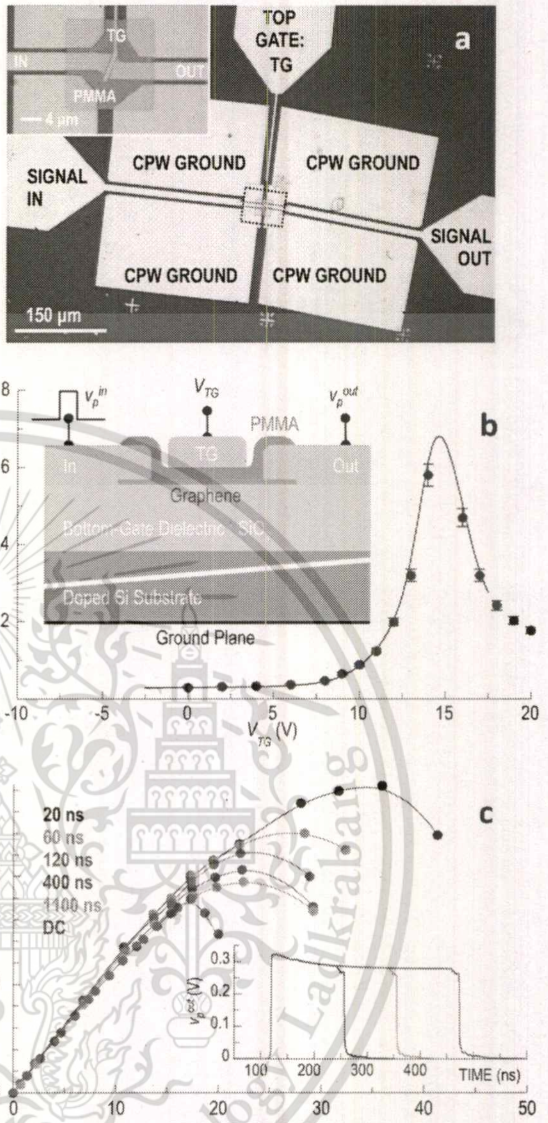

Figure 1. (a) The main panel is an optical micrograph of one of the graphene transistors (Device D5) studied here, showing the CPW structure used to make contact to the graphene flake. The area enclosed by the dotted line is shown in expanded form in the inset, in which the hardened PMMA layer has been colorized to highlight the top-gate geometry. (b) Comparison of the Dirac curve measured for Device D1 at room temperature by small-signal lockin detection (solid line) and low-amplitude transient pulsing (v_p^{in} = 100 mV, corresponding to a field strength F ∼ 0.6 $kVcm^{-1}$; duration = 4 ns; filled symbols). The inset is a cross-sectional schematic indicating the essential components of the top-gated devices. (c) The main panel shows the current−voltage characteristic determined at V_{TG} = 0 and room temperature for Device D1 for pulses of varying duration (indicated) and for DC biasing. The inset plots three long pulses of varying duration (v_p^{in} = 3.05 V, corresponding to F ∼ 34 $kVcm^{-1}$) for Device D4, exhibiting the influence of charge trapping and substrate heating.

origins of current saturation, as demonstrated by the results of Figure 1c. Here we plot current−voltage characteristics of one of our devices for transient pulses of varying duration and amplitude. (Throughout this Letter, quoted current values, and the drift velocities inferred from them, correspond to those determined at the end of the current pulse just before its falling edge.) At fields (F) below ~15 kV/cm, the transient current is independent of pulse duration and is also consistent with that obtained by DC biasing. At higher fields, however, the current decreases systematically with increasing pulse length and tends toward the DC result. Present in each data set is an apparent region of negative-differential conductance (NDC), whose onset shifts to higher field for shorter pulses. This behavior does not represent an intrinsic NDC, however, but rather results from the extrinsic influence of trapping and heating.[26] This may be seen by referring to the inset of Figure 1c, where we show measurements of pulses up to several hundred nanoseconds long. A monotonic decay of v_p^{out} is seen on this time scale, which has previously been identified as arising from the combined influence of charge trapping and substrate heating.[25−28,31] It is this decay that is responsible for the observed NDC and in order to avoid its influence it is necessary to pulse graphene on time scales much faster than those considered in Figure 1c.

An example of our rapid pulsing of graphene is presented in Figure 2a, the contour of which represents the output transients (v_p^{out}) measured in response to the application of short (4 ns) pulses of varying amplitude (v_p^{in}). The contour nicely reproduces the form of the input pulses, as shown in the insets to Figure 2a where we directly compare the input and output signals. The faithful manner in which the input transient is reproduced at the output demonstrates that parasitic circuit elements exert little influence on these measurements, and that trapping and substrate heating are both suppressed. In Figure 2b−d, we plot the current-(drain) voltage characteristics inferred from experiments of this type. Figure 2b plots gate voltages on the hole side of the Dirac curve (whose charge-neutrality point is at V_{TG} ~ 16.5 V), while Figure 2d shows similar data for electrons. Clear current saturation is observed for both carrier types with no evidence of NDC, despite the fact that the peak field strength in the measurements is almost twice that in Figure 1c.

From data such as those of Figure 2, and a knowledge of the carrier density (Supporting Information), the field-velocity characteristics of graphene are determined. Representative results are plotted in Figure 3a,b, where we see clear saturation of the drift velocity (v_d) for field strengths exceeding ~30 kV/cm. Consistent with the form of eq 1, v_{sat} increases as the carrier density is reduced from either the hole or electron sides. In the vicinity of the Dirac point, however, the drift velocity does not saturate (Figure 3a, inset), but rather shows a "kink-like" feature. The kink is also apparent in the current−voltage characteristics (see the data for V_{TG} = 10 and 15 V in Figure 2b and for V_{TG} = 20 V in Figure 2d) and has previously been attributed to the role of minority-carrier injection from the drain.[8,13,32]

The results obtained from our rapid-pulsing studies exhibit a number of important differences with those reported in prior (DC or quasi-DC) investigations. First, the current densities that we achieve (~4 mA/μm, see Figure 2b) are much larger than reported previously. Second, we note that velocity saturation has previously been parametrized[10,11,16,33] by appealing to Thornber's equation[34]

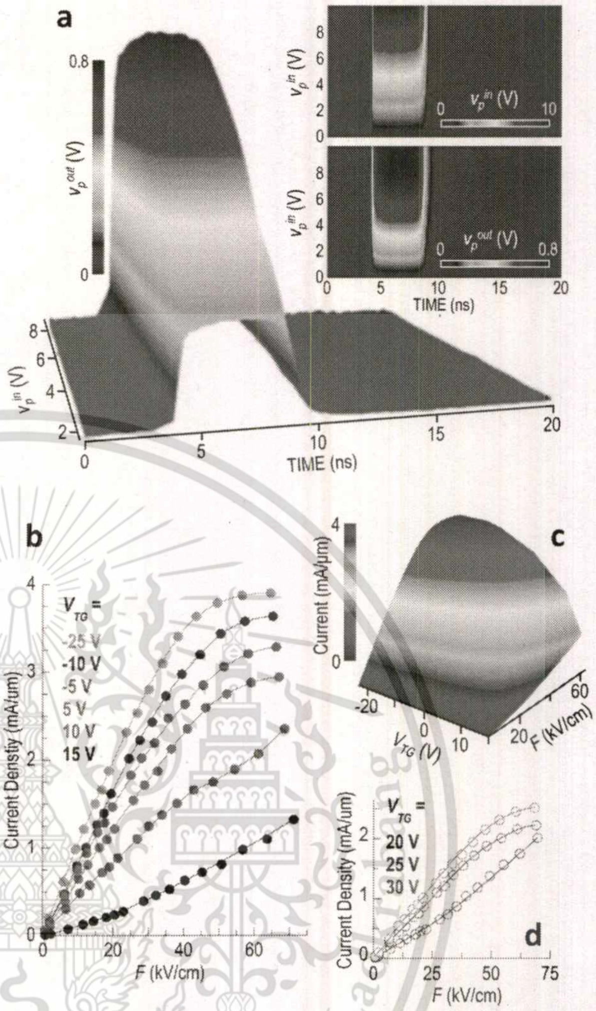

Figure 2. (a) Output pulses of duration 4 ns, measured in Device D2 in response to the application of input pulses of varying amplitude. The top-gate voltage is fixed at V_{TG} = −10 V. The inset plots the form of the input and output pulses as two-dimensional color contours to allow a comparison of their forms. (b) Transient current−voltage characteristics determined using 4 ns pulses such as those in panel a. Data are for holes in Device D3 and the different top-gate voltages are indicated. (c) Data in panel b replotted as a color contour. (d) Transient current−voltage characteristics determined using 4 ns pulses such as those in panel a. Data are for electrons in Device D3 at the indicated top-gate voltages. Solid lines in panels b and d are interpolation curves.

$$v_d = \left[\left(\frac{1}{\mu F}\right)^{\beta} + \left(\frac{1}{v_{sat}}\right)^{\beta}\right] \tag{2}$$

where μ is the low-field mobility, F is the electric field responsible for drift, and β is a phenomenological parameter. In work based on DC (and quasi-DC) methods, the field dependence of v_d has been found to be well fitted[10,11] with $\beta \approx 2$. As we show in Figure 3c, however, our data are also well described by eq 2 but only by taking $\beta = 5$. This larger value translates into a more rapid initial increase of current with electric field and to the onset of saturation at larger v_d (see Figure 3c). Overall, the implication of these observations is that

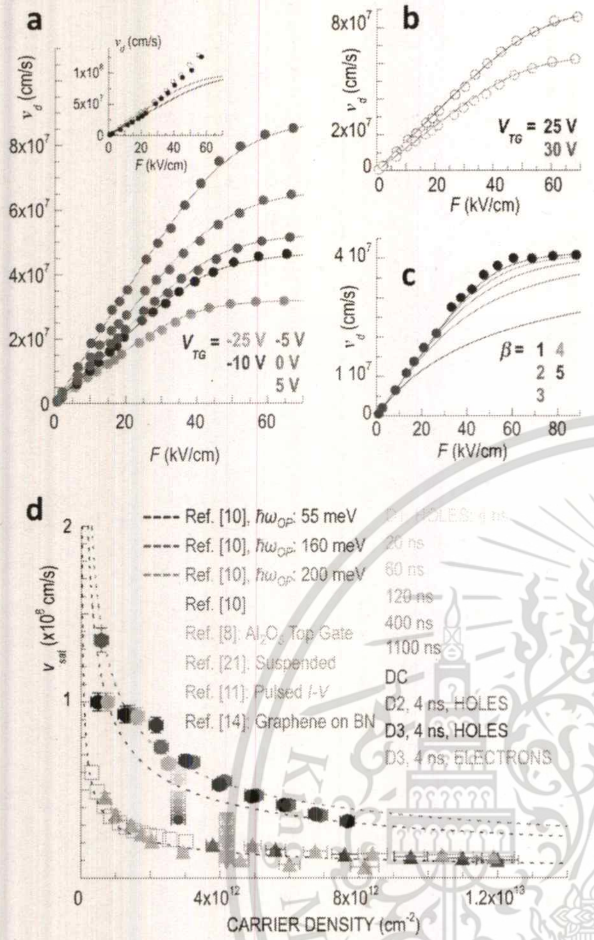

Figure 3. (a) Transient velocity-field characteristic determined for holes in Device D3 by 4 ns pulsing. Solid lines through the data are fits to eq 2 using the experimentally observed v_{sat} and a fit parameter $\beta = 5$. The inset plots corresponding data for the same device near its charge-neutrality point, where the current−voltage characteristics show the "kink" behavior arising from minority-carrier injection from the drain. Solid lines are fits to eq 2, obtained by assuming $\beta = 5$ and varying v_{sat} to obtain a best fit to the lower-field data. Filled symbols: $V_{TG} = 15$ V. Open symbols: $V_{TG} = 20$ V. (b) Similar plot as in panel a except for electrons in Device D3. (c) Fit of the velocity-field characteristic to eq 2, using the same values of v_{sat} but different β values. Filled symbols were obtained for Device D2 for $V_{TG} = -10$ V. (d) Variation of saturated drift velocity with carrier density. The different symbols are identified in the inset to the plot. Dashed lines correspond to the predictions of eq 1, using different characteristic phonon energies (also indicated in the inset).

relative to DC investigations our strategy of rapid pulsing allows us to more effectively drive graphene's carriers by avoiding the onset of trapping and heating.

The most important result of our study is presented in Figure 3d, which shows the density-dependent variation of v_{sat} determined in three of our devices. Data obtained by rapid pulsing for both electrons and holes clearly follow the variation expected from eq 1, for graphene's intrinsic optical-phonons ($\hbar\omega_{OP}$ = 160−200 meV). As the density is reduced below 10^{12} cm^{-2}, v_{sat} approaches the Fermi velocity of graphene ($v_F \sim 10^8$ cm/s), providing a dramatic difference with the behavior exhibited by typical metals. (To determine v_{sat} in this low-density limit, we restrict our fitting in terms of eq 2 to the field regime below the kink, see the inset to Figure 3a). These results should be contrasted with the data obtained from prior studies[8,10,11,14,15] (data plotted as filled triangles), performed under DC, or quasi-DC, conditions and which clearly follow the variation expected for scattering from the lower-energy ($\hbar\omega_{OP}$ = 55 mV) SOPs of SiO$_2$. In fact, our values for v_{sat} even exceed those obtained for freely suspended graphene[21] (inverted triangles) and for graphene isolated on a BN substrate[14] (open squares). On the basis of these observations we conclude that rapid pulsing of graphene can indeed be used to probe its intrinsic DVS, free of the negative impact of current-induced Joule heating of the substrate.

Some further points should be made regarding the importance of using very short pulses to obtain the intrinsic saturation velocities demonstrated in Figure 3d. In the inset to Figure 1c, the decaying portions of the different transient curves overlap very closely with one another, which leads one to consider whether it should be possible to infer the intrinsic velocity saturation from these curves also, simply by using the maximum value of the current just after the rising edge? While this would be reasonable if our measurements were performed in a "single-shot" scheme, it must be noted that our transient curves are instead captured by repetitive sampling. Consequently the entire duration of the transient pulse, including that obtained at short times, may reflect processes occurring on much longer time scales. These include substrate heating and charge trapping, the latter of which is known[26] to yield long recovery times. This point is discussed in more detail in the Supporting Information, where we provide an example to demonstrate the significantly increased saturation velocities that can be achieved by using short-pulse studies. As a further, more technical, point we note that such pulsing allows us to apply much higher fields to the devices (compare the maximum field strength in Figure 1c to that in Figures 2b−d and 3a−c) without irreversibly degrading their performance or even destroying them as the local substrate temperature is driven well-beyond ambient.

As a final comment on the results of Figure 3d, we point to the data plotted as the solid blue circles in this figure. These data show how the inferred drift velocity is steadily degraded as the measurement pulse is made longer; on increasing the duration from 4 to 20 ns, the drift velocity already drops by some 10%, while for a pulse length of around a microsecond the decrease is as much as 50% (these data are plotted more clearly in the Supporting Information). This figure again emphasizes the need to probe transport on very short (nanosecond) time scales when studying graphene's intrinsic characteristics. A useful avenue to pursue in the future, to study the dynamics of thermal decoupling from the substrate in more detail, would be to fix the pulse duration at its shortest value and to steadily increase the pulse-repetition frequency up to a value (125 MHz) approaching the pulse length. Unfortunately, this was not possible with our experimental setup in which the maximum repetition frequency of the pulse generator was 1 MHz. Up to this frequency, at least we found the short-pulse characteristics to be independent of the repetition rate, as we describe in further detail in the Supporting Information. Despite being unable to extend our measurements to higher repetition frequencies, for the first time we emphasize that the main value of this work lies in its demonstration of the use of short well-separated pulses to reveal the intrinsic velocity saturation of graphene.

While previous theoretical work[6,35,36] has explored the influence of different substrates on high-field DC-transport in graphene, our work demonstrates how rapid pulsing may be used to effectively eliminate any such influence. In this way, we achieve significantly higher saturated velocities than those reported previously, despite the poorer low-field mobility of our devices (Supporting Information) when compared to suspended material[21] or to graphene on BN.[14] The lessons learned from our study are not only relevant to graphene but rather point to a broader strategy in which rapid pulsing may be used to manage heat dissipation in different 2D semiconductors.

■ ASSOCIATED CONTENT

Ⓢ Supporting Information

The Supporting Information is available free of charge on the ACS Publications website at DOI: 10.1021/acs.nanolett.5b04003.

> The high-frequency measurement setup used to perform the pulsed studies; basic low-field characterization of device mobility; calculations of the drift velocity accounting for quantum capacitance, residual charge, and thermal carriers; and a discussion of the influence of pulse duration on the velocity-saturation characteristics. (PDF)

■ AUTHOR INFORMATION

Corresponding Author

*E-mail: jbird@buffalo.edu. Phone: +1 (716) 645-1015.

Author Contributions

All authors contributed equally to this work.

Notes

The authors declare no competing financial interest.

■ ACKNOWLEDGMENTS

This research was supported by the U.S. Department of Energy, Office of Basic Energy Sciences, Division of Materials Sciences and Engineering under Award DE-FG02-04ER46180. R.S. acknowledges support from the Thailand Research Fund (contract no. TRG5880012).

■ REFERENCES

(1) Geim, A. K.; Novoselov, K. S. *Nat. Mater.* 2007, *6*, 183–191.
(2) Schwierz, F. *Nat. Nanotechnol.* 2010, *5*, 487–496.
(3) Novoselov, K. S.; Fal'ko, V. I.; Colombo, L.; Gellert, P. R.; Schwab, M. G.; Kim, K. A. *Nature* 2012, *490*, 192–200.
(4) Chauhan, J.; Guo, J. *Appl. Phys. Lett.* 2009, *95*, 023120.
(5) Shishir, R. S.; Ferry, D. K. *J. Phys.: Condens. Matter* 2009, *21*, 344201.
(6) Perebeinos, V.; Avouris, P. *Phys. Rev. B: Condens. Matter Mater. Phys.* 2010, *81*, 195442.
(7) Fang, T.; Konar, A.; Xing, H.; Jena, D. *Phys. Rev. B: Condens. Matter Mater. Phys.* 2011, *84*, 125450.
(8) Meric, I.; Han, M. Y.; Young, A. F.; Ozyilmaz, B.; Kim, P.; Shepard, K. L. *Nat. Nanotechnol.* 2008, *3*, 654–659.
(9) Barreiro, A.; Lazzeri, M.; Moser, J.; Mauri, F.; Bachtold, A. *Phys. Rev. Lett.* 2009, *103*, 076601.
(10) Dorgan, V. E.; Bae, M.-H.; Pop, E. *Appl. Phys. Lett.* 2010, *97*, 082112.
(11) Meric, I.; Dean, C. R.; Young, A. F.; Baklitskaya, N.; Tremblay, N. J.; Nuckolls, C.; Kim, P.; Shepard, K. L. *Nano Lett.* 2011, *11*, 1093–1097.
(12) Islam, S.; Li, Z.; Dorgan, V. E.; Bae, M.-H.; Pop, E. *IEEE Electron Device Lett.* 2013, *34*, 166–168.
(13) Han, M. Y.; Kim, P. *Nano Convergence.* 2014, *1*, 1–11.
(14) Meric, I.; Dean, C.; Young, A.; Hone, J.; Kim, P.; Shepard, K. *Proc. IEEE Int. Electron Devices Meeting* 2010, 23.2.1–23.2.4.
(15) Bae, M. H.; Ong, Z.-Y.; Estrada, D.; Pop, E. *Nano Lett.* 2010, *10*, 4787–4793.
(16) Bae, M. H.; Islam, S.; Dorgan, V. E.; Pop, E. *ACS Nano* 2011, *5*, 7936–7944.
(17) DaSilva, A. M.; Zou, K.; Jain, J. K.; Zhu, J. *Phys. Rev. Lett.* 2010, *104*, 236601.
(18) Bolotin, K. I.; Sikes, K. J.; Hone, J.; Stormer, H. L.; Kim, P. *Phys. Rev. Lett.* 2008, *101*, 096802.
(19) Du, X.; Skachko, I.; Barker, A.; Andrei, E. Y. *Nat. Nanotechnol.* 2008, *3*, 491–495.
(20) Castro, E. V.; Ochoa, H.; Katsnelson, M. I.; Gorbachev, R. V.; Elias, D. C.; Novoselov, K. S.; Geim, A. K.; Guinea, F. *Phys. Rev. Lett.* 2010, *105*, 266601.
(21) Dorgan, V. E.; Behnam, A.; Conley, H. J.; Bolotin, K. I.; Pop, E. *Nano Lett.* 2013, *13*, 4581–4585.
(22) Dean, C. R.; Young, A. F.; Meric, I.; Lee, C.; Wang, L.; Sorgenfrei, S.; Watanabe, K.; Taniguchi, T.; Kim, P.; Shepard, K. L.; Hone, J. *Nat. Nanotechnol.* 2010, *5*, 722–726.
(23) Xue, J.; Sanchez-Yamagishi, J.; Bulmash, D.; Jacquod, P.; Deshpande, A.; Watanabe, K.; Taniguchi, T.; Jarillo-Herrero, P.; LeRoy, B. J. *Nat. Mater.* 2011, *10*, 282–285.
(24) Levendorf, M. P.; Kim, C.-J.; Brown, L.; Huang, P. Y.; Havener, R. W.; Muller, D. A.; Park, J. *Nature* 2012, *488*, 627–632.
(25) Lee, Y. G.; Kang, C. G.; Jung, U. J.; Kim, J. J.; Hwang, H. J.; Chung, H. J.; Seo, S.; Choi, R.; Lee, B. H. *Appl. Phys. Lett.* 2011, *98*, 183508.
(26) Majumdar, K.; Kallatt, S.; Bhat, N. *Appl. Phys. Lett.* 2012, *101*, 123505.
(27) Carrion, E. A.; Serov, A. Y.; Islam, S.; Behnam, A.; Malik, A.; Xiong, F.; Bianchi, M.; Sordan, R.; Pop, E. *IEEE Trans. Electron Devices* 2014, *61*, 1583.
(28) Li, H.; Russ, C. C.; Liu, W.; Johnsson, D.; Gossner, H.; Banerjee, K. *IEEE Trans. Electron Devices* 2014, *61*, 1920–1928.
(29) Huang, J. H.; Chen, S.; Jo, S. H.; Wang, Z.; Han, D. X.; Chen, G.; Dresselhaus, M. S.; Ren, Z. F. *Phys. Rev. Lett.* 2005, *94*, 236802.
(30) Yu, J.; Liu, G.; Sumant, A. V.; Goyal, V.; Balandin, A. A. *Nano Lett.* 2012, *12*, 1603–1608.
(31) Lee, K.; Moon, J.-S.; Oh, T.; Kim, S.; Asbeck, P. *Solid-State Electron.* 2014, *101*, 44–49.
(32) Bai, J.; Liao, L.; Zhou, H.; Cheng, R.; Liu, L.; Huang, Y.; Duan, X. *Nano Lett.* 2011, *11*, 2555–2559.
(33) Winters, M.; Hassan, J.; Zirath, H.; Janzen, E.; Rorsman, N. *J. Appl. Phys.* 2013, *113*, 193708.
(34) Thornber, K. K. *J. Appl. Phys.* 1980, *51*, 2127–2136.
(35) Li, X.; Barry, E. A.; Zavada, J. M.; Buongiorno Nardelli, M.; Kim, K. W. *Appl. Phys. Lett.* 2010, *97*, 232105.
(36) Rengel, R.; Pascual, E.; Martin, M. J. *Appl. Phys. Lett.* 2014, *104*, 233107.

APPLIED PHYSICS LETTERS 107, 262103 (2015)

Plasmon-mediated energy relaxation in graphene

D. K. Ferry,[1] R. Somphonsane,[2] H. Ramamoorthy,[3] and J. P. Bird[3]
[1]School of Electrical, Computer, and Energy Engineering, Arizona State University, Tempe, Arizona 85287-5706, USA
[2]Department of Physics, King Mongkut's Institute of Technology, Ladkrabang, Bangkok 10520, Thailand
[3]Department of Electrical Engineering, University at Buffalo, the State University of New York, Buffalo, New York 14260-1500, USA

(Received 12 October 2015; accepted 14 December 2015; published online 28 December 2015)

Energy relaxation of hot carriers in graphene is studied at low temperatures, where the loss rate may differ significantly from that predicted for electron-phonon interactions. We show here that plasmons, important in the relaxation of energetic carriers in bulk semiconductors, can also provide a pathway for energy relaxation in transport experiments in graphene. We obtain a total loss rate to plasmons that results in energy relaxation times whose dependence on temperature and density closely matches that found experimentally. *© 2015 AIP Publishing LLC.*
[http://dx.doi.org/10.1063/1.4938760]

The study of "hot" carriers, driven out of equilibrium by an electric field, has long been pursued, since the relaxation properties of these carriers are important for semiconductor-device performance.[1] With the emergence of graphene as a promising electronic material,[2–4] there has been significant experimental[5–18] and theoretical[19–24] interest in the dynamics of its hot carriers. One aspect of graphene is the high energy of its optical phonons, which should render these modes ineffective at mediating cooling below room temperature.[25] Similarly, momentum-conservation constraints dictate that cooling via acoustic phonons is quasi-elastic, and therefore also inefficient. Consequently, the role of other scattering processes has drawn increasing attention, with particular interest having focused on the implications of impurity-assisted "supercollisions."[23]

Commonly in studies of hot-carrier cooling, one compares the variations of some transport feature (e.g., mesoscopic fluctuations, localization-related magneto-resistance, and other quantum corrections), as a function of lattice temperature (T_L) and electric field, to infer hot-carrier temperature (T_e). We study the dependence of this parameter on electric field and T_L yields information on the scattering processes responsible for cooling, with this assignment achieved by introducing the hot-carrier energy-loss rate (P_e). Defined as the power dissipated per electron, this rate usually varies as[26]

$$P_e(T_e, T_L) = A(T_e^p - T_L^p), \tag{1}$$

with A and p characteristic parameters reflective of the specific relaxation process. Acoustic-phonon scattering in pristine graphene, for example, is predicted to yield $p = 4$,[19,20] while $p = 3$ is expected for supercollisions.[23] While both power laws have been reported in separate experiments,[10,14–17] other work has demonstrated an exponent of $p = 3$ in a regime where supercollisions are clearly not expected to be effective.[13,18] This suggests that some other mechanism may be responsible for cooling, and in this letter, we suggest that this may be provided by plasmon-mediated[27,28] scattering.

The relaxation of carrier energy through plasmon-induced losses has been studied for transport in metals[29,30] and semiconductors[31–37] (the single-particle carrier-carrier scattering, of course, does not relax either the net energy or the net momentum). Plasmons themselves have also been studied in carbon nanotubes[38] and graphene,[39] where the dielectric function has been calculated.[40] The plasmons of interest here arise from the free carriers in graphene, and their influence on cooling is determined by starting from the standard expression for the energy-loss rate[1,25,41]

$$P_e \equiv \left\langle \frac{dE}{dt} \right\rangle = \sum_{k,q,\omega} \{ f(E_k)[1 - f(E_k - \hbar\omega)]\,\hbar\omega W_{k\to k-q} - f(E_k)[1 - f(E_k + \hbar\omega)]\,\hbar\omega W_{k\to k+q} \}, \tag{2}$$

where the symbols E and k represent the carrier energy and momentum, respectively, while $\hbar\omega$ and $\hbar q$ are the energy and momentum exchanged in each collision, here that of the plasmon modes, and f(E) is the carrier distribution function. The scattering element W describes the plasmon-mediated interaction, the form of which we take from treatments of the low-temperature dephasing time (although with some differences). In (2), the energy-relaxation process depends on the *difference* in emission and absorption terms, whereas the phase-breaking time depends upon the *sum* of these terms. Each of these two terms is expressed as

$$W_{\pm} = \frac{2\pi}{\hbar} N \mathrm{Im}\left\{ \frac{V(q)}{\varepsilon(q,\omega)} \right\} \delta\left(\omega - \frac{E_k - E_{k\pm q}}{\hbar} \right), \tag{3}$$

where N is either the Bose Einstein distribution, in the absorption term, or 1 plus this distribution, in the emission term. The scattering function arises from the imaginary part of the screened Coulomb potential $V(q) = e/2\varepsilon_s q$, where e is the electron charge and ε_s is the permittivity of graphene.[28,42] Here, the screening is done by the full frequency and momentum dependent dielectric function. As may be expected, the dielectric function is dominated by the plasmon pole, but in using the inverse of the dielectric function in (3), we incorporate the collision broadening of this resonance. This is given as $\mathrm{Im}(V/\varepsilon) = \omega e^2/\varepsilon_s \chi_2 q^2 \tau$, where $\chi_2 = n_s e^2/2m^* \varepsilon_s = n_s e^2 v_F/2\hbar k_F \varepsilon_s$, n_s is the sheet density of carriers, v_F is the Fermi velocity, k_F is the Fermi momentum, and τ is the scattering time. In two dimensions, the plasmon frequency involves the momentum as $\omega_p^2 = n_s e^2 q/2m^* \varepsilon_s$, where n_s is the sheet density and m^* is the electron or hole effective mass $(= \hbar k/v_F)$. The broadening arises from the total scattering rates, which yield a scattering time τ. A key step in the development of the energy loss rate lies in the fact that (3) may be used to rewrite (2) as

$$P_e = 2\pi \sum_{\mathbf{q}} \int \frac{\omega}{2\pi} d\omega \mathrm{Im}\left\{\frac{V(q)}{\varepsilon(q,\omega)}\right\} \delta_\omega \Phi(\hbar\omega), \qquad (4)$$

where δ_ω represents the energy-conserving delta function and the various distribution functions (both Fermi-Dirac and Bose-Einstein) are pulled into the expression

$$\Phi(x) = \sum_{\mathbf{k}} \{[N(x,T)+1]f(E)[1-f(E-x)] \\ -N(x,T)f(E)[1-f(E+x)]\}, \qquad (5)$$

where x will ultimately involve the plasma frequency and the electron distribution function is at the carrier temperature T_e. Carrying out the various integrations (see supplementary material[43]) yields the energy-loss rate

$$P_e \equiv \left\langle \frac{dE}{dt} \right\rangle = \frac{2.4 k_B^3}{2\pi\hbar^2 v_F^2 \tau}\left(T_e^3 - T_L^3\right), \qquad (6)$$

where v_F is the Fermi velocity. Comparison with the form of (1) indicates two important features of this expression. First, the plasmon mechanism yields an exponent of $p = 3$, similar to that obtained for supercollisions. Second, the prefactor (A) in the energy-loss rate of (6) is governed by a system-dependent scattering time τ, which describes the broadening, that can be determined from the density and temperature dependent mobility of the device under test. In most cases at low temperature, this is dominated by the impurity scattering.[25]

An important parameter related to the energy-loss rate is the energy-relaxation time (τ_e), which may be obtained from (6) by factoring the cubic terms in T to give a definition of τ_e from the theoretical parameters[40]

$$P_e = \frac{k_B(T_e - T_L)}{\tau_e}. \qquad (7)$$

In Fig. 1, we compare the variation of $\tau_e(T_e)$, obtained in the experiment of Ref. 13, with that predicted by (6) for the base temperature of 1.8 K, as used in the experiments. Theoretical values of τ_e are determined by taking the experimentally-determined energy-loss rate for the given density and T_e and introducing this into (6) and (7) to compute τ_e. From this figure, we see that the plasmon-based model reproduces not only the low-temperature magnitude of τ_e, for both electrons and holes, but that it also captures its quantitative dependence on temperature.

The most striking observation of Ref. 13 was of a strong variation of τ_e as a function of carrier density. This behavior is reproduced in Fig. 2, along with the results of our calculations. The main panel compares the behavior observed at a number of different electron temperatures, and again shows close, if not perfect, agreement between experiment and theory. In the inset to the figure, we plot the variation of τ_e as a function of electron density, for three different measurement currents. As with the data in the main panel, the theory reproduces the experiment well.

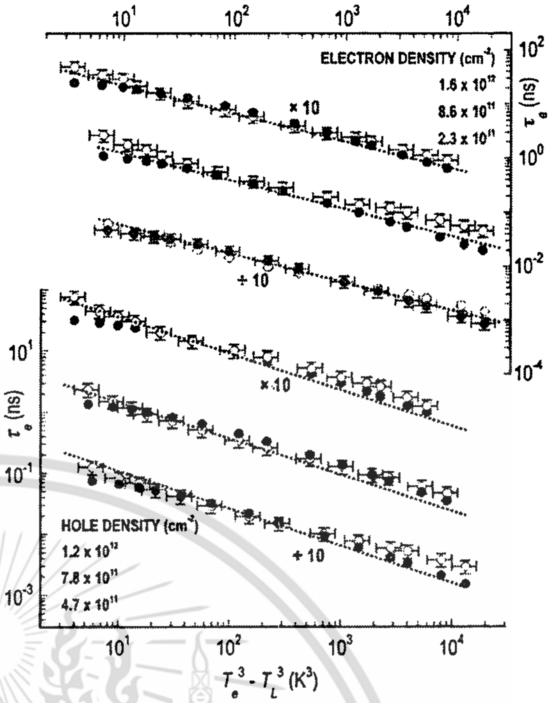

FIG. 1. The energy relaxation time for several values of the electron and hole density. Experimental values from Ref. 13 are plotted as open symbols while theoretical values obtained from (6) and (7) are the closed symbols. Error bars are shown for the experimental data only. Dotted lines through the theoretical data are guides to the eye that indicate a linear variation of power input with T^3. In each case, the red and green curves have been offset by a factor of 10 for clarity as indicated.

The plasmon-loss mechanism rearranges the energy distribution function, but this energy remains in the electron gas as a whole. Under the excitation current (or electric field), the distribution function is shifted in momentum space to reflect the current, and it spreads as the electron temperature rises. The shift can also distort the distribution to produce an elongated extension in the direction of the field or current. The ultimate limit of this elongation is a delta function in the field direction.[1] Between the shift in momentum space, and the elongation, the distribution function has more carriers in the forward direction than the backward direction. The plasmon loss takes carriers from the streaming forward direction and moves them to the backward direction, in the symmetric terms of the distribution function, on the average. This scattering process relaxes the streaming distribution, but the ultimate result still remains that another process must pass the energy to the lattice. This can be due to acoustic-phonon scattering,[19–24] or even supercollisions.[23] However, it is the plasmon interaction that dominates what is seen experimentally, as it is this process which moves the current carrying particles out of the forward extension of the distribution

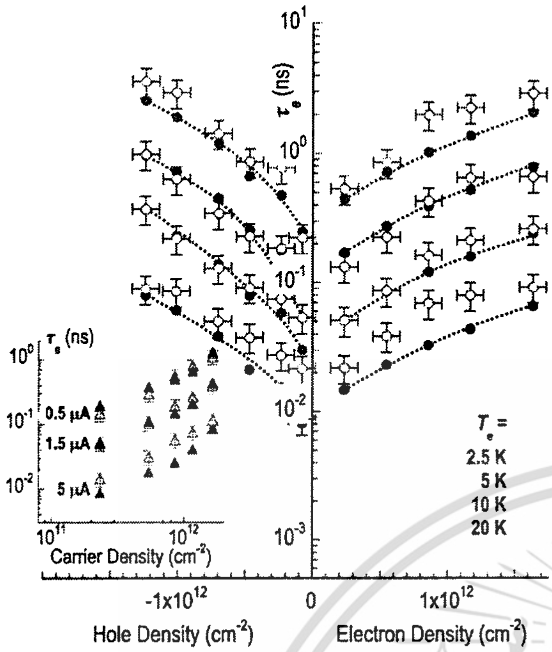

FIG. 2. The energy relaxation time as a function of the carrier density with the electron temperature as a parameter. Experimental values from Ref. 13 are plotted as open symbols while theoretical values obtained from (6) and (7) are the closed symbols. Dotted lines provide a guide though the theoretical data (filled symbols). At the lower left, we plot the variation of the relaxation time with density for a few values of the excitation current at $T_L = 4.2\,\mathrm{K}$.

function. The other processes which ultimately move the energy to the lattice are thus masked, and this would be even more true with the supercollision process as it has the same temperature dependence (i.e., $p = 3$) as that found here.

In conclusion, a good quantitative agreement between the experimental data of Ref. 13 and the theoretical results obtained here suggest that the plasmon interaction dominates hot-carrier energy relaxation in graphene at low temperatures. Since the role of this mechanism in governing energy loss does not appear to have been appreciated thus far, it suggests that its relevance may be far wider than simply the experimental study analyzed here.

Experimental work at Buffalo was supported by the Department of Energy (DE-FG02-04ER46180). R.S. acknowledges the support from the Thailand Research Fund (TRG5880012).

[1] See, e.g., E. M. Conwell, *High Field Transport in Semiconductors* (Academic Press, New York, 1967).
[2] I. Meric, M. Y. Han, A. F. Young, B. Ozylimaz, P. Kim, and K. L. Shepard, Nat. Nanotechnol. **3**, 654 (2008).
[3] M. Freitag, M. Steiner, Y. Martin, V. Perebeinos, Z. Chen, J. C. Tsang, and P. Avouris, Nano Lett. **9**, 1883 (2009).
[4] A. Barreiro, M. Lazzeri, J. Moser, F. Mauri, and A. Bachtold, Phys. Rev. Lett. **103**, 076601 (2009).
[5] P. Plochocka, P. Kossacki, A. Golnik, T. Kazimierczuk, C. Berger, W. A. de Heer, and M. Potemski, Phys. Rev. B **80**, 245415 (2009).
[6] J. Voutilainen, A. Fay, P. Häkkinen, J. K. Viljas, T. T. Heikkilä, and P. J. Hakonen, Phys. Rev. B **84**, 045419 (2011).
[7] Z. Tan, L. Ma, G. T. Liu, L. Lu, and C. L. Yang, Phys. Rev. B **84**, 115429 (2011).
[8] D. Sun, C. Divin, C. Berger, W. A. de Heer, P. N. First, and T. B. Norris, Phys. Status Solidi C **8**, 1194 (2011).
[9] K. Majumdar, S. Kallatt, and N. Bhat, Appl. Phys. Lett. **101**, 123505 (2012).
[10] A. M. R. Baker, J. A. Alexander-Webber, Y. Altebaeumer, and R. J. Nicholas, Phys. Rev. B **85**, 115403 (2012).
[11] A. S. Price, S. M. Hornett, A. V. Shytov, E. Hendry, and D. W. Horsell, Phys. Rev. B **85**, 161411(R) (2012).
[12] A. C. Betz, F. Vialla, D. Brunel, C. Voisin, M. Picher, A. Cavanna, A. Madouri, G. Fève, J.-M. Berroir, B. Plaçais, and E. Pallechi, Phys. Rev. Lett. **109**, 056805 (2012).
[13] R. Somphonsane, H. Ramamoorthy, G. Bohra, D. K. Ferry, Y. Ochiai, N. Aoki, and J. P. Bird, Nano Lett. **13**, 4305 (2013).
[14] A. M. R. Baker, J. A. Alexander-Weber, T. Altebaeumer, S. D. McMullan, T. J. B. M. Janssen, A. Tzalenchuk, S. Lara-Avila, S. Kubatkin, R. Yakimova, C.-T. Lin, L.-J. Li, and R. J. Nicholas, Phys. Rev. B **87**, 045414 (2013).
[15] M. W. Graham, S.-F. Shi, D. C. Ralph, J. Park, and P. L. McEuen, Nat. Phys. **9**, 103 (2013).
[16] M. W. Graham, S. Shi, Z. Wang, D. C. Ralph, J. Park, and P. L. McEuen, Nano Lett. **13**, 5947 (2013).
[17] A. C. Betz, S. H. Jhang, E. Pallecchi, R. Ferreira, G. Fève, J.-M. Berroir, and B. Plaçais, Nat. Phys. **9**, 109 (2013).
[18] J. V. Borzenets, U. C. Coskun, H. T. Mebrahtu, Yu. V. Bomze, A. L. Smirnov, and G. Finkelstein, Phys. Rev. Lett. **111**, 027001 (2013).
[19] R. Bistritzer and A. H. MacDonald, Phys. Rev. Lett. **102**, 206410 (2009).
[20] S. Kubakaddi, Phys. Rev. B **79**, 075417 (2009).
[21] W. K. Tse and S. Das Sarma, Phys. Rev. B **79**, 235406 (2009).
[22] J. K. Viljas and T. T. Heikkilä, Phys. Rev. B **81**, 245404 (2010).
[23] J. C. W. Song, M. Y. Reizer, and L. S. Levitov, Phys. Rev. Lett. **109**, 106602 (2012).
[24] P. Virtanen, Phys. Rev. B **89**, 245409 (2014).
[25] See, e.g., M. V. Fischetti, J. Kim, S. Narayanan, Z.-Y. Ong, C. Sachs, D. K. Ferry, and S. J. Aboud, J. Phys. Condens. Matter **25**, 473202 (2013), and references therein.
[26] See e.g., Sec. 6.4 of V. F. Gantmakher and Y. B. Levinson,*Carrier Scattering in Metals and Semiconductors* (North-Holland, Amsterdam, 1987).
[27] C. Kittel, *Quantum Theory of Solids* (Wiley, New York, 1963).
[28] See, e.g., D. K. Ferry, S. M. Goodnick, and J. P. Bird, *Transport in Nanostructures*, 2nd ed. (Cambridge University Press, Cambridge, 2009) and references therein.
[29] F. A. Ferrell, Phys. Rev. **101**, 554 (1956).
[30] Y. L. Klimontovich, Sov. Phys. JETP **36**, 999 (1959).
[31] B. B. Varga, Phys. Rev. **137**, A1896 (1965).
[32] A. Mooradian and G. B. Wright, Phys. Rev. Lett. **16**, 999 (1966).
[33] M. E. Kim, A. Das, and S. Senturia, Phys. Rev. B **18**, 6890 (1978).
[34] A. I. Kasiyan and P. I. Russo, Sov. Phys. Semicond. **15**, 1142 (1982).
[35] S. E. Kumekov and V. I. Perel, Sov. Phys. Semicond. **16**, 1291 (1982).
[36] P. Lugli and D. K. Ferry, IEEE Electron Dev. Lett. **6**, 25 (1985).
[37] P. Lugli and D. K. Ferry, Appl. Phys. Lett. **46**, 594 (1985).
[38] M. F. Lin and K. W. K. Shung, Phys. Rev. B **50**, 17744 (1994).
[39] B. Wunsch, T. Stauber, F. Sols, and F. Guinea, New J. Phys. **8**, 318 (2006).
[40] E. H. Hwang and S. Das Sarma, Phys. Rev. B **75**, 205418 (2007).
[41] See Sec. 10.3.1 of D. K. Ferry, *Semiconductors* (Macmillan, New York, 1991).
[42] G. F. Guiliani and J. J. Quinn, Phys. Rev. B **26**, 4421 (1982).
[43] See Supplementary material at http://dx.doi.org/10.1063/1.4938760 for the process of getting to (6) from (4).

J Comput Electron
DOI 10.1007/s10825-015-0764-3

Energy relaxation of hot carriers in graphene via plasmon interactions

D. K. Ferry[1] · R. Somphonsane[2] · H. Ramamoorthy[3] · J. P. Bird[3]

Abstract Energy relaxation of hot carriers in graphene is studied theoretically and experimentally at low temperatures, where the loss rate may differ significantly from that predicted for electron–phonon interactions. We show here that plasmons, important in the relaxation of energetic carriers in bulk semiconductors, can also provide a pathway for energy relaxation in transport experiments in graphene. Reflecting the linear nature of graphene's bands, we obtain a total loss rate to plasmons that is independent of carrier density. This results in energy relaxation times whose dependence on temperature and density closely matches that reported experimentally.

Keywords Graphene · Energy relaxation · Plasmons · Carrier heating

1 Introduction

The study of "hot" carriers in semiconductors has been pursued for many decades (See, e.g., [1]). By hot carriers, we refer to those carriers driven out of equilibrium by an applied electric field, or equivalently by passing a large current through the device. Since the relaxation of these carriers is important for electronic-device performance, it is important to understand just how this relaxation process occurs. When an electric field is applied to a semiconductor, or a current is passed through it, the distribution function is dramatically affected. While spherically symmetric in momentum space at thermal equilibrium (or cylindrically symmetric in the case of a two-dimensional semiconductor such as graphene), under non-equilibrium conditions this function splits into what can be considered as two separate parts. The first of these remains largely symmetric, while the second, the so-called "streaming", term is responsible for the current [2–4]. Electrical transport measurements typically probe *only* the streaming term, while telling us nothing about the symmetric one, behavior that should be contrasted with optical measurements. In the latter, the small photon momentum does not create the streaming term, and *only* information about the symmetric term can be obtained. Here, we want to treat plasmon-mediated energy relaxation, which is different since the interaction is between carriers in the streaming part of the distribution and those in the symmetric part. That is, the plasmon interaction transfers net energy *from* the streaming terms, thus serving to relax that part of the distribution that is measured by transport. It does this by primarily (near) back-scattering (for materials like graphene, exact back scattering is chirally forbidden). In a purely symmetrical distribution, we would not expect this process to be important, so that it is not likely to be significant in an optical experiment.

With the emergence of graphene as a promising material for future nanoelectronics [5–7], there has been significant experimental [8–21] and theoretical [22–27] interest in the processes governing its hot carrier dynamics. One aspect of graphene is the very high energy of its optical phonons, which ensures that these are ineffective at cooling electrons and holes except at higher temperatures, near or above room temperature [28]. At lower temperatures than this, the major cooling pathway has been thought to involve the

---

✉ D. K. Ferry
ferry@asu.edu

[1] School of Electrical, Computer, and Energy Engineering, Arizona State University, Tempe, AZ 85287-5706, USA

[2] Department of Physics, King Mongkut's Institute of Technology, Ladkrabang, Bangkok 10520, Thailand

[3] Department of Electrical Engineering, University at Buffalo, The State University of New York, Buffalo, NY 14260-1500, USA

interaction of hot carriers with acoustic phonons. Due to momentum-conservation constraints, however, this process is quasi-elastic, and so inefficient at mediating energy transfer. Consequently, the role of other phonon processes has drawn increasing attention, with significant interest having focused on the implications of impurity-assisted "supercollisions" [26]. Experiments utilizing noise thermometry [15, 20], coupled microwave and dc heating [29], and p-n junction photocurrent spectroscopy [18,19], have established the role of this mechanism at elevated carrier/phonon temperatures. Nonetheless, lower-temperature studies of mesoscopic devices [16,21] suggest that this mechanism does not provide a complete picture of hot-carrier cooling.

In evaluating the heating of carriers induced in a transport measurement, it is convenient to express the results in a form (See e.g., [30])

$$P_e(T_e, T_L) = A\left(T_e^p - T_L^p\right), \tag{1}$$

where P_e is the power input per carrier (the energy loss rate) and A and p are parameters determined by the specific mechanism of energy relaxation. Scattering of hot carriers by acoustic phonons in pristine graphene, for example, is predicted to be characterized by an exponent $p = 4$ [22,23], while $p = 3$ is expected for the aforementioned supercollisions [26]. The situation with regards to the latter mechanism is unclear, however, since some experiments [16,21] have also yielded $p = 3$ while clearly being performed in the regime in which supercollisions are not expected to dominate. Motivated by this, we therefore explore the possibility of cooling in graphene by a very-different process, namely that arising from plasmon-mediated scattering of hot carriers. Here, we demonstrate that such an exponent ($p = 3$), in fact, also is consistent with the role of plasmon-mediated relaxation. By deriving an expression for the energy-relaxation time (τ_e), the time scale governing the loss of energy from hot carriers in the system, we demonstrate here that this interaction can provide an important relaxation pathway in graphene. To demonstrate the validity of this approach, we show that the relaxation time predicted by this model reproduces well the temperature- and density-dependent variations of this parameter found in a recent experiment [16]. Most importantly, this agreement is achieved *without the use of any adjustable parameters*. Thus, this highlights how the weak electron–phonon coupling in graphene opens up the possibility of hot-carrier dissipation via novel mechanisms, beyond those typically considered in more conventional materials.

2 Plasmons in graphene

Scattering of carriers by the screened potential of other electrons and from the collective plasmon modes are both part of the total electron–electron (or hole–hole) interaction among the free carriers. Starting from the non-interacting electron gas, the inter-carrier Coulomb interaction is usually treated as a perturbation, but is problematic due to the long range of the Coulomb potential. The coupled dielectric function then has two important poles, one at zero frequency and one at the plasmon frequency. These correspond to the single-particle scattering potential and the plasmon mode, respectively. Generally, one introduces a screening wave vector to the Coulomb potential, which separates the long-range and the short-range parts. Then, the potential can be split into a short-range part, where the scattering wave vector is larger than this screening vector, and this corresponds to the free-particle Coulomb scattering. The long-range part, on the other hand, is responsible for the interactions with the collective plasmon mode. These collective mode are bosons, so that the scattering rate can be found in quite normal ways. The relaxation of carrier energy through plasmon-induced losses has been studied for transport in metals [31,32] and semiconductors [33–39] for some time. Plasmons themselves have also been studied in carbon nanotubes [40] and graphene [41], where the dielectric function has been calculated [42]. It has also been suggested that the plasmon interaction can be important for phase breaking in two dimensional systems [43–45].

To be sure, there has been a lively debate in the literature over whether or not the electrons can actually interact with the plasmons. It has been stated in some papers that this interaction cannot occur in graphene [46–48], since graphene is *qualitatively different from a parabolic band semiconductor*. It has been known for quite some time that the plasmons can be scattered by the single-particle interactions, a process known as Landau damping. If this scattering is large, then the plasmon modes are heavily damped and one could say that they don't really exist. However, it has been conclusively shown that the plasmon dispersion curve (energy versus wave vector) in graphene remains outside the region of single particle electron–electron interactions [42]. However, the dispersion curve does enter the region of electron–hole scattering. In spite of this, away from the Dirac point, one does not have strong electron–hole interactions as one or the other of these particles is absent. Moreover, in a recent review of many-body interactions in graphene [49], it was found that a double feature is present in the decay rate given by the imaginary part of the self-energy. One of these was a peak at positive energies, signaling an onset of plasmon emission. In another context, plasmonics is a new area of interest in graphene. Here, high frequency waves are used to excite the plasmons. In a recent paper, the authors computed the dielectric function and plasmons in graphene, and find that [50] "...scattering between plasmons and electrons is possible and will lead to damping of the plasmons." This is plasmon absorption by the electrons. Of course, one then expects that the reverse will be true and this scattering will lead to emission of plasmons by energetic electrons. So, it appears that the plasmons are well defined excitations, even in graphene, and can be involved in the relaxation of hot carriers.

The scattering potential for the plasmons $V(q)$ remains the Coulomb potential, and this is combined with the momentum- and frequency-dependent dielectric function in the dynamic screening approach [51,52]. In general, this approach arises from the Lindhard RPA dielectric function, and the dynamic screening expression can be written as

$$\varepsilon(q,\omega)=\varepsilon_s\left[1+\frac{\omega_p^2}{Dq^2/\tau-(\omega-i/\tau)^2}\right], \tag{2}$$

where the square of the plasmon frequency in two dimensions is given as

$$\omega_p^2=\frac{n_s e^2 q}{2m^*\varepsilon_s}=\chi_2 q. \tag{3}$$

In the dielectric response, one normally just keeps the plasmon-pole approximation, which means keeping only the frequency term in the denominator of (2). However, we require the imaginary part of the inverse dielectric function, which means keeping at least the leading term in the scattering time. Then, we may write the scattering term as

$$\mathrm{Im}\left\{\frac{V}{\varepsilon}\right\}\simeq\frac{\omega e^2}{\varepsilon_s\chi_2 q^2\tau}, \tag{4}$$

with $\chi_2=n_s e^2/2m^*\varepsilon_s=n_s e^2 v_F/2\hbar k_F\varepsilon_s$ (ε_s is the permittivity of the graphene), and τ is the total scattering time in the material. We will use these results in the next section for the energy relaxation rate.

3 The energy relaxation rate

As we remarked above, the role of the electric field is to distort the distribution function to account for the hot carriers. We illustrate this in Fig. 1, where we compare the equilibrium distribution function (in two dimensions) and the streaming distribution function that results in the hot carriers. The electric field causes a portion of the distribution to stream along the field direction, and this accounts for the current that flows through the sample. The electric field provides a forcing function which is balanced by the relaxation of energy back to those states that have been emptied by the formation of the streaming part of the distribution. We indicate this for plasmons by the arrow that flows from the streaming part to the back of the distribution. Of course, the inverse process, the absorption of the plasmons, is also possible, and the two processes have to balance in equilibrium. The net energy loss by the carriers depends upon the difference between the emission rate and the absorption rate. The general approach we use to describe this overall process is quite straight forward. We begin with a standard equation for the energy loss rate, which can be written as [1], (See e.g., [30]), [53]

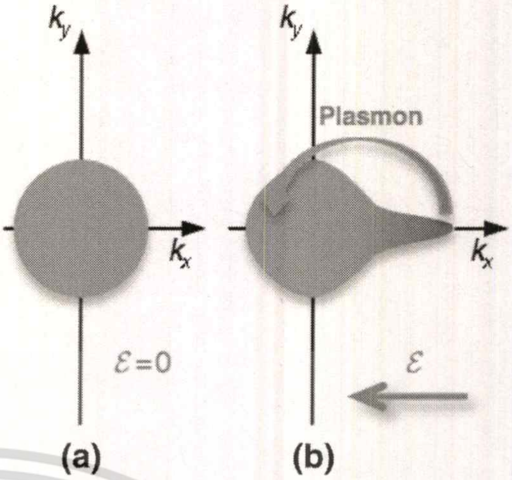

Fig. 1 **a** A diagrammatic depiction of the equilibrium distribution function in two dimensions. **b** A similar depiction of the formation of the streaming portion of the distribution, and the role of plasmons in the energy relaxation

$$\left\langle\frac{dE}{dt}\right\rangle=\sum_{k,q,\omega}\left\{f(E_k)\left[1-f(E_k-\hbar\omega_q\right]\hbar\omega_q W_{k\to k-q}\right.$$
$$\left.-f(E_k)\left[1-f(E_k+\hbar\omega_q\right]\hbar\omega_q W_{k\to k+q}\right\}. \tag{5}$$

Here, W represents the scattering function. For the scattering function we take the standard approach to the phase-breaking time in mesoscopic materials at low temperature, in which the scattering function arises from the imaginary part of the screened Coulomb potential (See, e.g., [54]), [43]. There is a difference, however. It may be noted in (5) that the energy relaxation process depends upon the *difference* in the emission and absorption terms, as described above, whereas the phase-breaking time depends upon the *sum* of these two terms. Each of these two terms is expressed as

$$W_\pm=\frac{2\pi}{\hbar}N\,\mathrm{Im}\left\{\frac{V(q)}{\varepsilon(q,\omega)}\right\}\delta\left(\omega-\frac{E_k-E_{k\pm q}}{\hbar}\right), \tag{6}$$

where the plus (minus) sign refers to the plasmon emission (absorption). The N here is either the Bose Einstein distribution, in the absorption term, or 1 plus this distribution, in the emission term. Note that we require the imaginary part of the inverse dielectric function, which is given by (4) above. In (5), there is a delta function which conserves the energy, while the momentum is also assumed to be conserved in writing this expression. There is still the phase space argument of the delta functions to be considered, and this is discussed in Appendix 1.

Using these preliminaries, and the results of (6), we can now rewrite (5) as

$$P = 2\pi \sum_{\mathbf{q}} \int \frac{\omega d\omega}{2\pi} \mathrm{Im}\left\{\frac{V(q)}{\varepsilon(q,\omega)}\right\} \delta_{\omega} \Phi(\hbar\omega) \tag{7}$$

where δ_ω represents the energy conserving delta function, and the various distribution functions (both Fermi–Dirac and Bose–Einstein) are pulled into the expression

$$\begin{aligned}\Phi(x) = \sum_{\mathbf{k}} \{ & [N(x,T)+1] f(E)[1-f(E-x)] \\ & - N(x,T) f(E)[1-f(E+x)]\end{aligned} \tag{8}$$

and the distribution function is at the carrier temperature T_e. Price [55] has shown how the integral over the distribution functions can be carried out, and how the electron temperature in the emission term finally appears in the Bose–Einstein distribution. Using the properties of the linear bands in graphene, his results applied to the last integral can be rewritten as

$$\Phi(x) = \frac{x E_F}{\pi(\hbar v_F)^2}\left[N(x,T_e) - N(x,T_L)\right] \quad . \tag{9}$$

In (7), the potential and inverse dielectric function are given by (4).

We are now ready to evaluate the integrals in (7). Using the delta functions and the other properties given above and in Appendix 1, we can carry out these integrals in a straightforward manner. This leads to two terms, as in (9), each of which can be written in terms of an arbitrary temperature as

$$F(T_1) = \frac{e^2 E_F k_B^3 T_1^3}{2\pi \varepsilon_s \hbar^4 v_F^2 \chi_2 \tau} \int_0^{u_{\max}} \frac{u^2 du}{e^u - 1} \tag{10}$$

where $u = \hbar v_F q / k_B T_1$ and $u_{\max} = 2\hbar v_F k_F / k_B T_1$ represents an approximate upper limit. In general, this upper limit is density and temperature dependent but is large, and the integral approaches a limiting value near 2.4 as is shown in Appendix 2.

Using the above results, and those of Appendix 2 for the integral, the final power loss is given as

$$\left\langle \frac{dE}{dt} \right\rangle = \frac{2.4 k_B^3 \left(T_e^3 - T_L^3\right)}{2\pi \hbar^2 v_F^2 \tau} \quad . \tag{11}$$

An interesting point is that, with the unique band structure of graphene, the explicit density dependence has dropped out of this final power loss, but will return when we normalize it to the power loss per electron. The second important point to note is that the loss rate in this expression is characterized by the exponent $p = 3$, consistent with the results of recent experiments [16,21].

In (10) and (11), we see the scattering time τ is the only sample dependent parameter remaining in the energy loss rate. In general, we can use the measured mobility to infer a value only for the momentum relaxation time, which is longer than τ by a numerical factor that arises from the averaging over the scattering angle. The momentum relaxation time is weighted in favor of large angle scattering (subject to chirality constraints), while there is considerably more small angle scattering with the Coulomb interaction. Since there are other scattering processes than just the Coulomb scattering from impurities, it is difficult to assign an exact value that arises from this weighted average. We have assumed the dominance of impurity scattering for the mobility, and this allows us to compute an estimate of the actual scattering time from the momentum relaxation time. In Appendix 3, we plot

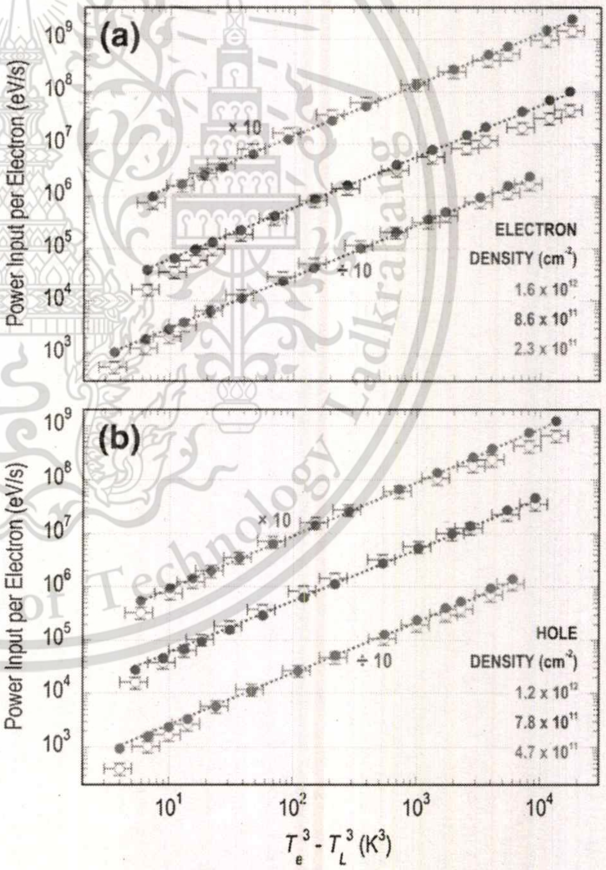

Fig. 2 The energy loss rate per carrier for **a** Electrons and **b** holes. In each case, the *solid symbols* are the theory (11) and the *open symbols* are the data from Ref. [16]. The *color* corresponds to a particular density and *error bars* are shown for the experimental data only. *Dotted lines* through the theoretical data are guides to the eye that indicate a linear variation of power input with T^3 (Color figure online)

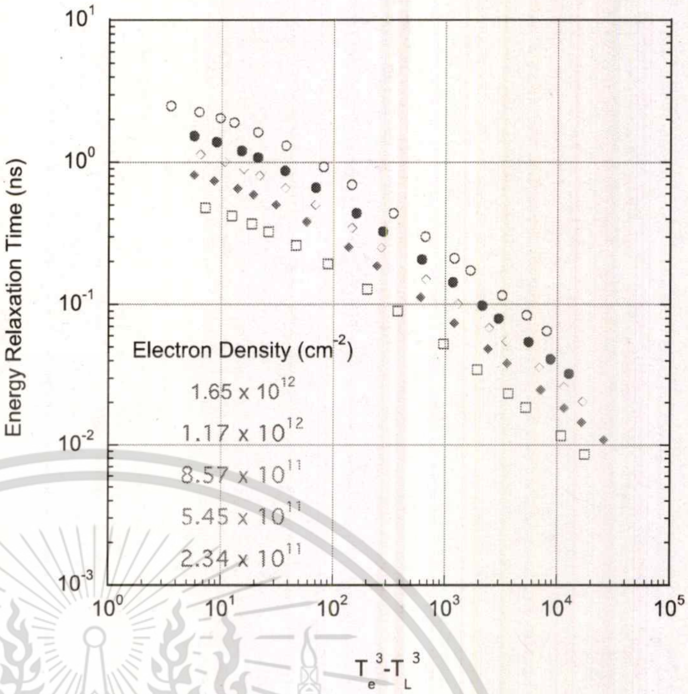

Fig. 3 Variation of the energy relaxation time with temperature for several values of the electron density

the mobility that is measured in the samples as a function of temperature for various densities.

We are now ready to show an experimental test of the theory developed here, and this is a direct comparison of the main results of the present work with those of Ref. [16]. There, we showed an energy-loss rate described by an exponent p close to 3, while the energy-relaxation time was found to decrease significantly as the Dirac point was approached from either the conduction or valence band. In Fig. 2, we compare the computed energy-loss rate per carrier to the experimental values determined for different electron and hole densities in monolayer graphene. It may be observed that there is some curvature in the experimental data (open symbols) that is not matched by the theory. This could arise from the variation of the Bose integral, or from a temperature variation of the scattering time, which has not been considered here. In general, though, the agreement is quantitatively good, which is remarkable as there are essentially no adjustable parameters other than the fit to the scattering rate.

4 The energy relaxation time

Another important parameter for hot carrier cooling is the energy relaxation time. Normally, this is obtained from (11) by factoring the cubic terms to give a definition of the energy relaxation time from the theoretical parameters [53]

$$P_e = \frac{k_B\left(T_e - T_L\right)}{\tau_e}, \tag{12}$$

where P_e is the power loss per electron. It is τ_e that actually describes the time over which the energy is taken out of the streaming term (Fig. 1). In Fig. 3, we compare the temperature-dependent variation of τ_e found from the present theory. To obtain the theoretical values, the electron temperature that is found from the excitation current at a particular density [16] is used to determine the power lost, and this is introduced into (12) to compute τ_e. From this figure, we see that the plasmon-based model reproduces not only the low-temperature magnitude of τ_e, but that it also captures its quantitative dependence on temperature.

The most striking observation of Ref. [16] was of a strong variation of τ_e as a function of carrier density. This behavior is reproduced in Fig. 4, along with the results of our calculations. The main panel compares the behavior observed at a number of different electron temperatures, and again shows close, if not perfect, agreement between experiment and theory. One may note that there is an asymmetry between the electron and hole sides of the plot, the origin of which is a similar asymmetry in the gate-voltage dependent conductance measured in experiment [16]. On the electron side, it appears that there is a soft saturation setting in above $\sim 10^{12}\,\mathrm{cm}^{-2}$, which is not apparent on the hole side. Whether his has significance is not clear at this time. The electron temperature is extracted from the experimental data, and we note that the sample was chemically-doped such that a positive gate bias was necessary to bring the Fermi energy to the Dirac point. It is possible then that this negative charge could have induced some asymmetry into the results. In the inset to Fig. 4, we plot the variation of τ_e as a function of electron density, for

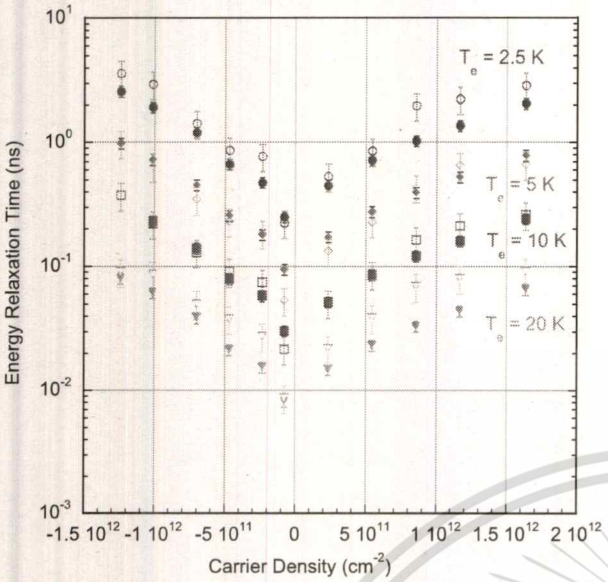

Fig. 4 Comparison of the calculated energy relaxation time with that measured in Ref. [16] for several values of the electron temperature. The *open symbols* are experimental data while the *solid symbols* are the theoretical values

three different measurement currents. As with the data in the main panel, we see that the theory reproduces the experiment well in this figure also.

The plasmon loss mechanism rearranges the energy distribution function, but this energy remains in the electron gas as a whole. Under the excitation current (or electric field), the distribution function is shifted in momentum space to reflect the current, and it spreads as the electron temperature rises. The shift can also distort the distribution to produce an elongated extension in the direction of the field or current. The ultimate limit of this elongation is a delta function in the field direction [4]. Between the shift in momentum space, and the elongation, the distribution function has more carriers in the forward direction than the backward direction. The plasmon loss takes carriers from the streaming forward direction and moves them to the backward direction, in the symmetric terms of the distribution function, on the average. This relaxes the streaming distribution, but the ultimate result still remains that another process must pass the energy to the lattice. This can be due to the acoustic phonon process [22–27] or even the super-collision process [26]. However, it is the plasmon interaction that dominates what is seen experimentally as it is this process which moves the current carrying particles out of the forward extension of the distribution function. The other processes which ultimately move the energy to the lattice are thus masked, and this would be even more true with the supercollision process as it has the same temperature dependence (i.e., $p = 3$) as that found here.

In conclusion, the good quantitative agreement between the experimental data of Ref. [16] and the theoretical results obtained here suggests that the plasmon interaction dominates hot-carrier energy relaxation in graphene at low temperatures. Since the role of this mechanism in governing energy loss does not appear to have been appreciated thus far, it suggests that its relevance may be far wider than simply the experimental study analyzed here.

Appendix 1

We note that the emission and absorption of plasmons by hot carriers is not the normal Fermi liquid behavior. If the Fermi sea is completely full at zero Kelvin, then there can be no emission at the Fermi level since the lower energy states are full. We need a spreading of the distribution function at an elevated temperature arising from the hot electron effect, induced by the electric field as shown in Fig. 1. The phase space interaction, illustrating conservation of both energy and momentum can be sketched as in Fig. 5, for both emission and absorption. Here, we show two circles which are the constant energy rings for the states $E(\mathbf{k})$ and $E(\mathbf{k} \pm \mathbf{q})$. These rings are separated by the plasmon energy, which is q dependent. The red ring is the Fermi circle for the initial state, and the blue ring is the Fermi circle for the final state. The initial and final momenta are, of course, connected vectorially by the momentum of the plasmon, so that momentum conservation, as well as energy conservation, is assured in the interaction. Panel (a) represents the situation for plasmon emission, while (b) represents the situation for plasmon absorption.

We begin by writing the energy conservation for the emission process in terms of the magnitudes of the various vectors as

$$\hbar v_F \left(|\mathbf{k}| - |\mathbf{k} - \mathbf{q}|\right) = \hbar \omega_p = \hbar \sqrt{\chi_2 q} \tag{13}$$

where the plasma frequency has been given in the main text by (3). Here, we have introduced the proper dynamic mass for graphene in the last term. We can now expand the terms in the first equation to get

$$k - \sqrt{k^2 + q^2 + 2kq\cos\vartheta} = \frac{\sqrt{\chi_2 q}}{v_F}. \tag{14}$$

It is important to note here that the vector properties of Fig. 5a mean that $\cos\vartheta < 0$, or that the angle is in the second or third quadrants. We can now rearrange the terms and square the result to get

$$k^2 + \frac{\chi_2 q}{v_F^2} - 2k\frac{\sqrt{\chi_2 q}}{v_F} = k^2 + q^2 + 2kq\cos\vartheta. \tag{15}$$

Fig. 5 Diagrams for the conservation of momentum and energy in the plasmon interaction for **a** emission and **b** absorption

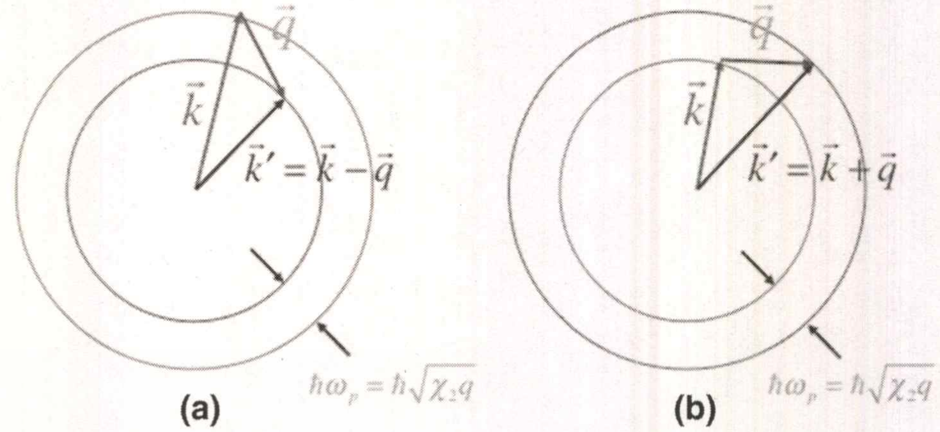

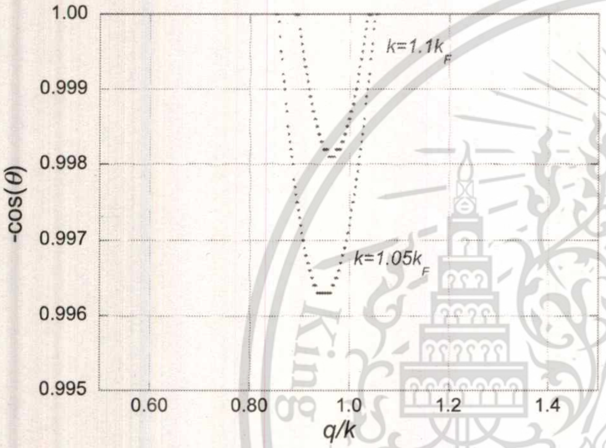

Fig. 6 The *lines* for which the delta function is satisfied for the emission of plasmons at two different values of energy of the carriers, as given by (16)

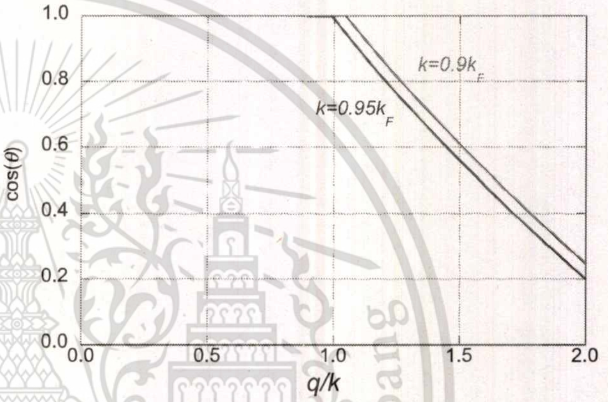

Fig. 7 The *lines* for which the delta function is satisfied for the absorption of plasmons at two different values of energy of the carriers, as given by (20)

or

$$\cos\vartheta = -\frac{q^2 - \frac{\chi_2 q}{v_F^2} + 2k\frac{\sqrt{\chi_2 q}}{v_F}}{2kq} = -\left[\frac{q}{2k} - \frac{\chi_2}{2kv_F^2} + \frac{1}{v_F}\sqrt{\frac{\chi_2}{q}}\right]. \tag{16}$$

Thus, we require the term in square brackets to be positive. The solutions are shown in Fig. 6.

Now, we turn to the absorption process and write the energy conservation in terms of the magnitudes of the various vectors as

$$\hbar v_F\left(|\mathbf{k}+\mathbf{q}| - |\mathbf{k}|\right) = \hbar\omega_p = \hbar\sqrt{\chi_2 q}. \tag{17}$$

We can now expand the terms in the first equation to get

$$\sqrt{k^2 + q^2 + 2kq\cos\vartheta} - k = \frac{\sqrt{\chi_2 q}}{v_F}. \tag{18}$$

It is important to note here that the vector properties of Fig. 5b mean that $\cos\vartheta > 0$, or that the angle is in the first or fourth quadrants. We can now rearrange the terms and square the result to get

$$k^2 + \frac{\chi_2 q}{v_F^2} + 2k\frac{\sqrt{\chi_2 q}}{v_F} = k^2 + q^2 + 2kq\cos\vartheta, \tag{19}$$

or

$$\cos\vartheta = \frac{-q^2 + \frac{\chi_2 q}{v_F^2} + 2k\frac{\sqrt{\chi_2 q}}{v_F}}{2kq} = \left[-\frac{q}{2k} + \frac{\chi_2}{2kv_F^2} + \frac{1}{v_F}\sqrt{\frac{\chi_2}{q}}\right]. \tag{20}$$

Thus, we require the term in square brackets to be positive (Fig. 7).

It is clear that there are solutions to the above equations which allow for both emission and absorption of plasmons.

In the emission case, the scattering lies in a very small range of angles whose "cone" is 6°–10° for the curves shown. This is around the back-scattered direction and has a momentum almost equal to that of the initial state. Hence, this is almost back scattering, but not quite (we note that pure back-scattering in graphene is forbidden in the equilibrium case by chirality). For absorption, there is a very large range of angles for the forward process, but again it occurs for rather large values of the momentum. In both emission and absorption, the scattering involves rather large values of the plasmon energy. There is almost no density dependence in the range of $10^{11} - 10^{12}$ cm^{-2}, but one would expect the interaction to get stronger nearer to the Dirac point, although the plasmon may be damped strongly in this case by the interband single particle interactions discussed above.

Appendix 2

The integral in (10) may be written as

$$I = \int_0^{u_{\max}} \frac{u^2 du}{e^u - 1} \tag{21}$$

where

$$u = \frac{\hbar v_F q}{k_B T}, \quad u_{\max} = \frac{2\hbar v_F k_F}{k_B T}. \tag{22}$$

The first term arises from the energy conserving delta function that appears in the integration over the frequency. The second term arises from the fact that the maximum value of q that can occur is approximately the span of the Fermi circle in two dimensions, which translates into a maximum value for u. Generally, this maximum is twice the ratio of the Fermi energy to the thermal energy, and can be quite large. In Fig. 8, we plot both the integrand and the value of the integral as a function of u or $u_{\max}$, as appropriate. It may be seen that the peak of the argument occurs at a relatively small value of u, due to the dominance of the exponential in the denominator. The integral approaches its limiting value fairly rapidly. The smallest value of the limit occurs for low density and high temperature. In the experiments [16], the lowest value of density is about 2×10^{11} cm^{-2} while the highest carrier temperature is about 40 K. These numbers lead to a minimum value of u_{max} of about 2.4 where the integral has already reached more than half its final value. So, except for low densities at the highest input power per electron, the integral can reasonably be assumed to be the limiting value of approximately 2.4.

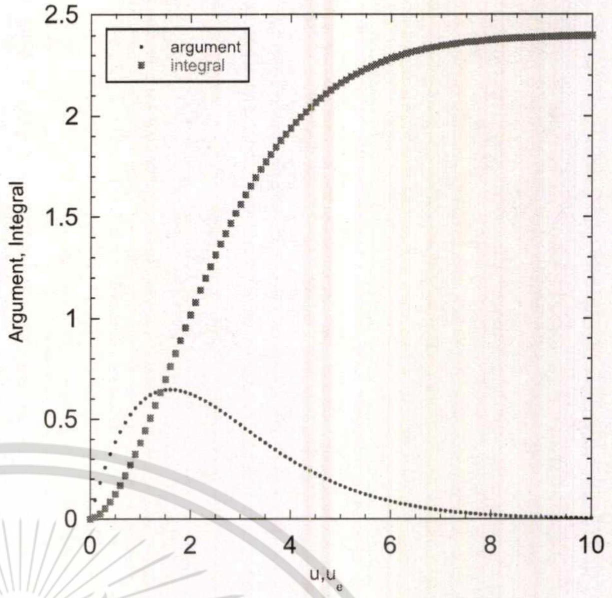

Fig. 8 The argument and value of the integral (21) as a function of the argument or limit

Appendix 3

The mobility that is measured in the samples as a function of temperature for various densities is shown in Fig. 9. To get to the needed scattering time, one must understand how the various scattering rates are averaged over the scattering angle (See, e.g., [56]). With several scattering mechanisms active in graphene, this is actually rather difficult to unfold. We have considered impurity scattering to be dominant. The actual scattering rate differs from the momentum relaxation

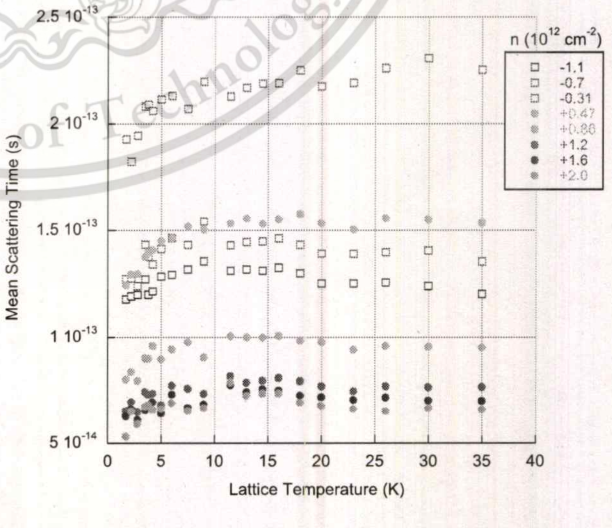

Fig. 9 The momentum relaxation time as a function of temperature for several values of the carrier density

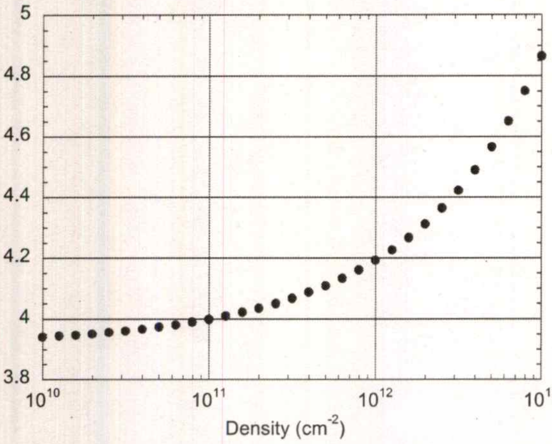

Fig. 10 The ratio of the momentum relaxation time to the actual scattering time for ionized impurity scattering in graphene

time determined from the measured mobility. The actual scattering rate from ionized impurity scattering in graphene can be written as [57]

$$\frac{1}{\tau_{imp}} = \frac{N_{imp}}{4\pi\hbar E_k}\left(\frac{Ze^2}{\varepsilon_s}\right)^2 \int_0^{\pi} \frac{[1+\cos(2\vartheta)]\, e^{-4k\sin(\vartheta)d_s}\, d\vartheta}{\left[\sin(\vartheta)+\frac{q_s}{2k}\right]^2} \tag{23}$$

where $e^2k_F/2\pi\varepsilon_s$ is the screening wave vector and 2θ is the angle between the incoming and scattered wave vectors—the elastic scattering occurs with $q = 2k\cos(\theta/2)$, and the angle has been doubled in the equation. In the momentum relaxation time, there is an additional factor of $[1-\cos(2\theta)]$ in the numerator (See, e.g., [58]). So, the ratio of the momentum relaxation time to the actual scattering time is the ratio of the integrals with, and without, this additional term. This ratio is shown in Fig. 10, with the scattering rates all evaluated at the Fermi surface, appropriate for low temperatures. In graphene, the mobility in suspended graphene is quite high, and can be of the order of several times 10^5 cm^2/s [59]. The mobility in the experiments discussed in Ref. [16], and used in the manuscript, are much lower and so are assumed to dominated by impurity scattering. Hence, the ratio in Fig. 6 was used to convert the momentum relaxation time into the actual scattering time used in the computation of the energy loss rate per electron.

References

1. Conwell, E.M.: High Field Transport in Semiconductors. Academic Press, New York (1967)
2. Yamashita, J., Watanabe, M.: On the conductivity of non-polar crystals in the strong electric field, I. Prog. Theor. Phys. **12**, 443 (1954)
3. Reik, H.G., Risken, H.: Distribtuion functions for hot electrons in many-valley semiconductors. Phys. Rev. **124**, 777 (1961)
4. Baraff, G.A.: Distribtuion functions and ionization rates for hot electrons in semiconductors. Phys. Rev. **128**, 2507 (1962)
5. Meric, I., Han, M.Y., Young, A.F., Ozylimaz, B., Kim, P., Shepard, K.L.: Current saturation in zero-bandgap, top-gated graphene field-effect transistors. Nat. Nanotechnol. **3**, 654 (2008)
6. Freitag, M., Steiner, M., Martin, Y., Perebeinos, V., Chen, Z., Tsang, J.C., Avouris, P.: Energy dissipation in graphene field-effect transistors. Nano Lett. **9**, 1883 (2009)
7. Barreiro, A., Lazzeri, M., Moser, J., Mauri, F., Bachtold, A.: Transport properties of graphene in the high-current limit. Phys. Rev. Lett. **103**, 076601 (2009)
8. Plochocka, P., Kossacki, P., Golnik, A., Kazimierczuk, T., Berger, C., de Heer, W.A., Potemski, M.: Slowing hot-carrier relaxationin graphene using a magnetic field. Phys. Rev. B **80**, 245415 (2009)
9. Voutilainen, J., Fay, A., Häkkinen, P., Viljas, J.K., Heikkilä, T.T., Hakonen, P.J.: Energy relaxation in graphene and its measurement with supercurrent. Phys. Rev. B **84**, 045419 (2011)
10. Tan, Z., Ma, L., Liu, G.T., Lu, L., Yang, C.L.: Shubnikov-de Haas oscillations of a single layer graphene under dc current bias. Phys. Rev. B **84**, 115429 (2011)
11. Sun, D., Divin, C., Berger, C., de Heer, W.A., First, P.N., Norris, T.B.: Hot carrier cooling by acoustic phonons in epitaxial graphene by ultrafast pump-probe spectroscopy. Phys. Status Solidi C **8**, 1194 (2011)
12. Majumdar, K., Kallatt, S., Bhat, N.: High field carrier transport in graphene: insights from fast current transient. Appl. Phys. Lett. **101**, 123505 (2012)
13. Baker, A.M.R., Alexander-Webber, J.A., Altebaeumer, Y., Nicholas, R.J.: Energy relaxation for hot Dirac fermions in graphene and breakdown of the quantum Hall effect. Phys. Rev. B **85**, 115403 (2012)
14. Price, A.S., Hornett, S.M., Shytov, A.V., Hendry, E., Horsell, D.W.: Nonlinear resistivity and heat dissipation in monolayer graphene. Phys. Rev. B **85**, 161411(R) (2012)
15. Betz, A.C., Vialla, F., Brunel, D., Voisin, C., Picher, M., Cavanna, A., Madouri, A., Fève, G., Berroir, J.-M., Plaçais, B., Pallechi, E.: Hot electron cooling by acoustic phonons in graphene. Phys. Rev. Lett. **109**, 056805 (2012)
16. Somphonsane, R., Ramamoorthy, H., Bohra, G., Ferry, D.K., Ochiai, Y., Aoki, N., Bird, J.P.: Fast energy relaxation of hot carriers near the dirac point of graphene. Nano Lett. **13**, 4305 (2013)
17. Baker, A.M.R., Alexander-Weber, J.A., Altebaeumer, T., McMullan, S.D., Janssen, T.J.B.M., Tzalenchuk, A., Lara-Avila, S., Kubatkin, S., Yakimova, R., Lin, C.-T., Li, L.-J., Nicholas, R.J.: Energy loss rates of hot Dirac fermions in epitaxial exfoliated, and CVD graphene. Phys. Rev. B **87**, 045414 (2013)
18. Graham, M.W., Shi, S.-F., Ralph, D.C., Park, J., McEuen, P.L.: Photocurrent measurements of supercollision cooling in graphene. Nat. Phys. **9**, 103 (2013)
19. Graham, M.W., Shi, S., Wang, Z., Ralph, D.C., Park, J., McEuen, P.L.: Transient absorption and photocurrent microscopy show that hot electron supercollisions describe the rate-limiting relaxation step in graphene. Nano Lett. **13**, 5497 (2013)
20. Betz, A.C., Jhang, S.H., Pallecchi, E., Ferreira, R., Fève, G., Berroir, J.-M., Plaçais, B.: Supercollision cooling in undoped graphene. Nat. Phys. **9**, 109 (2013)
21. Borzenets, J.V., Coskun, U.C., Mebrahtu, H.T., Bomze, YuV, Smirnov, A.I., Finkelstein, G.: Phonon bottleneck in graphene-based josephson junctions at millikelvin temperatures. Phys. Rev. Lett. **111**, 027001 (2013)

22. Bistritzer, R., MacDonald, A.H.: Electronic cooling in graphene. Phys. Rev. Lett. **102**, 206410 (2009)
23. Kubakaddi, S.: Interaction of massless Dirac electrons with acoustic phonons in graphene at low temperatures. Phys. Rev. B **79**, 075417 (2009)
24. Tse, W.K., Das Sarma, S.: Energy relaxation of hot Dirac fermions in graphene. Phys. Rev. B **81**, 235406 (2009)
25. Viljas, J.K., Heikkilä, T.T.: Electron-phonon heat transfer in monolayer and bilayer graphene. Phys. Rev. B **81**, 245404 (2010)
26. Song, J.C.W., Reizer, M.Y., Levitov, L.S.: Disorder-assisted electron-phonon scattering and cooling pathways in graphene. Phys. Rev. Lett. **109**, 106602 (2012)
27. Virtanen, P.: Energy transport via multphonon processes in graphene. Phys. Rev. B **89**, 245409 (2014)
28. Fischetti, M.V., Kim, J., Nayaranan, S., Ong, Z.-Y., Sachs, C., Ferry, D.K., Aboud, S.J.: Pseudopotential-based studies of electron transport in graphene and graphene nanoribbons. J. Phys. Cond. Matter **25**, 473202 (2013)
29. Eless, V., Yager, T., Spasov, S., Lara-Avila, S., Yakimova, R., Kubatkin, S., Janssen, T.J.M., Tzalenchuk, A., Antonov, V.: Phase coherence and energy relaxation in epitaxial graphene under microwave radiation. Appl. Phys. Lett. **103**, 093103 (2013)
30. Gantmahker, V.F., Levinson, Y.B.: Carrier Scattering in Metals and Semiconductors. North-Holland, Amsterdam (1987). Sec. 6.4
31. Ferrell, R.A.: Angular dependence of the characteristic energy loss of electrons passing through metal foils. Phys. Rev. **101**, 554 (1956)
32. Klimontovich, Y.L.: Charged particle energy losses due to excitation of plasma oscillations. Sov. Phys. JETP **9**, 999 (1959)
33. Varga, B.B.: Coupling of plasmons to polar phonons in degenerate semiconductors. Phys. Rev. **137**, A1896 (1965)
34. Mooradian, A., Wright, G.B.: Observation of the interaction of plasmons with longitudinal optical phonons in GaAs. Phys. Rev. Lett. **16**, 999 (1966)
35. Kim, M.E., Das, A., Senturia, S.: Electron scattering interadtion with coupled plasmon-polar modes in degeneratre semiconductors. Phys. Rev. B **18**, 6890 (1978)
36. Kasiyan, A.I., Russo, P.I.: Influence of plasma oscillations on the mobility of carriers in polar semiconductors. Sov. Phys. Semicond. **15**, 1142 (1982)
37. Kumekov, S.E., Perel, V.I.: Relaxation of fast electrons in semiocnducotrs at coupled plasmon-phonon oscillations. Sov. Phys. Semicond. **16**, 1291 (1982)
38. Lugli, P., Ferry, D.K.: Investigaation of plasomn-induced losses in quasi-ballistic transport. IEEE Electron Dev. Lett. **4**, 25 (1985)
39. Lugli, P., Ferry, D.K.: Electron-electron interaction and high field transport in Si. Appl. Phys. Lett. **46**, 594 (1985)
40. Lin, M.F., Shung, K.W.K.: Plasmons and optical properties of carbon nanotubes. Phys. Rev. B **50**, 17744 (1994)
41. Wunsch, B., Stauber, T., Sols, F., Guinea, F.: Dynamical polarization of graphene at finite doping. New J. Phys. **8**, 318 (2006)
42. Hwang, E.H., Das Sarma, S.: Dielectric function, screening, and plasmons in two-dimensional graphene. Phys. Rev. B **75**, 205418 (2007)
43. Guiliani, G.F., Quinn, J.J.: Lifetime of a quasiparticle in a two-dimensional electron gas. Phys. Rev. B **26**, 4421 (1982)
44. Altshuler, B.L., Aronov, A.G., Khemelnitskii, D.E.: Effects of electron-electron collisions with small energy transfers on quantum localisation. J. Phys. C **15**, 7367 (1982)
45. Golubev, D.S., Zaikin, A.D.: Quantum decoherence in disordered mesoscopic systems. Phys. Rev. Lett. **81**, 1074 (1998)
46. Tse, W.-K., Hwang, E.H., Das Sarma, S.: Ballistic hot electron transport in graphene. Appl. Phys. Lett. **93**, 023128 (2008)
47. Hwang, E.H., Das Sarma, S.: Quasiparticle spectral function in doped graphene: electron-electron interaction effects in ARPES. Phys. Rev. B **77**, 081412 (2008)
48. Hwang, E.H., Hu, B.Y.-K., Das Sarma, S.: Inelastic carrier lifetime in graphene. Phys. Rev. B **76**, 115434 (2007)
49. Kotov, V.N., Uchoa, B., Pereira, V.M., Guinea, F., Castro-Neto, A.H.: Electron-electron interactions in graphene: current status and perspectives. Rev. Mod. Phys. **84**, 1067 (2012)
50. Hill, A., Mikhailov, S.A., Ziegler, K.: Dielectric function and plasmons in graphene. Europhys. Lett. **87**, 27005 (2009)
51. Lee, P.A., Ramakrishnan, T.V.: Disordered electronic systems. Rev. Mod. Phys. **57**, 287 (1985)
52. Altshuler, B.L., Aronov, A.G.: Electron-Electron interactions in disordered conductors. In: Efros, A.L., Pollak, M. (eds.) Electron-Electron Interactions in Disordered Systems, pp. 1–154. North-Holland, Amsterdam (1985)
53. Ferry, D.K.: Semiconductors. Macmillan, New York (1991). Sec. 10.3.1
54. Ferry, D.K., Goodnick, S.M., Bird, J.P.: Transport in Nanostructures, 2nd edn. Cambridge Univ. Press, Cambridge (2009). and references therein
55. Price, P.J.: Hot electrons in a GaAs heterolayer at low temperatures. J. Appl. Phys. **53**, 6863 (1982)
56. Shishir, R.S., Chen, F., Xia, J., Tao, N.J., Ferry, D.K.: Room temperature carrier transport in graphene. J. Comput. Electron. **8**, 43 (2009). and references therein
57. Ferry, D.K.: Short-range potential scattering and its effect on graphene mobility. J. Comput. Electron. **12**, 76 (2013)
58. Baccarani, C., Jacoboni, C., Mazzone, A.M.: Current transport in narrow-base transistors. Solid State Electron. **20**(5), 1–75 (1977)
59. Castro Neto, A.H., Guinea, F., Peres, N.M.R., Novoselov, K.S., Geim, A.K.: The electronic properties of graphene. Rev. Mod. Phys. **81**, 109 (2009)

NANO LETTERS

Letter

pubs.acs.org/NanoLett

Conduction Mechanisms in CVD-Grown Monolayer MoS_2 Transistors: From Variable-Range Hopping to Velocity Saturation

G. He,[†] K. Ghosh,[†] U. Singisetti,[†] H. Ramamoorthy,[†] R. Somphonsane,[‡] G. Bohra,[†] M. Matsunaga,[§] A. Higuchi,[§] N. Aoki,[§] S. Najmaei,[∥] Y. Gong,[∥] X. Zhang,[∥] R. Vajtai,[∥] P. M. Ajayan,[∥] and J. P. Bird[†,*]

[†]Department of Electrical Engineering, University at Buffalo, The State University of New York, Buffalo, New York 14260-1900, United States

[‡]Department of Physics, King Mongkut's Institute of Technology Ladkrabang, Bangkok 10520, Thailand

[§]Graduate School of Advanced Integration Science, Chiba University, 1-33 Yayoi-cho, Inage-ku, Chiba 263-8522, Japan

[∥]Department of Materials Science and NanoEngineering, Rice University, Houston, Texas 77005, United States

Supporting Information

ABSTRACT: We fabricate transistors from chemical vapor deposition-grown monolayer MoS_2 crystals and demonstrate excellent current saturation at large drain voltages (V_d). The low-field characteristics of these devices indicate that the electron mobility is likely limited by scattering from charged impurities. The current−voltage characteristics exhibit variable range hopping at low V_d and evidence of velocity saturation at higher V_d. This work confirms the excellent potential of MoS_2 as a possible channel-replacement material and highlights the role of multiple transport phenomena in governing its transistor action.

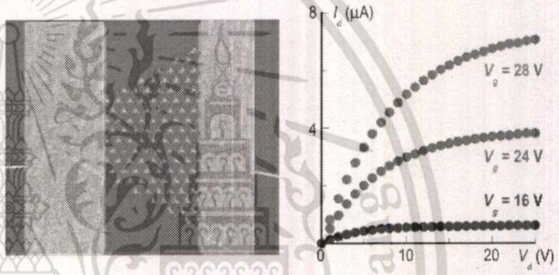

KEYWORDS: *Molybdenum disulfide, transition metal dichalcogenides, 2D transistors, high-field transport, velocity saturation*

Transition-metal dichalcogenides have recently emerged as a new class of electronic materials, which, much like graphene, may be isolated in a two-dimensional (2D) form to implement a variety of novel electronic devices.[1] Among the materials that comprise this group, molybdenum disulfide (MoS_2) is one whose characteristics appear particularly promising for such applications. In marked contrast to graphene, MoS_2 exhibits a large energy gap (1.3−1.8 eV), the direct nature of which in the monolayer form makes it attractive for not only transistor implementations but also optoelectronics. Efficient transistor action has been demonstrated for devices based on multilayer and monolayer MoS_2,[1−23] and these devices are characterized by large ($>10^7$) room-temperature ON-OFF ratios. They are also predicted to exhibit excellent subthreshold swing and benefit from immunity to short-channel effects.[24] Although the large effective mass ($m^* = 0.45m_o$) of the MoS_2 electrons means that they exhibit much lower mobility than the massless Fermions of graphene, this is not expected to be problematic for many applications involving transistor switching. In one pioneering study, MoS_2 transistors were used to implement small-scale integrated circuits,[25] providing essential Boolean functionality. Other work has demonstrated their application as sensitive photodetectors[26,27] capable of operating in the visible and UV ranges. Additionally, and in common with graphene, the ability to exploit valley polarization as a state variable in (monolayer) MoS_2 may open up the development of new "valleytronic" devices.[28−30]

In the vast majority of studies reported in the literature to date, MoS_2 transistors have been fabricated by mechanically exfoliating 2D material onto an insulating substrate from crystalline molybdenite.[2−9,13−18,20,22,23,25,26] Although this has the benefit of allowing rapid prototyping of individual devices, chemical routes to synthesis[10−12,19,21,31−33] offer the prospect of both high material yield and uniformity. Chemical vapor deposition (CVD), involving the sulfurization of molybdenum films deposited on Si/SiO_2 substrates, is one such promising approach.[11,12,19,31,32] Depending on the initial film thickness a variety of final structures can be realized, including monolayer crystals with areas of many tens of square microns. These structures may then easily be subjected to in situ device fabrication or may be released into solution for transfer to other substrates.[19] Structural characterization (via Raman spectroscopy and atomic-force microscopy) of the CVD-grown crystals confirms their monolayer,[11,12] highly crystalline[33] character, making this approach particularly attractive for transistor realization. Recently, there have been some reports[11,12,19] of the electrical characteristics of such devices, suggesting that they are able to compete with or even exceed the performance offered by their exfoliated counterparts. In ref 21, the authors presented a detailed study of the influence of thermal annealing

Received: March 24, 2015
Revised: May 20, 2015
Published: June 29, 2015

DOI: 10.1021/acs.nanolett.5b01159
Nano Lett. 2015, 15, 5052−5058

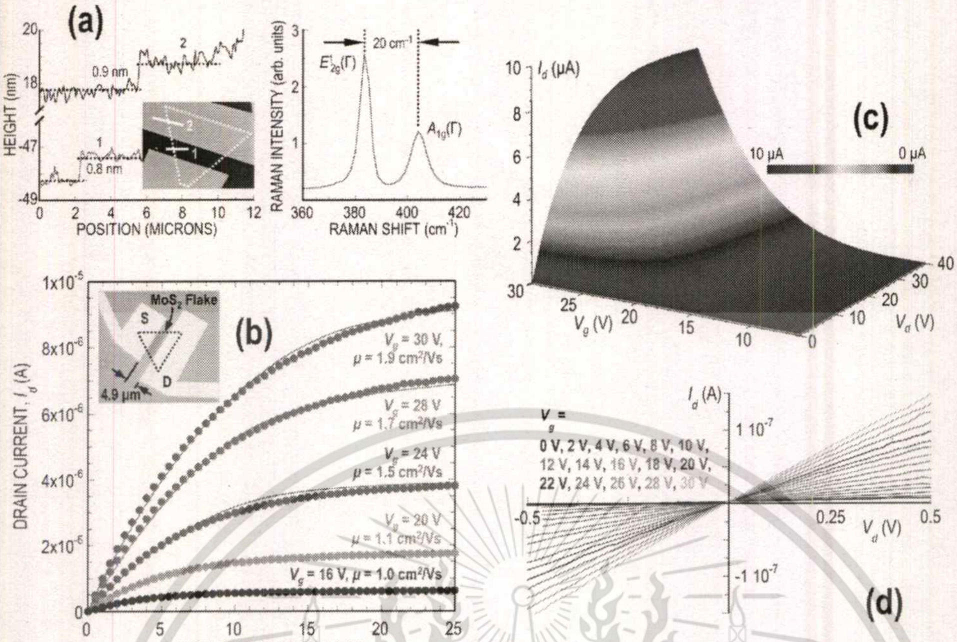

Figure 1. (a) Shown on the left are line scans recorded along the two white solid lines in the AFM image shown in the inset. The image is of MS2-13, and the outline of the MoS$_2$ crystal is indicated by the white dotted line. The figure on the right is a Raman spectrum obtained using a (514.5 nm wavelength, 1 μm spot size) laser to illuminate the channel of MS2-13. (b) Transistor curves measured at room temperature for transistor MS2-13 (shown in the false-color optical micrograph in the inset). Filled symbols are experimental data points, and solid lines represent the results of simulations (see main text for details). (c) Color contour plot showing the full evolution of $I_d(V_d, V_g)$ for device MS2-13. (d) Expanded view of the transistor curves around $V_d = 0$, showing the linearity of the current over the full range of V_g.

on the transistor characteristics and showed that this allowed low-temperature (10 K) mobility values as large as 500 cm^2 V^{-1} s^{-1}) to be obtained. Moreover, the authors were able to demonstrate evidence of a metal–insulator transition as a function of gate voltage, suggestive of the high electronic quality of the CVD-grown crystals.

In this Letter, we present the results of studies of the electrical properties of transistors implemented in CVD-grown, monolayer MoS$_2$. We demonstrate, for the first time, excellent current saturation in such devices and explore the role of different transport mechanisms in governing the dependence of their drain current (I_d) on the drain (V_d) and gate (V_g) voltages. For drain voltages in the linear regime, we observe clear signatures of variable-range hopping (VRH) in the temperature (T)-dependent conduction, reminiscent of prior studies of exfoliated MoS$_2$.[3,13] The VRH weakens with an increase in the gate voltage, presumably as electrons in the channel are able to more effectively screen out the impurity-related background potential. This behavior is accompanied at higher fields by the emergence of velocity saturation. The need to introduce the latter phenomenon arises from the strongly gate-voltage dependent character of the channel mobility (μ), and the saturation velocity ($v_{sat} = 3 \times 10^6$ cm s^{-1}) used to fit the experiment is found to closely match that reported in recent studies of multilayer MoS$_2$.[34] Simulations of the electrostatics within the device confirm that the velocity saturation arises from the presence of a strongly peaked electric field (E_y, where y is the direction along the channel length), which develops in the channel near the drain contact under current saturation.

Monolayer MoS$_2$ transistors were fabricated using electron-beam lithography and metal lift-off to form Cr/Au (5 nm/50 nm) source-drain contacts to CVD-grown single MoS$_2$ crystals synthesized on commercial Si/SiO$_2$ wafers. The heavily doped Si served as the back-gate of the transistor, whereas the 280 nm thick SiO$_2$ functioned as the gate dielectric and was also used to provide optical contrast when observing the MoS$_2$ crystals under an optical microscope. (In the ultimate applications, this design could be replaced with one consisting of a top gate formed on a thin layer of high-k dielectric, significantly lowering the working gate-voltage range while also enhancing the mobility through "engineering" of the dielectric environment.[2]) The CVD growth was performed by first dispersing MoO$_3$ nanoribbons onto the Si/SiO$_2$ substrate and then sulfurizing them in a furnace.[32] This process resulted in the formation of triangular-shaped single crystals, 13 ± 2.5 μm on a side, whose monolayer character was confirmed by both Raman studies and atomic-force microscopy. This is indicated in Figure 1(a), in which the measured thickness of the MoS$_2$ crystal and the separation of the E^1_{2g} (Γ) and A_{1g}(Γ) Raman peaks are both consistent with earlier reports for CVD grown monolayer MoS$_2$.[11,21]

The electrical characteristics of 13 different transistors were investigated for this study and were all found to exhibit fairly similar characteristics (see Table 1 of the Supporting Information, where we also define the notation used to identify the different transistors). For this reason, in our discussions here we focus on providing the results of a comprehensive study of a single device (MS2-13), which we have chosen due to its representative character. This device is shown as an inset in Figure 1(b), where the source (S) and drain (D) contacts are indicated. After fabrication, transistors were wirebonded into standard DIP packages and mounted in a cryostat, allowing

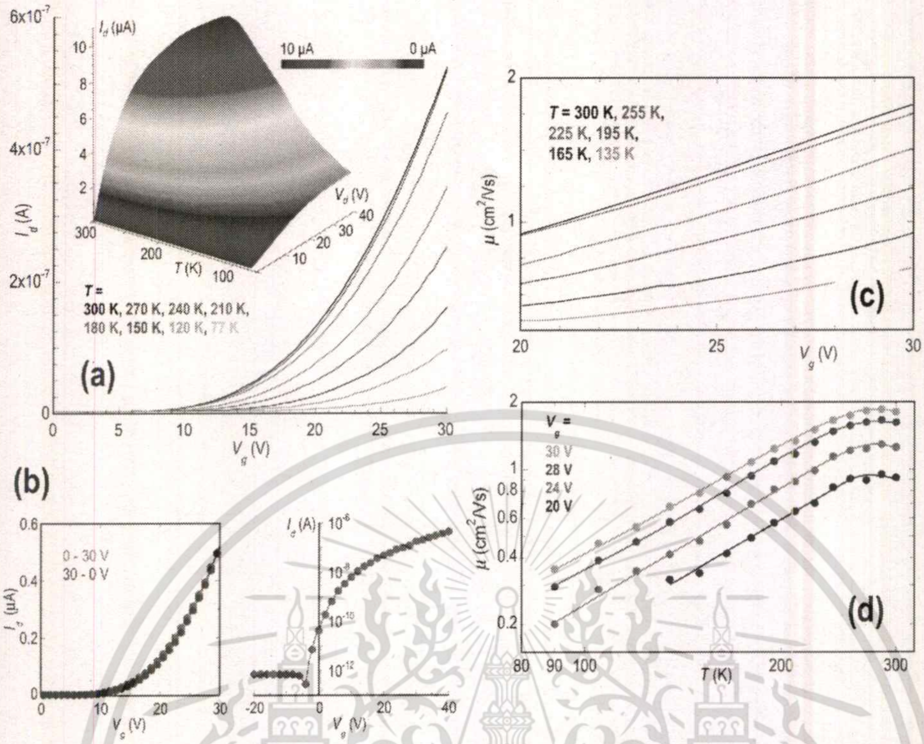

Figure 2. (a) Transfer characteristics of device MS2-13 (V_d = 0.5 V), measured at various temperatures from 77 to 300 K. The inset plots the variation of $I_d(V_d)$ as a function of temperature from 77 to 300 K. The gate voltage (V_g = 30 V) was held fixed for these measurements. (b) The left panel shows the transfer curve of MS2-13 measured at 300 K in both sweep directions (red and blue data). In the right panel, we use a semilog plot to reveal an on−off ratio at 300 K of ~6 orders of magnitude. The measurement was made with V_d = 1 V using a Keithley 4200 with a high resolution preamplifier. (c) Variation of mobility as a function of V_g, inferred (using eq 2) from the experimental data of (a) at different temperatures. (d) Variation of mobility as a function of temperature, inferred from the results of (c) at various gate voltages. The solid lines are trend lines that form a guide to the eye.

their electrical characteristics to be measured from 77 to 300 K with a Keithley 2400 source meter. The measurements reported here were obtained with the samples maintained under vacuum, in the dark, and in the absence of any annealing.[15,21] We have performed both in situ (under vacuum, 110 °C, 10^{-5} mbar, 20 h) and ex situ (also under vacuum, 120 °C, 10^{-5} mbar, 20 h) annealing of our devices, but in contrast to earlier reports,[15,21] do not find such a significant improvement in performance. The key features of transistor action (including the well-defined current saturation that we show below) are preserved after annealing, and current levels are increased by ~50%, but this improvement is much less dramatic than that achieved in refs 15 and 21. The reasons for this are unclear at present and require further investigation.

In Figure 1(b) and (c), we show measurements of the transistor curves of device MS2-13 at room temperature. Figure 1(b) shows the characteristics measured at several discrete gate voltages, along with corresponding theoretical fits (solid lines), whose details are provided further below. Figure 1(c) is a color contour that expresses the evolution of I_d as a continuous function of V_d and V_g. Both figures reveal classic transistor action with excellent saturation at high drain voltages, something that has not been demonstrated for CVD-grown MoS_2 devices (for which previous works have focused primarily on analyzing the transfer characteristics[11,12,15,19,21]). In Figure 1(d), we confirm the linear character of the current for small V_d and for a wide range of V_g. Typically, such linearity in two-terminal measurements is taken to indicate that good ohmic contact has been achieved to the MoS_2 channel.[21]

In the main panel of Figure 2(a), we present measurements of the transfer (I_d–V_g) characteristic of transistor MS2-13 at a series of temperatures from 77 to 300 K. As indicated in Figure 2(b), the transfer curve showed little hysteresis as a function of sweep direction (left panel), and yielded a room-temperature on−off ratio of ~6 orders of magnitude (right panel). Regardless of the temperature in Figure 2(a), it is noted that none of the curves show the linear variation $I_d(V_g)$ expected from a simple square-law model[35]

$$I_d = \frac{W\mu}{L}\frac{\varepsilon_{ox}\varepsilon_o}{x_o}\left[(V_g - V_T)V_d - \frac{{V_d}^2}{2}\right] \tag{1}$$

Here, V_T is the threshold voltage, L is the channel length, x_o is the oxide thickness, and ε_{ox} is its dielectric constant. W is the channel width, which in this work is taken as the average width of the MoS_2 crystal at the source and drain ends. μ is an effective channel mobility and, when this parameter is independent of gate voltage, its value can be determined from the linear relation between the drain current and the gate voltage [i.e., $\mu = (dI_d/dV_g)(x_o/(\varepsilon_{ox}\ \varepsilon_o))(L/WV_d)$]. The nonlinearity of the curves in Figure 2(a) indicates that the mobility in these devices is gate-voltage dependent however, requiring us to determine μ by solving the following expression (for details see the Supporting Information).

$$\mu + (V_g - V_T)\frac{d\mu}{dV_g} = \frac{L}{W}\frac{x_o}{\varepsilon_{ox}\varepsilon_o}\frac{1}{V_d}\frac{dI_d}{dV_g} \tag{2}$$

In Figure 2(c), we plot the variation of $\mu(V_g)$ determined from the experimental transfer curves at various temperatures using eq 2. The mobility clearly increases in an almost linear manner with increasing V_g and is also systematically larger at higher temperatures. This latter point can be seen explicitly in Figure 2(d), where we plot the variation of $\mu(T)$ at four different values of V_g. The behavior here is similar to that found previously for exfoliated MoS_2[17] and is consistent with the role of charged-impurity scattering.[1,5] The temperature dependence of the mobility is reflected as a strong variation of the transistor curves, as we indicate in the inset to Figure 2(a). This color contour plots the I_d–V_d characteristic of transistor MS2-13 at fixed gate voltage and at a series of different temperatures. As the mobility increases with temperature, the overall current level exhibits significant growth. At every temperature, however, we observe clear signatures of the linear- and saturated-current regimes, indicating that the transistor action is robust.

Turning to the issue of the conduction mechanism in the MoS_2 transistors, this is strongly dependent upon both the drain and gate voltages. For small V_d, we observe clear signatures of 2D VRH in the resistance[3,13]

$$R \propto R_o \exp\left[\left(\frac{T_o}{T}\right)^{1/3}\right] \tag{3}$$

where R_o and T_o are appropriate fit parameters. In Figure 3(a), we show the variation of the resistance (R) as a function $T^{-1/3}$ (on a semilog plot) and obtain good agreement with the VRH form for a wide range of gate voltages. The resistance values plotted here were determined at $V_d = 1$ V, well within the linear regime of transistor operation. In Figure 3(b), we plot the variation of T_o, inferred from the data of Figure 3(a), as a function of the gate voltage. Clearly, there is a trend for T_o to decrease with an increase in V_g, indicating that the role of the VRH is correspondingly reduced. We have already noted that the increase in mobility that we observe upon increasing temperature is indicative of the role of strong charged-impurity scattering. The related observation of VRH suggests that these charged impurities, which are presumably associated with the substrate,[3] also give rise to the disordered potential landscape needed for hopping to dominate. As the carrier concentration is increased by raising the gate voltage, screening of the impurity potential should then suppress the role of the hopping. MoS_2, like graphene, is known to be characterized by inefficient screening, particularly when prepared in few-layer form.[36−39] Estimates for the screening length vary, dependent upon the number of layers, but are typically in the range of several nanometers.[36−39] Screening of the impurity potential will therefore be incomplete in the devices, but we nonetheless expect that it should improve as the carrier concentration increases.[40] From our SILVACO simulations described in further detail below, we find that an increase in the gate voltage from 16 to 30 V should raise the carrier concentration in the MoS_2 from 0.4×10^{12} to 2.2×10^{12} cm^{-2}. According to recent theoretical work,[40] the increased density should lead to improved screening, and it is this phenomenon that we suggest is responsible for the modest improvements in mobility achieved in Figure 2(c).

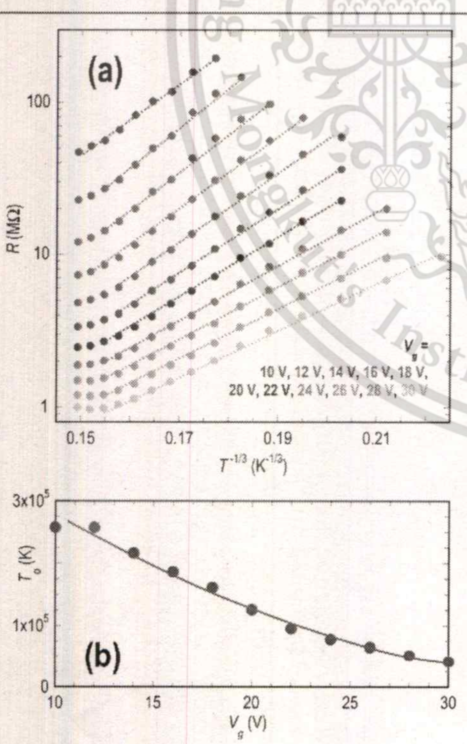

Figure 3. (a) Temperature-dependent variation in the resistance of device MS2-13 plotted to reveal the connection to VRH. A source voltage of $V_d = 1$ V was used for these measurements. (b) Gate-voltage-dependent variation of the VRH parameter T_o (see eq 3).

For a more quantitative understanding of transistor action, we have simulated the performance of the devices using the SILVACO Atlas package.[41] Details of the calculations are provided in the Supporting Information, along with a full list of the material parameters used. The essential idea, however, is that the monolayer MoS_2 crystal is treated as a 0.5 nm thick film, and a classical drift-diffusion model is used to simulate the drain current. The calculations explicitly consider the triangular shape of the MoS_2, and use micrographs of the actual device to determine the orientation of the crystal relative to the contacts. To account for the influence of velocity saturation, a field-dependent mobility ($\mu(E_y)$) is used, such that

$$\mu(E_y) = \mu_o\left[\frac{1}{1 + (\mu_o E_y / v_{sat})^{\beta}}\right]^{1/\beta} \tag{4}$$

where E_y is the electric field along the direction of current flow. Because the conduction in these devices is dominated by electrons, we take the parameter $\beta = 2$.[42] The low-field mobility (μ_o) in eq 4 is then determined by fitting the drain current to match that obtained in the linear region of the transistor curves.

Using the approach described above, we are able to successfully reproduce the experimental transistor curves of Figure 1(b). In doing so, we infer low-field mobility values in good agreement with those determined from the experimental data. This is illustrated in the inset to Figure 4(b), where we plot as discrete points the mobility values used in our simulations and compare them with those determined experimentally at room temperature. The agreement between the simulation and experiment is good, being within the error bars associated with the former. (The error bars reflect

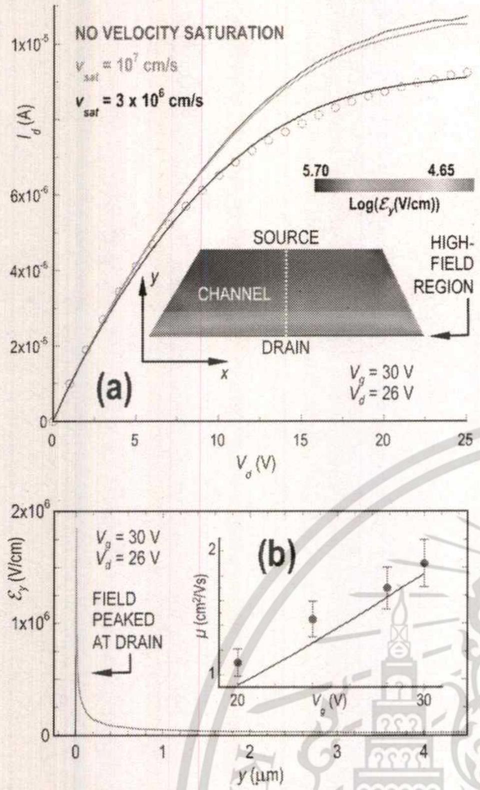

Figure 4. (a) Simulated fits to the drain current (V_g = 30 V), using different values for v_{sat} (indicated). A saturated velocity of 3×10^6 cm s^{-1} is found to best fit the experimental data (open symbols). The inset plots the calculated electric field strength (E_y) as a function of position within the channel (for V_g = 30 V, V_d = 26 V). The field strength is plotted on a log scale here (see color bar) and is strongly peaked at the drain end. (b) Variation of E_y as a function of position along the center line of the channel, indicated by the white dotted line. $y = 0$ corresponds to the drain end of the device. V_g = 30 V; V_d = 26 V. (inset) Comparison of experimentally determined mobility at 300 K with that used in the simulations to match the transistor curves. Device MS2-13. Solid line: experimental data. Filled symbols: simulated mobility values.

primarily the variation that arises when computing the mobility using the width of the triangular channel at its source and drain ends. The data points themselves were obtained by using an averaged valued for this width.)

An important feature revealed by our simulations is that current saturation at large V_d results from an interplay between channel pinch-off at the drain end and velocity saturation of electrons in the channel. At low gate voltages, where the mobility is small, the current saturation results primarily from pinch-off, whereas the converse is true at higher gate voltages. Referring to the transistor curves of Figure 1, for example, for gate voltages lower than 25 V, our simulations show that the drain current is generally consistent with a simple square-law model without the need for any velocity saturation. For larger gate voltages, however, agreement with the experiment is only possible by properly accounting for velocity saturation. This can be seen in Figure 4(a), where we show how the choice of different values for v_{sat} influences the computed current. The experimental data are plotted as open symbols in the figure, and it is clear that, with no velocity saturation (green line) or with an assumed $v_{sat} = 10^7$ cm s^{-1} (blue line), the simulated current is significantly larger than the experimental current. With v_{sat} = 3×10^6 cm s^{-1}, a value suggested in previous work on multilayer MoS_2 transistors,[34] however, the agreement is very good. In the inset to Figure 4(a), we plot a 2D surface contour of the channel field (E_y) using a logarithmic scale. The figure reveals that the velocity saturation is due to the strongly peaked nature of this field near the drain, a feature that can also be seen in Figure 4(b). Here, we plot the variation of E_y as a function of position (y) along the center line indicated by the white dotted line in the color contour of Figure 4(a). The field at the drain end approaches 2×10^6 V cm^{-1}, from which value and the mobility of 1.9 cm^2 V^{-1} s^{-1}, we obtain an estimate for the saturated velocity of 3.8×10^6 cm s^{-1}. This is consistent with our discussion above regarding the influence of the velocity saturation on the drain current in Figure 4(a).

The mobility values determined here (~1−10 cm^2 V^{-1} s^{-1}, see Table 1 in the Supporting Information) are, in many cases, much lower than those reported elsewhere. Putting aside the fact that the estimates provided in many of these studies have been called into question by others,[43] there are three primary issues that are likely at play here. First, our measurements are performed on unannealed devices, whereas thermal annealing has been demonstrated to provide improvements in the mobility.[15,21] Second, and perhaps more importantly, our work here shows that the mobility is strongly gate-voltage dependent, such that further increasing the gate voltage beyond the threshold can be expected to result in larger mobility values. In ref 21, for example, room-temperature mobility as large as 50−60 cm^2 V^{-1} s^{-1} was reported but was achieved by using back-gate voltages approaching 100 V. Finally, our two-terminal measurements may be influenced by contact resistance, which would result in an underestimate of the mobility. Although contact resistance was not included in the simulations shown in Figure 4, we have performed calculations in which the source/drain contact resistance was increased up to 1 kΩ (inclusion of larger values than this introduces problems with convergence) and did not observe any significant change in drain current. This can be attributed to the much lower conductance of the FET channel itself.

It is informative to compare the results of our study with those found in similar investigations of multilayer MoS_2 transistors. We have seen here that the current saturation in our devices arises from a combination of usual electrostatics (i.e., pinch-off at the drain) supplemented by velocity saturation that becomes important as the channel mobility improves. Current saturation has also been reported for multilayer devices[5,7,18,20,34] and has similarly been discussed in terms of long-channel pinch-off[5] and velocity saturation.[34] However, the much higher mobility exhibited by multilayer MoS_2[37] results in saturated current values that may be >2 orders of magnitude larger[5,20,34] than those reported here. In this sense, it is clear that multilayer devices are more attractive than monolayer ones for applications requiring larger drive currents. Nonetheless, in spite of its lower mobility, monolayer MoS_2 benefits from a larger gap (1.8 eV) than its multilayer counterpart (1.2 eV), offering the potential of a lower off current. Additionally, and in contrast to multilayer MoS_2, its direct band structure makes monolayer material attractive for various light-emitting devices. In this sense, both monolayer and multilayer devices possess their own advantageous characteristics, making them suitable for very distinct applications.

In conclusion, we have fabricated transistors from CVD-grown monolayer MoS_2 crystals and have demonstrated well-behaved operation in these devices. Excellent current saturation is observed at large drain voltages, and an analysis of the low-field transport indicates that the associated mobility is likely limited by scattering from charged impurities. The dominant conduction mechanisms are strongly dependent upon both the drain and gate biases with clear evidence of VRH at small V_d. With increases in both V_g and V_d, however, a satisfactory description of the characteristics can only be achieved by invoking the role of high-field velocity saturation. The velocity saturation was shown to arise from the presence of a strongly peaked electric field near the drain end of the channel, and the value of v_{sat} inferred from our studies was shown to be consistent with reports for multilayer MoS_2 transistors. This work therefore confirms the excellent potential of MoS_2 as a possible channel-replacement material and highlights the role of multiple transport phenomena in governing its transistor action.

ASSOCIATED CONTENT

Supporting Information

Information on the various devices studied, along with details of the simulation parameters, and a description of the mobility determination from the transfer characteristics. The Supporting Information is available free of charge on the ACS Publications website at DOI: 10.1021/acs.nanolett.5b01159.

AUTHOR INFORMATION

Corresponding Author

*E-mail: jbird@buffalo.edu. Phone: +1 (716) 645-1015.

Author Contributions

G.H. fabricated the MoS_2 transistors, and G.H., M.M., A.H., and N.A. measured their temperature-dependent electrical characteristics. G.H., R.S., H.R., G.B., S.N., R.V., and J.P.B. collaborated on the design of the experiments. K.G. performed the computational modeling of transistor performance, working in collaboration with U.S., G.H., and J.P.B. CVD growth of MoS_2 crystals was performed by S.N. in collaboration with R.V. and P.M.A. Y.G. and X.Z. performed AFM and Raman microscopy of the fabricated devices.

Notes

The authors declare no competing financial interest.

ACKNOWLEDGMENTS

Device fabrication and electrical characterization were performed in the group of J.P.B. under the support of the U.S. Department of Energy, Office of Basic Energy Sciences, Division of Materials Sciences and Engineering (Award # DE-FG02-04ER46180). Computations of MoS_2 transistor operation were undertaken in the group of U.S. and were supported by the Department of Electrical Engineering at the University at Buffalo. CVD growth of the MoS_2 was performed in the group of P.M.A. and was supported by the U.S. Army Research Office MURI Grant W911NF-11-1-0362.

REFERENCES

(1) Wang, Q. H.; Kalantar-Zadeh, K.; Kis, A.; Coleman, J. N.; Strano, M. S. *Nat. Nanotechnol.* **2012**, *7*, 699–712.

(2) Radisavljevic, B.; Radenovic, A.; Brivio, J.; Giacometti, V.; Kis, A. *Nat. Nanotechnol.* **2011**, *6*, 147–150.

(3) Ghatak, S.; Pal, A. N.; Ghosh, A. *ACS Nano* **2011**, *5*, 7707–7712.

(4) Castellanos-Gomez, A.; Barkelid, M.; Goossens, A. M.; Calado, V. E.; van der Zant, H. S.; Steele, G. A. *Nano Lett.* **2012**, *12*, 3187–3192.

(5) Kim, S.; Konar, A.; Hwang, W.-S.; Lee, J. H.; Lee, J.; Yang, J.; Jung, C.; Kim, H.; Yoo, J.-B.; Choi, J.-Y.; Jin, Y. W.; Lee, S. Y.; Jena, D.; Choi, W.; Kim, K. *Nat. Commun.* **2012**, *3*, 1011.

(6) Zhang, Y.; Ye, J.; Matsuhashi, Y.; Iwasa, Y. *Nano Lett.* **2012**, *12*, 1136–1140.

(7) Qiu, H.; Pan, L.; Yao, Z.; Li, J.; Shi, Y.; Wang, X. *Appl. Phys. Lett.* **2012**, *100*, 123104.

(8) Late, D. J.; Liu, B.; Matte, R. H. S. S.; Dravid, V. P.; Rao, C. N. R. *ACS Nano* **2012**, *6*, 5635–5641.

(9) Liu, H.; Neal, A. T.; Ye, P. D. *ACS Nano* **2012**, *6*, 8563–8569.

(10) Sik Hwang, W.; Remskar, M.; Yan, R.; Kosel, T.; Kyung Park, J.; Jin Cho, B.; Haensch, W.; Xing, H.; Seabaugh, A.; Jena, D. *Appl. Phys. Lett.* **2013**, *102*, 043116.

(11) Amani, M.; Chin, M. L.; Birdwell, A. G.; O'Regan, T. P.; Najmaei, S.; Liu, Z.; Ajayan, P. M. *Appl. Phys. Lett.* **2013**, *102*, 193107.

(12) Wu, W.; De, D.; Chang, S.-C.; Wang, Y.; Peng, H.; Bao, J.; Pei, S.-S. *Appl. Phys. Lett.* **2013**, *102*, 142106.

(13) Jariwala, D.; Sangwan, V. K.; Late, D. J.; Johns, J. E.; Dravid, V. P.; Marks, T. J.; Lauhon, L. J.; Hersam, M. C. *Appl. Phys. Lett.* **2013**, *102*, 173107.

(14) Walia, S.; Balendhran, S.; Wang, Y.; Ab Kadir, R.; Sabrin Zoolfakar, A.; Atkin, P.; Zhen Ou, J.; Sriram, S.; Kalantar-Zadeh, K.; Bhaskaran, M. *Appl. Phys. Lett.* **2013**, *103*, 232105.

(15) Baugher, B. W. H.; Churchill, H. O. H; Yang, Y.; Jarillo-Herrero, P. *Nano Lett.* **2013**, *13*, 4212–4216.

(16) Qiu, H.; Xu, T.; Wang, Z.; Ren, W.; Nan, H.; Ni, Z.; Chen, Q.; Yuan, S.; Miao, F.; Song, F.; Long, G.; Shi, Y.; Sun, L.; Wang, J.; Wang, X. *Nat. Commun.* **2013**, *4*, 2642.

(17) Radisavljevic, B.; Kis, A. *Nat. Mater.* **2013**, *12*, 815–820.

(18) Chang, H.-Y.; Zhu, W.; Akinwande, D. *Appl. Phys. Lett.* **2014**, *104*, 113504.

(19) Amani, M.; Chin, M. L.; Mazzoni, A. L.; Burke, R. A.; Najmaei, S.; Ajayan, P. M.; Lou, J.; Dubey, M. *Appl. Phys. Lett.* **2014**, *104*, 203506.

(20) Kwon, H.-J.; Jang, J.; Kim, S.; Subramanian, V.; Grigoropoulos, C. P. *Appl. Phys. Lett.* **2014**, *105*, 152105.

(21) Schmidt, H.; Wang, S.; Chu, L.; Toh, M.; Kumar, R.; Zhao, W.; Castro Neto, A. H.; Martin, J.; Adam, S.; Özyilmaz, B.; Eda, G. *Nano Lett.* **2014**, *14*, 1909–1913.

(22) Yuan, H.; Cheng, G.; You, L.; Zhu, H.; Li, W.; Kopanski, J. J.; Obeng, Y. S.; Hight Walker, A. R.; Gundlach, D. J.; Richter, C. A.; Ioannou, D. E.; Li, Q. *ACS Appl. Mater. Interfaces* **2015**, *7*, 1180–1187.

(23) Zhang, F.; Appenzeller, J. *Nano Lett.* **2015**, *15*, 301–306.

(24) Yoon, Y.; Ganapathi, K.; Salahuddin, S. *Nano Lett.* **2011**, *11*, 3768–3773.

(25) Wang, H.; Yu, L.; Lee, Y.-H.; Shi, Y.; Hsu, A.; Chin, M. L.; Li, L.-J.; Dubey, M.; Kong, J.; Palacios, T. *Nano Lett.* **2012**, *12*, 4674–4680.

(26) Lopez-Sanchez, O.; Lembke, D.; Kayci, M.; Radenovic, A.; Kis, A. *Nat. Nanotechnol.* **2013**, *8*, 497–501.

(27) Yin, Z.; Li, H.; Li, H.; Jiang, L.; Shi, Y.; Sun, Y.; Lu, G.; Zhang, Q.; Chen, X.; Zhang, H. *ACS Nano* **2012**, *6*, 74–80.

(28) Zeng, H.; Dai, J.; Yao, W.; Xiao, D.; Cui, X. *Nat. Nanotechnol.* **2012**, *7*, 490–493.

(29) Mak, K. F.; He, K.; Shan, J.; Heinz, T. F. *Nat. Nanotechnol.* **2012**, *7*, 494–498.

(30) Cao, T.; Wang, G.; Han, W.; Ye, H.; Zhu, C.; Shi, J.; Niu, Q.; Tan, P.; Wang, E.; Liu, B.; Feng, J. *Nat. Commun.* **2012**, *3*, 887.

(31) Lee, Y. H.; Zhang, X.-Q.; Zhang, W.; Chang, M.-T.; Lin, C.-T.; Chang, K. D.; Yu, Y.-C.; Wang, J. T.-W.; Chang, C.-S.; Li, L.-J.; Lin, T. W. *Adv. Mater.* **2012**, *24*, 2320–2325.

(32) Zhan, Y.; Liu, Z.; Najmaei, S.; Ajayan, P. M.; Lou, J. *Small* **2012**, *8*, 966–971.

(33) van der Zande, A. M.; Huang, P. Y.; Chenet, D. A.; Berkelbach, T. C.; You, Y.; Lee, G.-H.; Heinz, T. F.; Reichman, D. R.; Muller, D. A.; Hone, J. C. *Nat. Mater.* **2013**, *12*, 554–561.

(34) Fiori, G.; Szafranek, B. N.; Iannaccone, G.; Neumaier, D. *Appl. Phys. Lett.* **2013**, *103*, 233509.

(35) Sze, S. M.; Ng, K. K. *Physics of Semiconductor Devices*, 3^{rd} ed.; John Wiley & Sons, Inc., 2007.

(36) Castellanos-Gomez, A.; Cappelluti, E.; Roldan, R.; Agrait, N.; Guinea, F.; Rubio-Bollinger, G. *Adv. Mater.* **2013**, *25*, 899–903.

(37) Das, S.; Appenzeller, J. *Phys. Status Solidi RRL* **2013**, *7*, 268–273.

(38) Li, Y.; Xu, C.-Y.; Zhen, L. *Appl. Phys. Lett.* **2013**, *102*, 143110.

(39) Yu, W. J.; Liu, Y.; Zhou, H.; Yin, A.; Li, Z.; Huang, Y.; Duan, X. *Nat. Nanotechnol.* **2013**, *8*, 952–958.

(40) Ma, N.; Jena, D. *Phys. Rev. X* **2014**, *4*, 011043.

(41) *Atlas user manual.* www.silvaco.com (accessed March 21, 2014), SILVACO, Inc..

(42) Thomas, R. E. *Proc., IEEE* **1967**, *55*, 2192–2193.

(43) Fuhrer, M. S.; Hone, J. *Nat. Nanotechnol.* **2013**, *8*, 146–147.

AIP Applied Physics Letters

Reversing hot-carrier energy-relaxation in graphene with a magnetic field

H. Ramamoorthy, R. Somphonsane, G. He, D. K. Ferry, Y. Ochiai, N. Aoki, and J. P. Bird

Citation: Applied Physics Letters **104**, 193115 (2014); doi: 10.1063/1.4878535
View online: http://dx.doi.org/10.1063/1.4878535
View Table of Contents: http://scitation.aip.org/content/aip/journal/apl/104/19?ver=pdfcov
Published by the AIP Publishing

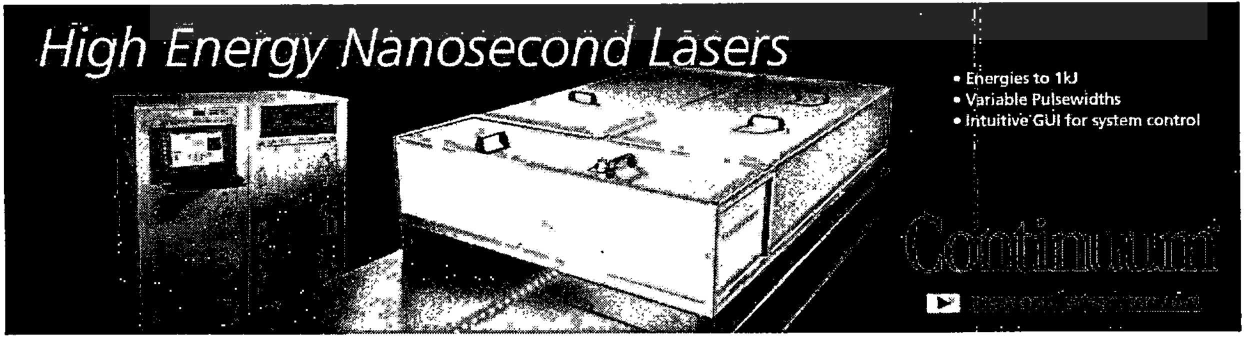

APPLIED PHYSICS LETTERS 104, 193115 (2014)

Reversing hot-carrier energy-relaxation in graphene with a magnetic field

H. Ramamoorthy,[1] R. Somphonsane,[2] G. He,[1] D. K. Ferry,[3,4] Y. Ochiai (落合勇一),[4]
N. Aoki (青木伸之),[4] and J. P. Bird[1,4]
[1]*Department of Electrical Engineering, University at Buffalo, Buffalo, New York 14260-1900, USA*
[2]*Department of Physics, King Mongkut's Institute of Technology Ladkrabang, Bangkok 10520, Thailand*
[3]*School of Electrical, Computer, and Energy Engineering, and Center for Solid State Electronics Research, Arizona State University, Tempe, Arizona 85287-5706, USA*
[4]*Graduate School of Advanced Integration Science, Chiba University, 1-33 Yayoi-cho, Inage-ku, Chiba 263-8522, Japan*

(Received 21 April 2014; accepted 6 May 2014; published online 15 May 2014)

We investigate the influence of a perpendicular magnetic field on hot-carrier energy relaxation in bilayer graphene. Working in the regime of incipient Landau quantization, we find that the magnetic field influences the relaxation in a very different manner, dependent upon the position of the Fermi level relative to the Dirac point. While for carrier densities $>10^{12}\,\mathrm{cm}^{-2}$ relaxation is slowed by the magnetic field, as the density of free carriers approaches zero it instead becomes quicker. We discuss this behavior in terms of the emergence of the zero-energy Landau level, and the role of charge puddling in graphene. © *2014 AIP Publishing LLC.* [http://dx.doi.org/10.1063/1.4878535]

Over the past decade, graphene has emerged as the leading two-dimensional material, due to its broad potential for application to a range of electronic technologies.[1] As our understanding of its fundamental transport properties has matured,[2] a problem that has attracted growing interest concerns the mechanisms for hot-carrier energy loss in this material. Driving ongoing theoretical[3–11] and experimental[12–34] interest in this problem are its implications for the development of active devices. In graphene bolometers,[23,25,34] for example, it is desirable to engineer the environment to strongly decouple nonequilibrium carriers from phonons. Similarly, in photonic devices such as solar cells[35] and lasers[36] energy transfer from excited carriers to phonons will degrade the optical output. From such examples alone, the need to quantitatively understand the various energy-loss pathways in graphene becomes apparent.

When carriers in graphene are driven out of equilibrium, their excess energy is redistributed by various mechanisms. The fastest of these occurs on a few tens of femtoseconds, as carrier-carrier scattering establishes an effective carrier temperature (T_e).[37] At the opposite end of the spectrum, energy exchange between carriers and phonons occurs on the energy-relaxation time (τ_ε), which may be as long as nanoseconds at 4.2 K.[23,28,31] The details of phonon-mediated cooling are predicted to differ significantly for pristine[3,4] and disordered[7,9] graphene, with the role of impurity-mediated "supercollisions" being emphasized for the latter.[7,9,28,29,32] Elsewhere, we have found surprising behavior in which energy relaxation quickens significantly as the Fermi level is swept towards the Dirac point (DP) from either band. This behavior is inconsistent with existing theories[3,4,7,9] for phonon-cooling pathways, and suggests that the mechanisms for energy relaxation may differ, near to and away from the DP.

A useful means for probing energy relaxation involves the application of a perpendicular magnetic field (B), which modifies the phase space for phonon scattering by inducing Landau quantization.[2] In recent work on graphene, Plochocka *et al.*[16] showed that the onset of this quantization is accompanied by a slowing of carrier thermalization. Baker *et al.*,[21,27] in contrast, used resistance thermometry to investigate electron-phonon cooling, and found this, also, to be slowed in the magnetic field. In none of these studies, however, was the carrier density varied continuously, so that the results obtained provided only a "snapshot" of the cooling at a few fixed energies far from the DP. In this Letter, however, we present a systematic study of the energy and magnetic-field dependence of τ_ε in graphene. For Fermi energies away from the DP, our results reveal a slowing of energy relaxation with increasing magnetic field, reminiscent of the aforementioned studies.[16,21,27] As the Fermi level approaches the DP, however, a distinct reversal of this behavior occurs, with the energy-relaxation rate increasing at higher magnetic fields. This observation appears to support the idea that a very different process dominates energy relaxation near the DP. We discuss these results in terms of the influence of the magnetic field on the graphene density of states, and on the charge-puddling phenomenon[38–40] that is known to lead to strong incompressibility near the DP.

Our study was performed on two bilayer graphene devices, realized by exfoliating Kish graphite onto a doped Si substrate with a 300-nm SiO_2 cap layer.[31,41,42] Layer identification was performed through a combination of optical microscopy and Raman imaging, and the use of bilayer graphene was primarily driven by the relative ease with which manageable pieces of this material could be isolated. Nonetheless, there is a natural benefit to using this system for studies of this type, since the magnetic-field induced changes in the density of states near the DP are more pronounced than for monolayer graphene.[2] One of the devices studied (referred to hereafter as BG1) was device B1 of Ref. 31, while in Fig. 1 we show a micrograph of the second device (which we will refer to as BG2) and indicate its four-terminal measurement geometry. Since consistent results were obtained for both BG1 and BG2, below we focus on our more comprehensive study of energy relaxation in BG2. This flake was approximately 8-μm long and 2–3-μm wide,

0003-6951/2014/104(19)/193115/5/$30.00

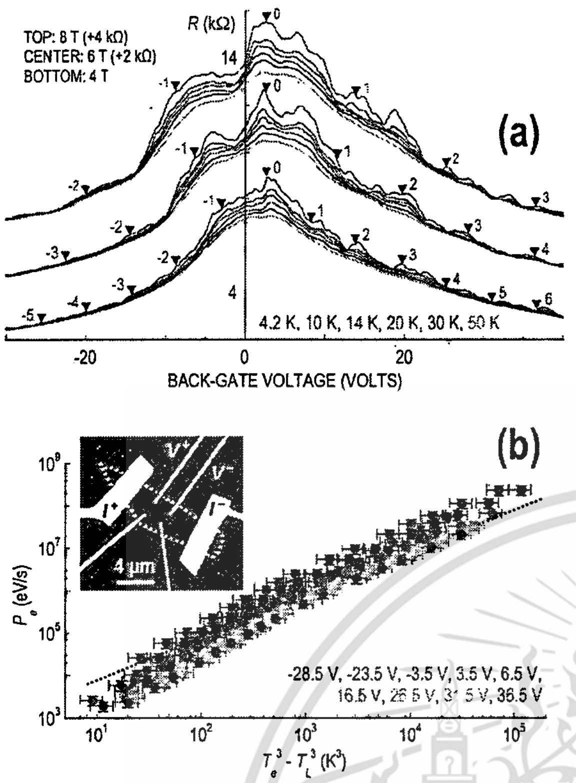

FIG. 1. (a) CF in device BG2. Measurements are at various T_L (indicated) and for $I = 100$ nA. Data at different fields are shifted vertically by the amounts indicated. Triangles identify gate voltages corresponding to filling of an integer number of Landau levels. The Landau index (N_L) is also indicated for each symbol, with negative values corresponding to filling by holes. (b) P_e vs. $T_e^3 - T_L^3$ for device BG2 at different V_g (indicated) and at zero field. The dotted line has power-law slope of one and $T_L = 4.2$ K. Inset: optical micrograph of device BG2. The graphene flake is denoted by the white dotted line and the four-terminal measurement geometry is indicated.

and the voltage probes indicated in Fig. 1 were 2-μm apart. Carrier density (n) was varied by means of the voltage (V_g) applied to the conductive Si substrate and Hall measurements could be used to reliably determine its value down to a level of $\sim 4 \times 10^{11}$ cm^{-2}.[31] Electron (hole) mobility at 4.2 K was determined to be 4340 (3620) cm^2/Vs over a wide range of density, with a diffusion constant that ranged from 80 to 210 cm^2 s^{-1}. Conductance of the graphene devices was measured by low-frequency (13 Hz) lock-in detection, using an AC current (I, whose RMS value was varied from 0.1 to 20 μA) to vary the carrier temperature relative to that of the lattice (T_L).

The hot-carrier thermometry that we perform here has been described previously in Ref. 31: it involves comparing measurements of the conductance fluctuations (CF), generated by varying the Fermi energy (V_g) in the material,[41,42] at a series of lattice temperatures (at fixed I) and measurement currents (at fixed T_L). The CF are demonstrated in Fig. 1(a), where we plot the resistance (R) of device BG2 as a function of V_g, at various T_L (4.2–50 K) and three different magnetic fields (4-, 6-, and 8-T). The DP is located at $V_g \sim 5$ V, indicating the presence of a small amount of chemical doping. Nonetheless, we observe reproducible CF that are suppressed with increasing T_L due to increased decoherence.[41,42] For each magnetic field, we have indicated with a set of markers the gate voltages corresponding to complete filling of an integer number ($N_L = nh/4eB$, with the sheet density n provided by a parallel-plate capacitor expression) of Landau levels. While there is some correlation between these voltages and the presence of significant structure in the resistance, the correlation is not perfect. From this, we conclude that we are in the regime where the Landau quantization is incipient.

A key parameter in discussions of hot-carrier relaxation is the energy-loss rate (P_e), the power dissipated per carrier in the material ($P_e = I^2R/nLW$, with R, L, and W the resistance, length, and width of the conductor, respectively). Typically, this rate is expressed in the form[43]

$$P_e = A(T_e^p - T_L^p), \tag{1}$$

where the constants A and p depend upon the specific scattering mechanisms responsible for energy relaxation. In graphene it has been suggested that p should take values of 4 and 3, respectively, for electron-phonon scattering in pristine material,[4] and for impurity-mediated supercollisions.[9] In previous work, performed at zero magnetic field, we found[31] that the loss rate in both bilayer and monolayer graphene is well described by $p = 3$, for wide variations of temperature and density. This behavior is reproduced in Fig. 1(b), where we plot P_e vs. ($T_e^3 - T_L^3$) for device BG2. While these data are again consistent with $p = 3$, as noted already in Ref. 31 it is unlikely that such behavior is due to supercollisions. These are only expected to dominate[9] when the Bloch-Gruneisen temperature (T_{BG}) is smaller than T_L, while our experiments are performed in the opposite regime where $T_{BG} > T_L$. ($T_{BG} = 2\hbar s k_F/k_B \sim 54n^{1/2}$ K, where $s = 2.1 \times 10^4$ ms^{-1} is the sound velocity in graphene, k_F is the Fermi radius, and n is the electron or hole density, in units of 10^{12} cm^{-2}. For the lowest density of around 4×10^{11} cm^{-2} that we are able to reliably infer from Hall measurements, $T_{BG} \sim 34$ K.) In this sense, it appears that the behavior of P_e in Fig. 1(b) represents a more general signature of hot-carrier relaxation in graphene, a conclusion that is consistent with the work of Ref. 30 where an exponent of $p = 3$ was also found outside of the supercollision limit.

In Fig. 2(a), we demonstrate how hot-carrier relaxation is influenced by the magnetic field, plotting the energy-loss rate for electrons and holes at $B = 8$ T (where the negative values denote the hole density). For both types of carrier, and at all gate voltages, the observed variations are consistent with the form of Eq. (1), with an exponent $p = 3$. In contrast to Fig. 1(b), however, the data for the different gate voltages do not collapse onto a common curve but rather exhibit a significant spread in values (implying significant differences in the prefactor A). As we reveal in Fig. 2(b), this much broader dispersion of loss rates arises from a significant change in the nature of carrier heating when the magnetic field is applied. In this figure, we plot the density-dependent variation of T_e at several different magnetic fields (and for fixed total electrical power, $I^2R = 20$ nW). At low magnetic fields, in the range of 0–2 T, the heating is most effective near the DP, where T_e reaches a local maximum. Higher magnetic fields induce a dramatic reversal of this behavior, however, with T_e now developing a minimum near

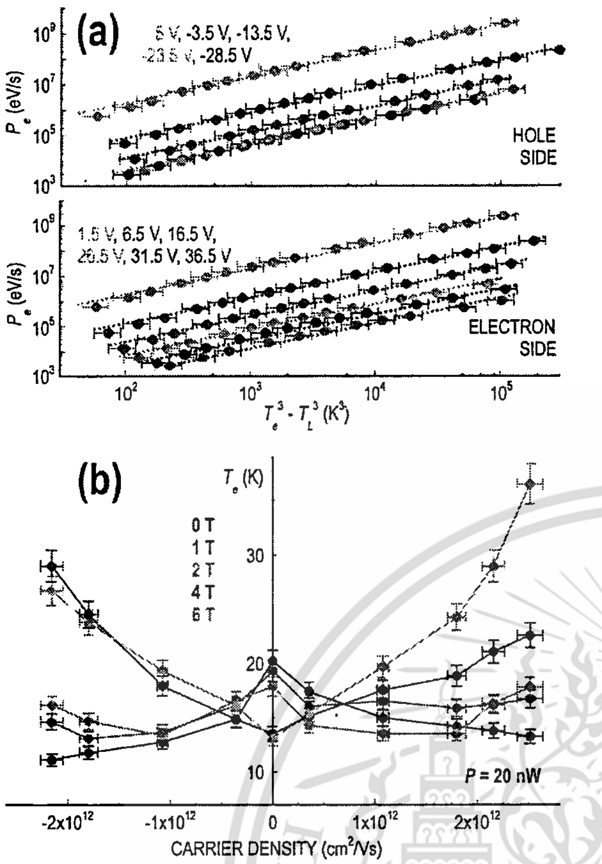

FIG. 2. (a) P_e vs. $T_e^3 - T_L^3$ for device BG2 at different V_g (indicated) at 8 T. Dotted lines through the data have power-law slope of 1 and $T_L = 4.2$ K. Top (bottom) panel: hole (electron) side of DP. (b) Variation of the effective carrier temperature, $T_e(n, B)$, obtained for fixed total electric power of 20 nW.

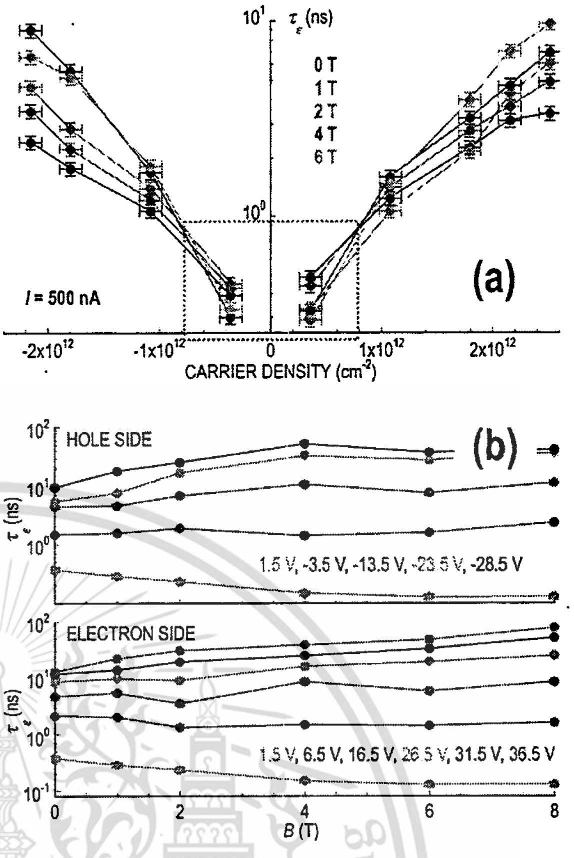

FIG. 3. (a) Variation of τ_ε with density for device BG2 at fields in the range of 0–6 T (indicated, measurement current = 500 nA). (b) Variation of τ_ε with B at various V_g. The upper (lower) panel is for holes (electrons) and $I = 100$ nA.

the DP. At the same time, T_e also exhibits a much stronger variation with density at these magnetic fields, and it is this characteristic that is responsible for the wide spread in energy-loss rates apparent in Fig. 2(a).

By imposing the requirement of energy balance, knowledge of the carrier temperature allows us to infer the energy-relaxation time[44]

$$P_e = \frac{k_B(T_e - T_L)}{\tau_\varepsilon}. \tag{2}$$

In Fig. 3(a), we plot the density-dependent variation of τ_ε at magnetic fields in the range of 0–6 T. At each magnetic field, τ_ε decreases by at least an order of magnitude as the Fermi level approaches the DP from either band, consistent with our earlier work at zero field.[31] The important aspect revealed here, however, is a strong influence of the magnetic field on heating, dependent upon the position of the Fermi level relative to the DP. For densities away from the DP ($|n| > \sim 10^{12}\,\text{cm}^{-2}$), we find that τ_ε increases with magnetic field, implying that relaxation is correspondingly slowed. This behavior is reversed at lower densities, however, where τ_ε instead decreases with increasing field (data enclosed by the dotted line in Fig. 3(a)). This crossover is further demonstrated in Fig. 3(b), where we plot the variation of τ_ε as a function of B for several gate voltages. For the data obtained closest to the DP (gray symbols), τ_ε decreases by a factor of three when the magnetic field is increased from 0- to 8-T. At the highest densities, on the other hand, it increases by as much as a factor of five for the same variation in field strength.

Previously, there have been several reports on the influence of a magnetic field on hot-carrier relaxation in graphene.[16,21,27] The common conclusion that followed from these studies, which were performed at fixed Fermi energies away from the DP, is that relaxation is suppressed at higher magnetic fields, due to the emergence of the graphene Landau-level structure. While we do not realize well-resolved Landau levels in our work, the emergence of structure in the CF of Fig. 1(a) nonetheless suggests the presence of incipient Landau quantization. Consequently, the slowing of cooling that we observe at densities away from the DP appears to be consistent with the results of these earlier studies.

By varying carrier density via the gate voltage, we have found that energy relaxation undergoes a dramatic reversal near the DP, where the application of a magnetic field now leads to more-efficient cooling. This behavior, also, may be related to the emergence of the Landau spectrum, most notably to the development of the zero-energy level[2] that is unique to monolayer and bilayer graphene. Magneto-capacitance measurements provide a powerful tool to probe the structure of this level,[45–47] and reveal two competing effects as the magnetic field is increased. The first of these is a growth in the density of states at the DP, while the second is a simultaneous reduction of this density on the electron and hole flanks.[45] By providing an enhanced phase space for electron-phonon coupling near the DP, it seems reasonable that the magnetic field could therefore enhance the relaxation rate.

While these general arguments concerning Landau quantization provide an attractive framework for the interpretation of our experiment, it must be emphasized that the quantization is only emergent in our experiments and that other scenarios should also be considered. Most notably, in our prior work at zero magnetic field,[31] we noted that the short relaxation times inferred near the DP occur in a regime where the effects of charge puddling[38–40] are expected to be important. The puddle state is characterized by strong thermodynamic incompressibility, implying that the carriers become "frozen" into a microscopic configuration that is resistant to excitation.[31] Recent experiments in which scanning-probe techniques were used to investigate the microscopic structure of the puddling[40] have shown that the localization associated with the puddles is significantly enhanced by a magnetic field. It is therefore also possible that the unusual heating behavior we observe near the DP is related to the incompressible character of the puddling, and to its enhancement in a magnetic field.

Finally, before concluding, we comment on the possible role of screening of the carrier-phonon interaction, and the dependence of this on magnetic field and density. Starting at zero field, while screening should be effective at higher densities it should weaken as the Fermi level is swept towards the DP. This in turn should lead to stronger scattering, and so faster relaxation, reminiscent of our experiment. A problem with this picture emerges when a magnetic field is applied, however, since screening at wavelengths longer than the Landau-orbit size will be suppressed. In this case, the main effect of increasing density should be to enhance scattering via the unscreened interaction, due to the associated increase of the electron or hole density of states. This would imply faster energy relaxation at higher densities, behavior opposite to that found here. While we cannot completely rule out the role of screening in our observations, the experimental behavior therefore seems to suggest a deeper rationale for the nature of the cooling process.

In conclusion, we have investigated the influence of incipient Landau quantization on hot-carrier relaxation in bilayer graphene. The magnetic field influences the relaxation in a very different manner, dependent upon the position of the Fermi level relative to the Dirac point. For electron or hole densities greater than roughly $10^{12}\,\mathrm{cm}^{-2}$, relaxation is slowed by the magnetic field. As the Fermi level approaches the DP, however, a reversal in this behavior occurs, with the relaxation quickening at higher fields. We have discussed how this behavior may be related to the emergence of the zero-energy Landau level, and to the peculiar nature of the graphene puddle state in a magnetic field. While we have focused on the influence of a magnetic field on relaxation in bilayer graphene, in previous work at zero field[31] we found the details of the relaxation to be very similar for both monolayer- and bilayer-graphene.[31] From this, we concluded that the density-dependent variation of τ_ε should not be a consequence of the linear bands, but rather more likely arises from the vanishing of the density of states near the DP. From this perspective, we expect the magnetic field to influence relaxation in monolayer graphene in a similar manner to that found here, although this requires confirmation through proper experiment. In spite of this, our observations nonetheless provide an important perspective on our emerging understanding of hot-carrier relaxation mechanisms in graphene.

This research was supported by the U.S. Department of Energy, Office of Basic Energy Sciences, Division of Materials Sciences, and Engineering under Award No. DE-FG02-04ER46180 (JPB), and the National Science Foundation under Award No. OISE0968405 (HR & RS).

[1] K. S. Novoselov, V. I. Fal'ko, L. Colombo, P. R. Gellert, M. G. Schwab, and K. Kim, Nature **490**, 192 (2012).
[2] H. C. Neto, F. Guinea, N. M. R. Peres, K. S. Novoselov, and A. K. Geim, Rev. Mod. Phys. **81**, 109 (2009).
[3] R. Bistritzer and A. H. MacDonald, Phys. Rev. Lett. **102**, 206410 (2009).
[4] S. Kubakaddi, Phys. Rev. B **79**, 075417 (2009).
[5] W. K. Tse and S. D. Sarma, Phys. Rev. B **79**, 235406 (2009).
[6] J. K. Viljas and T. T. Heikkilä, Phys. Rev. B **81**, 245404 (2010).
[7] J. C. W. Song, M. S. Rudner, C. M. Marcus, and L. S. Levitov, Nano Lett. **11**, 4688 (2011).
[8] T. Low, V. Perebeinos, R. Kim, M. Freitag, and P. Avouris, Phys. Rev. B **86**, 045413 (2012).
[9] J. C. W. Song, M. Y. Reizer, and L. S. Levitov, Phys. Rev. Lett. **109**, 106602 (2012).
[10] W. Chen and A. A. Clerk, Phys. Rev. B **86**, 125443 (2012).
[11] M. V. Fischetti, J. Kim, S. Narayanan, Z.-Y. Ong, C. Sachs, D. K. Ferry, and S. J. Aboud, J. Phys.: Condens. Matter **25**, 473202 (2013).
[12] I. Meric, M. Y. Han, A. F. Young, B. Ozyilmaz, P. Kim, and K. L. Shepard, Nat. Nanotechnol. **3**, 654 (2008).
[13] M. Freitag, M. Steiner, Y. Martin, V. Perebeinos, C. Chen, J. C. Tsang, and P. Avouris, Nano Lett. **9**, 1883 (2009).
[14] A. Barreiro, M. Lazzeri, J. Moser, F. Mauri, and A. Bachtold, Phys. Rev. Lett. **103**, 076601 (2009).
[15] A. M. DaSilva, K. Zou, J. K. Jain, and J. Zhu, Phys. Rev. Lett. **104**, 236601 (2010).
[16] P. Plochocka, P. Kossacki, A. Golnik, T. Kazimierczuk, C. Berger, W. A. de Heer, and M. Potemski, Phys. Rev. B **80**, 245415 (2009).
[17] J. Voutilainen, A. Fay, P. Häkkinen, J. K. Viljas, T. T. Heikkilä, and P. J. Hakonen, Phys. Rev. B **84**, 045419 (2011).
[18] Z. Tan, C. Tan, L. Ma, G. T. Liu, L. Lu, and C. L. Yang, Phys. Rev. B **84**, 115429 (2011).
[19] N. M. Gabor, J. C. W. Song, Q. Ma, N. L. Nair, T. Taychatanapat, K. Watanabe, T. Taniguchi, L. S. Levitov, and P. Jarillo-Herrero, Science **334**, 648 (2011).
[20] D. Sun, G. Aivazian, A. M. Jones, J. S. Ross, W. Yeo, D. Cobden, and X. Xu, Nat. Nanotechnol. **7**, 114 (2012).
[21] A. M. R. Baker, J. A. Alexander-Webber, Y. Altebaeumer, and R. J. Nicholas, Phys. Rev. B **85**, 115403 (2012).
[22] A. S. Price, S. M. Hornett, A. V. Shytov, E. Hendry, and D. W. Horsell, Phys. Rev. B **85**, 161411(R) (2012).
[23] J. Yan, M. H. Kim, J. A. Elle, A. B. Sushkov, G. S. Jenkins, H. M. Milchberg, M. S. Fuhrer, and H. D. Drew, Nat. Nanotechnol. **7**, 472 (2012).
[24] A. C. Betz, F. Vialla, D. Brunel, C. Voisin, M. Picher, A. Cavanna, A. Madouri, G. Fève, J.-M. Berroir, B. Plaçais, and E. Pallecchi, Phys. Rev. Lett. **109**, 056805 (2012).
[25] K. C. Fong and K. C. Schwab, Phys. Rev. X **2**, 031006 (2012).
[26] K. Majumdar, S. Kallatt, and N. Bhat, Appl. Phys. Lett. **101**, 123505 (2012).
[27] A. M. R. Baker, J. A. Alexander-Webber, T. Altebaeumer, S. D. McMullan, T. J. B. M. Janssen, A. Tzalenchuk, S. Lara-Avila, S. Kubatkin, R. Yakimova, C.-T. Lin, L.-J. Li, and R. J. Nicholas, Phys. Rev. B **87**, 045414 (2013).
[28] M. W. Graham, S.-F. Shi, D. C. Ralph, J. Park, and P. L. McEuen, Nat. Phys. **9**, 103 (2013).

[29] A. C. Betz, S. H. Jhang, E. Pallecchi, R. Ferreira, G. Fève, J.-M. Berroir, and B. Plaçais, Nat. Phys. **9**, 109 (2013).

[30] I. V. Borzenets, U. C. Coskun, H. T. Mebrahtu, Yu. V. Bomze, A. I. Smirnov, and G. Finkelstein, Phys. Rev. Lett. **111**, 027001 (2013).

[31] R. Somphonsane, H. Ramamoorthy, G. Bohra, G. He, D. K. Ferry, Y. Ochiai, N. Aoki, and J. P. Bird, Nano Lett. **13**, 4305 (2013).

[32] M. W. Graham, S.-F. Shi, Z. Wang, D. C. Ralph, J. Park, and P. L. McEuen, Nano Lett. **13**, 5497 (2013).

[33] I. Gierz, J. C. Petersen, M. Mitrano, C. Cacho, I. C. E. Turcu, E. Springate, A. Stöhr, A. Köhler, U. Starke, and A. Cavalleri, Nature Mater. **12**, 1119 (2013).

[34] Q. Han, T. Gao, R. Zhang, Y. Chen, J. Chen, G. Liu, Y. Zhang, Z. Liu, X. Wu, and D. Yu, Sci. Rep. **3**, 3533 (2013).

[35] X. Miao, S. Tongay, M. K. Petterson, K. Berke, A. G. Rinzler, B. R. Appleton, and A. F. Hebard, Nano Lett. **12**, 2745 (2012).

[36] A. A. Lagatsky, Z. Sun, T. S. Kulmala, R. S. Sundaram, S. Milana, F. Torrisi, O. L. Antipov, Y. Lee, J. H. Ahn, C. T. A. Brown, W. Sibbett, and A. C. Ferrari, Appl. Phys. Lett. **102**, 013113 (2013).

[37] M. Breusing, C. Ropers, and T. Elsaesser, Phys. Rev. Lett. **102**, 086809 (2009).

[38] J.-H. Chen, C. Jang, S. Adam, M. S. Fuhrer, E. D. Williams, and M. Ishigami, Nat. Phys. **4**, 377 (2008).

[39] J. Martin, N. Akerman, G. Ulbricht, T. Lohmann, J. H. Smet, K. von Klitzing, and A. Yacoby, Nat. Phys. **4**, 144 (2008).

[40] S. Jung, G. M. Rutter, N. N. Klimov, D. B. Newell, I. Calizo, A. R. Hight-Walker, N. B. Zhitenev, and J. A. Stroscio, Nat. Phys. **7**, 245 (2011).

[41] G. Bohra, R. Somphonsane, N. Aoki, Y. Ochiai, R. Akis, D. K. Ferry, and J. P. Bird, Phys. Rev. B **86**, 161405(R) (2012).

[42] G. Bohra, R. Somphonsane, N. Aoki, Y. Ochiai, D. K. Ferry, and J. P. Bird, Appl. Phys. Lett. **101**, 093110 (2012).

[43] P. J. Price, J. Appl. Phys. **53**, 6863 (1982).

[44] D. K. Ferry, *Semiconductor Transport* (Taylor & Francis, London, U.K., 2000).

[45] L. A. Ponomarenko, R. Yang, R. V. Gorbachev, P. Blake, A. S. Mayorov, K. S. Novoselov, M. I. Katsnelson, and A. K. Geim, Phys. Rev. Lett. **105**, 136801 (2010).

[46] G. L. Yu, R. Jalil, B. Belle, A. S. Mayorov, P. Blake, F. Schedin, S. V. Morozov, L. A. Ponomarenko, F. Chiappini, S. Wiedmann, U. Zeitler, M. I. Katsnelson, A. K. Geim, K. S. Novoselov, and D. C. Elias, Proc. Natl. Acad. Sci. U. S. A. **110**, 3282 (2013).

[47] X. L. Chen, L. Wang, W. Li, Y. Wang, Y. H. He, Z. F. Wu, Y. Han, M. W. Zhang, W. Xiong, and N. Wang, Appl. Phys. Lett. **102**, 203103 (2013).

บันทึกรายการรับ-จ่ายเงิน โครงการวิจัย ที่ ....51......... ตั้งแต่วันที่ ......1 ต.ค. 2557..... ถึงวันที่ ....30 ก.ย. 2558.....

แหล่งทุน : แหล่งเงินรายได้

ชื่อโครงการ : การจำแนกประเภทของกราฟีนด้วยเทคนิคกล้องจุลทรรศน์และรามานสเปกโตรสโคปี

ชื่อหัวหน้าโครงการ : ดร. รัชนก สมพรเสน่ห์

ว/ด/ป	รายการ	เลขที่อ้างถึง	รายการรับ - จ่าย			รายรับ	รายจ่าย						รวม
			รับ	จ่าย	คงเหลือ	ดอกเบี้ย	งบบุคลากร	งบดำเนินงาน				งบลงทุน	รายจ่าย
							ค่าจ้างชั่วคราว	ค่าตอบแทน	ค่าใช้สอย	ค่าวัสดุ	ค่าสาธารณูปโภค	ค่าครุภัณฑ์	
	งบประมาณที่ได้รับการอนุมัติ (ตามแผน)		50,000.00										-
19/11/57	จำนวนเงินที่ได้รับ		50,000.00										
	หัก ค่าใช้จ่าย			#######			-	-		50,868.91	-	-	50,868.91
	งบประมาณคงเหลือ		50,000.00		-868.91	0.00							
	รายละเอียดค่าใช้จ่าย												
7/7/57	SF-BM-10+	590348								3,379.85			3,379.85
7/7/57	SF-BM-20+	590348								2,607.33			2,607.33
7/7/57	SF-BM-30+	590348								3,745.80			3,745.80
7/7/57	Freight Charges	590348								274.12			274.12
7/7/57	ZX85-12G+	590349								12,868.88			12,868.88
7/7/57	Freight Charges	590349								274.12			274.12
7/7/57	ZX75BP-2150+	590350								9,478.85			9,478.85
7/7/57	Freight Charges	590350								274.12			274.12
7/7/57	ZX05-73L+	590352								8,292.95			8,292.95
7/7/57	Freight Charges	590352								274.12			274.12
13/7/57	30 dB Fixed Attenuator	PSIN701010								9,398.77			9,398.77
	รวม		-	-	-	-	-	-			-	-	50,868.91

ลงชื่อหัวหน้าโครงการ .... วันที่ ....10 สิงหาคม 2558...

Curriculum Vitae

Name: Dr. Ratchanok Somphonsane

1. Personal Data

☑ Female ☐ Male

Date of Birth: 4/26/1982

Affiliated University/Institute : King Mongkut's Institute of Technology Ladkrabang
Department of Physics, Faculty of Science
Chalongkrung Rd. Ladkrabang
Bangkok 10520 THAILAND

Academic Position: Lecturer

E-mail: rsomphonsane@gmail.com

Telephone: 091-706-2494

2. Education

Degree	Major	University	Year Completed
Ph.D.	Physics	The State University of New York, at Buffalo	2014
Grad. Dip.	Teaching Profession	Srinakharinwirot University	2005
B.Sc. (1st class honors)	Physics	Prince of Songkla University	2004

3. Research Experience

2013-2014	Posdoctoral fellow, The State University of New York, at Buffalo, New York, USA
2009-2013	Research assistant, The State University of New York, at Buffalo New York, USA
2012	Visiting research fellow, Rice University, Texas, USA

Skill/Expertise: Nanoelectronics, Graphene nanoelectronics, Nanofabrication, Electrical measurement, Low-temperature measurement

4. Major Prize / Award / Honor

Year	Award	Institute
2015	Best Senior Poster Award of EDISON'19	Edison'19 Conference
2011	Best Poster Award	SEAS, The State University of New York, at Buffalo, USA
2011	Best Poster Award	EE Department, The State University of New York, at Buffalo, USA

5. Scholarships/Fellowships

Year	Scholarships/Fellowships	Institute
2016-2017	Grant for new researcher	Ministry of Science and Technology, Thailand
2016-2017	Grant for new researcher	King Mongkut's Institute of Technology Ladkrabang
2015-2017	Grant for new researcher	Thailand research funding
2015-2017	Grant for new researcher	King Mongkut's Institute of Technology Ladkrabang
2015-2016	Grant for new researcher	King Mongkut's Institute of Technology Ladkrabang
2007-2012	Scholarship for Ph.D. study	Ministry of Science and Technology, Thailand
2004-2005	Scholarship for Graduate study in Teaching profession	The Insitute for the Promotion of Teaching Science and Technology, Thailand
2000-2004	Scholarship for undergraduate study	The Insitute for the Promotion of Teaching Science and Technology, Thailand

6. Publications

1. R. Somphonsane, H. Ramamoorthy, G. He, J. Nathawat, C.-P. Kwan, Y.-H. Lee, J. Fransson, and J. P. Bird *“Evaluating the contribution of impurities and phonons to the resistivity of graphene by differential-conductance mapping”* Phys. Rev. B (2016, under revision)
2. G. He, H. Ramamoorthy, C.-P. Kwan, Y.-H. Lee, J. Nathawat, R. Somphonsane, M. Matsunaga, A. Higuchi, N. Aoki, Y. Gong, X. Zhang, R. Vajtai, P. M. Ajayan, and J. P. Bird "*Thermally-Assisted Nonvolatile Memory in Monolayer* MoS_2 *Transistors*", Nano Lett. 16, DOI: 10.1021/acs.nanolett.6b02905 (2016)
3. H. Ramamoorthy, R. Somphonsane, J. Radice, G. He, C.-P. Kwan, and J. P. Bird *“"Freeing" Graphene from its Substrate: Observing Intrinsic Velocity Saturation with Rapid Electrical Pulsing”* Nano Lett. **16**, 399–403 (2016)
4. B. Liu, R. Akis, D. K. Ferry, G. Bohra, R. Somphonsone, H. Ramamoorthy, and J. P. Bird, *“Conductance fluctuations in graphene in the presence of long-range disorder”* J. Phys.: Condens. Matter **28**, 135302 (2016)
5. D. K. Ferry, R. Somphonsone, H. Ramamoorthy, and J. P. Bird, *“Energy relaxation of hot carriers in graphene via plasmon interactions”* J. Comput. Electron. **15**, 144-153 (2016)
6. D. K. Ferry, R. Somphonsone, H. Ramamoorthy, and J. P. Bird, *“Plasmon-mediated energy relaxation in graphene”* Appl. Phys. Lett. **107**, 262103 (2015)

7. G. He, K. Ghosh, U. Singisetti, H. Ramamoorthy, R. Somphonsane, G. Bohra, M. Matsunaga, A. Higuchi, N. Aoki, S. Najmaei, Y. Gong, X. Zhang, R. Vajtai, P. M. Ajayan, and J. P. Bird, "*Conduction Mechanisms in CVD-Grown Monolayer* MoS_2 *Transistors: From Variable-Range Hopping to Velocity Saturation*" Nano Lett. 15, 5052 (2015)
8. H. Ramamoorthy, R. Somphonsane, G. He, D. K. Ferry, Y. Ochiai, N. Aoki, and J. P. Bird, "*Reversing hot-carrier energy-relaxation in graphene with a magnetic field*", Appl. Phys. Lett. 104, 193115 (2014)
9. R. Somphonsane, H. Ramamoorthy, G. Bohra, G. He, D. K. Ferry, Y. Ochiai, N. Aoki, and J. P. Bird, "*Fast energy relaxation of hot carriers near the Dirac point of graphene*", Nano Lett. 13, 4305 (2013)
10. G. Bohra, R Somphonsane, N. Aoki , Y. Ochiai, R. Akis, D. K. Ferry, and J. P. Bird, "*Nonergodicity and microscopic symmetry breaking of the conductance fluctuations in disordered mesoscopic graphene*", Phys. Rev. B 86, 161405(R) (2012)
11. G. Bohra, R. Somphonsane, N. Aoki , Y. Ochiai, D. K. Ferry, and J. P. Bird, "*Robust mesoscopic fluctuations in disordered graphene*", Appl. Phys. Lett. 101, 093110 (2012)

7. Presentations

Oral Presentations

1. Gave a talk on "*Relaxation Dynamics of Hot Carriers in Graphene Revealed by Current-Induced Heating Measurements*" at NanoThailand 2014 (The 4th Thailand International Nanotechnology Conference), at Phatumthani, Thailand on Nov 26-28, 2014
2. Gave a talk on "Reversing Hot-Carrier Energy Relaxation with a Magnetic field" at IEEE NMDC 2014 (IEEE Nanotechnology Materials and Devices Conference) at Sicily, Italy on Oct 12-15, 2014
3. Gave a talk on on "Hot-Carrier Relaxation in Graphene and Its Dependence on a Magnetic Field" at GRPR 2014 (The 6th International Conference on Recent Progress in Graphene Research) at Taipei, Taiwan on Sep 21-25, 2014

Poster Presentations

1. R. Somphonsane, H. Ramamoorthy, and J. P. Bird, "*Phonon-induced hot-carrier scattering in graphene: Insight from differential conductance*" at: 9th International Conference on Electron Dynamics in Semiconductors, Optoelectronics and Nanostructures (Edison' 19), Salamanca, Spain (2015)

2. H. Ramamoorthy, R. Somphonsane, G. He, D. K. Ferry, N. Aoki, Y. Ochiai and J. P. Bird, "*Hot-Carrier Relaxation in Graphene in a Magnetic Field*" at: 21st International Conference on "High Magnetic Fields in Semiconductor Physics"(HMF-21), Panama City Beach, Florida (2014)
3. R. Somphonsane, H. Ramamoorthy, D. K. Ferry, and J. P. Bird, "*Magnetic-field dependence of hot-carrier relaxation in graphene*", Poster presentation at: The International Symposium on Advanced Nanodevices and Nanotechnology (ISANN), Kauai, Hawaii (2013)
4. H. Ramamoorthy, R. Somphonsane, and J. P. Bird, "*Current-induced cleaning of graphene and graphene-metal contacts*" The International Symposium on Advanced Nanodevices and Nanotechnology (ISANN), Kauai, Hawaii (2013)
5. R. Somphonsane, H. Ramamoorthy, G. Bohra, G. He, D. K. Ferry, Y. Ochiai, N. Aoki, and J. P. Bird, "*Hot-carrier energy relaxation near the Dirac point of graphene*", International Workshop on Recent Progress in Nonequilibrium Quantum Many-Body Theory, Buffalo, NY (2013)
6. R. Somphonsane, H. Ramamoorthy, G. Bohra, G. He, D. K. Ferry, Y. Ochiai, N. Aoki, and J. P. Bird, "*Energy relaxation in mesoscopic graphene*", 3rd International Symposium on Terahertz Nanoscience (TeraNano III), Honolulu, Hawai (2012)